
Non-linear beam theory in context of bio-inspired sensing of flows

submitted by:

B.Sc. Daniel Lavayen Farfán

for the degree of

Master of Science in Mechanical Engineering

Supervising professors:

Technische Universität Ilmenau Pontificia Universidad Católica del Perú
Dr.-Ing. habil. Dipl.-Math. Carsten Behn Dr.-Ing. Dante Ángel Elías Giordano

Ilmenau, Germany

Conceptual Formulation of the Master Thesis

of Mr. BSc. Daniel Lavayen-Farfan

Topic: Non-linear beam theory in context of bio-inspired sensing of flows

The master thesis complements the current research activities at the Technical Mechanics Group at TU Ilmenau. The focus is on non-visual characterization of objects and flows using tactile sensors, which are inspired by animal vibrissae. The aim is to develop models of technical sensors which are used (1) to determine the contact with an object or the deformation due to a flow, and (2) to reconstruct the boundaries/the contour of the obstacle or the magnitude and direction of the flow. The flow detection is in the focus of the master thesis.

The Euler-Bernoulli bending rod (in a plane) serves as a model of the artificial sensor. Already existing models for object contour scanning and reconstruction as well as for surface texture detection shall serve as an inspiration for a bio-inspired beam model to detect flows. For this, the current literature in the field of flow detection by means of tactile mechanical sensors has to be reviewed. Then, a beam model has to be set up and has to be analytically and numerically analyzed, in that way to detect the flows. Tasks of the master thesis are:

- to become acquainted with the non-linear bending theory of beams, the mathematical handling in performing shooting methods to solve the boundary-value problems;
- to review the corresponding literature of flow detection;
- to set up a Matlab-program for numerical simulations;
- to analyze the bending behavior and to perform parameter studies: modify the support of the tactile beam (clamping \rightarrow elastic support; bearing with a torsional spring) / modify the cylindrically shaped beam to a tapered one / incorporate a pre-curvature to the beam structure.

The master thesis shall be layouted using LaTeX, all necessary files (LaTeX files, Matlab files, figures, pictures, drawings, literature files, ...) have to taken on a supplementing CD.

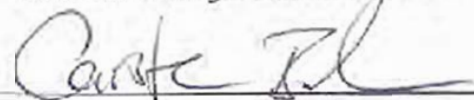
Date of issue: 1st July, 2016

Responsible Professor (TU Ilmenau): PD Dr.-Ing. habil. Carsten Behn

Responsible Professor (PUCP Lima): Prof. Dante Angel Elias Giordano

Ilmenau, 21.06.2016

Location, Date



Signature of the responsible professor TU Ilmenau

LIMA, 14.06.2016

Location, Date



Signature of the responsible professor PUCP Lima

Ilmenau, 29.06.2016

Location, Date



Signature of the student

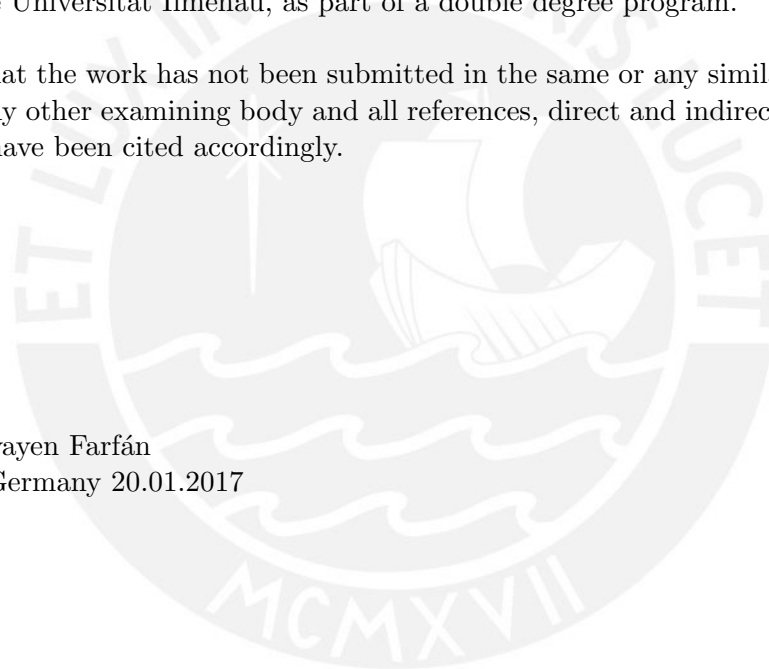
Declaration

I declare that the work is entirely my own and was produced with no assistance from third parties.

This work was presented at the same time as a thesis of the Master program “*Maestría en Ingeniería Mecánica*” (Master in Mechanical Engineering) at the Pontificia Universidad Católica del Perú and as the Masterarbeit of the “*Master Maschinenbau*” program at Technische Universität Ilmenau, as part of a double degree program.

I certify that the work has not been submitted in the same or any similar form for assessment to any other examining body and all references, direct and indirect, are indicated as such and have been cited accordingly.

Daniel Lavayen Farfán
Ilmenau, Germany 20.01.2017



Abstract

The thesis at hand is part of a research project that attempts to study and develop vibrissa inspired tactile sensors for object and fluid flow detection. The main focus of the thesis is on the development of a model for a vibrissa-like sensor for obstacle contour recognition under fluid loads. To this end, a mechanical model – based on the non-linear Euler-Bernoulli beam theory – is established. The model includes the main characteristics found in a natural vibrissa, such as elasticity of the base, that acts as the vibrissa follicle; the intrinsic curvature; and conicity. The characteristics are represented as parameters of the model. The model is subjected to a contact load and a fluid flow load, represented by a concentrated load and a distributed load, respectively. Then, the model is transformed into a dimensionless representation for further studies to achieve more general assertions. A variation of the magnitude of these loads, as well as the vibrissa parameters is also analyzed. A direct numerical approximation using the finite difference method, along with the shooting method, is used to obtain a solution of the model. Subsequently, the model is used to simulate an ideal contact between an obstacle and the vibrissa. This simulation considers a quasi-static sweep of the artificial vibrissa with the contour of a profile, while measuring and recording the forces and moment at the base. This procedure is then repeated in combination of a distributed force acting on the vibrissa, simulating the effect of a fluid flow. Two types of contact phases are identified and the conditions for each one are set. Finally, the measured quantities, which represent the observables an animal solely relies on, are used to obtain the magnitude of the fluid load and to reconstruct the profile contour of the obstacle. The developed model is used again for the reconstruction, an analysis of the observables is performed to identify and predict which contact phase the vibrissa is in. The results successfully show identification of the fluid flow load as well as reconstruction of the profile, the difference between the reconstructed profile and the original profile is then calculated as a measure of reconstruction quality.

Kurzzusammenfassung

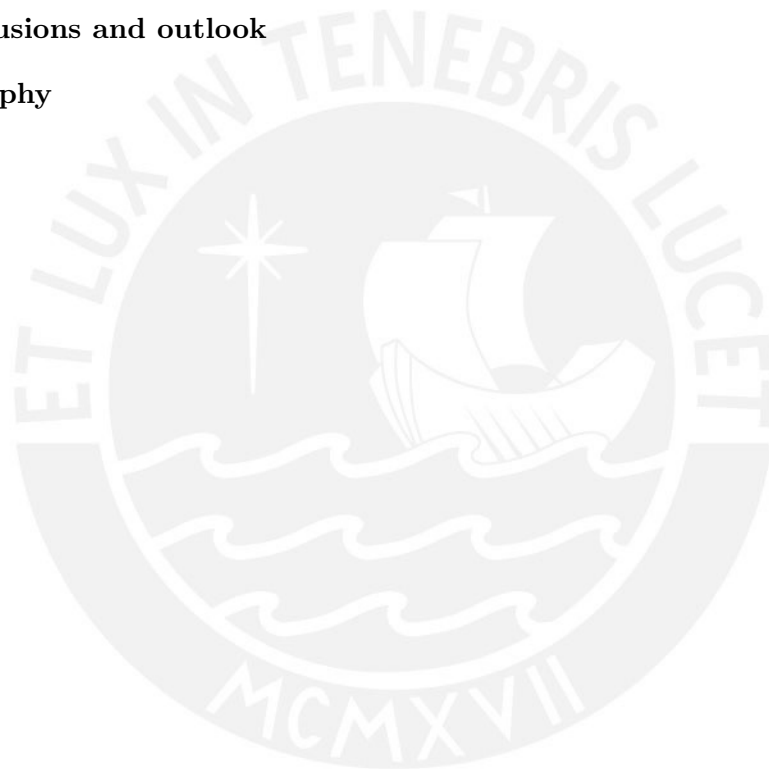
Die folgende Arbeit ist ein Teil eines Forschungsprojekts, das Vibrissen-inspirierte Tastsensoren für Objekt- und Strömungserkennung zu analysieren versucht. Der Schwerpunkt dieser Arbeit ist die Entwicklung eines technischen und mathematischen Modells für Objekterkennung unter dem Einfluss einer Strömung. Dazu wird ein mechanisches Modell auf Basis der nicht-linearen Euler-Bernoulli Biegungstheorie entwickelt. Das Modell enthält Hauptmerkmale, die in einer natürlichen Vibrisse gefunden werden, z.B. intrinsische Vorkrümmung, die Veränderung des Querschnitts, elastische Lagerung. Diese Hauptmerkmale werden als Parameter des Modells dargestellt. Das Modell wird dann einer Kontakt- und einer Strömungsbelastung ausgesetzt, die durch eine konzentrierte Kraft und eine verteilte Kraft repräsentiert werden. Dann wird das Modell in eine dimensionslose Form für weitere Untersuchungen transformiert. Eine Variation der Größe dieser Lasten, sowie die Vibrissen-Parameter wird analysiert. Eine direkte numerische Näherung durch das Finite-Differenzen-Verfahren wird zusammen mit dem Schießverfahren verwendet, um eine Lösung für das Modell zu erhalten. Danach soll der Kontaktvorgang zwischen Objekt und Vibrisse simuliert werden. Dabei wird ein quasi-statisches Vorbeiziehen der Vibrisse an der Objektkontur betrachtet, während die Lagerreaktionen bestimmt und aufgezeichnet werden. Diese Prozedur wird dann in Kombination einer Strömungsbelastung wiederholt, die eine Strömung simulieren soll. Es werden zwei Arten von Kontaktphasen identifiziert und die Bedingungen für jede Gruppe festgelegt. Schließlich werden die gemessenen Größen verwendet, um die Größe der Strömungskraft zu bestimmen und die Profilkontur der Oberfläche zu rekonstruieren. Das entwickelte Modell wird wieder für die Rekonstruktion verwendet, eine Analyse der Observablen wird vorgenommen, um zu identifizieren und vorherzusagen, in welcher Kontaktphase die Vibrisse ist. Die Ergebnisse zeigen eine erfolgreiche Identifikation der Fluidströmungsbelastung sowie eine Rekonstruktion des Profils, die Differenz zwischen dem rekonstruierten Profil und dem Originalprofil wird dann als ein Maß für die Rekonstruktionsqualität berechnet.

Contents

Declaration	i
Abstract	ii
Kurzzusammenfassung	iii
List of abbreviations	vii
1 Introduction	1
1.1 Motivation	1
1.2 Problem statement	1
1.3 Overview	2
2 State of the Art	3
2.1 Fundamentals of tactile sensing with Vibrissae	3
2.1.1 Vibrissae description	3
2.1.2 Form and geometry	5
2.1.3 Material properties	9
2.1.4 Follicle sinus complex	10
2.1.5 Main functions	11
2.2 Prototypes and application	12
2.2.1 Whisking robots	13
2.2.2 Platforms for fine work	15
2.2.3 Flow detecting sensors	16
2.3 Mechanical models of vibrissa behavior	18
2.3.1 Models with concentrated load at free end	19
2.3.2 Models with distributed and combined loading	23
2.4 Numerical procedures	26
2.4.1 Runge-Kutta Methods (RK)	26
2.4.2 Non-linear finite difference method	28
2.4.3 Bisection Method	30
2.5 Concretization of thesis goals	30
3 Formulation of the mechanical-mathematical problem	32
3.1 General model	32
3.2 Deduction of the equation of the system	33
3.2.1 Geometry of the vibrissa	33
3.2.2 Geometry of the elastica curve	35
3.2.3 Euler-Bernoulli equation	35
3.2.4 Analysis of the cross-section	36
3.2.5 Definition of dimensionless parameters	37
3.2.6 Dimensionless form of the system equation	38

3.2.7	Main set of parameters for investigations	39
3.3	Load scenarios	40
4	Preliminary studies: mechanical behavior of beams under various load scenarios	41
4.1	General solution procedure	41
4.2	Concentrated force at the free end	42
4.2.1	Case 1: Direction preserving tip load	42
4.2.2	Case 2: Angle preserving tip load	46
4.3	Distributed load along the shaft	48
4.3.1	Case 3: Rigid support, constant cross section and straight beam . .	48
4.3.2	Case 4: Elastic support, constant cross section and straight beam . .	50
4.3.3	Case 5: Rigid support, conical, straight beam	51
4.3.4	Case 6: Elastic support, conical, straight beam	52
4.3.5	Case 7: Rigid support, constant cross section, pre-curved beam . . .	53
4.3.6	Case 8: Elastic support, constant cross section, pre-curved beam . .	55
4.3.7	Case 9: Rigid support, conical and pre-curved beam	55
4.3.8	Case 10: Elastic support, conical and pre-curved beam	56
4.4	Combined loading	59
4.4.1	Case 11: Combined load, uniform beam, no pre-curvature, rigid support	59
4.4.2	Case 12: Combined load, uniform beam, no pre-curvature, elastic support	59
4.4.3	Case 13: Combined load, tapered beam, no pre-curvature, rigid support	61
4.4.4	Case 14: Combined load, tapered beam, no pre-curvature, elastic support	61
4.4.5	Case 15: Combined load, uniform beam, pre-curvature, rigid support	62
4.4.6	Case 16: Combined load, uniform beam, pre-curvature, elastic support	63
4.4.7	Case 17: Combined load, tapered beam, pre-curvature, rigid support	64
4.4.8	Case 18: Combined load, tapered beam, pre-curvature, elastic support	65
4.5	Comparison of results with FEM-software	66
4.6	Influence of each parameter	67
4.7	Summary and comments	68
5	Obstacle contour contact under the influence of a fluid flow	69
5.1	Considerations for obstacle/fluid flow detection	69
5.1.1	General considerations	69
5.1.2	Considerations for the fluid flow	70
5.2	General scenario for obstacle/fluid flow detection	70
5.2.1	Vibrissa only under the influence of the fluid load	70
5.2.2	Vibrissa contact with the obstacle	71
5.2.3	Vibrissa separation from the obstacle	73
5.3	Obstacle contour contact	73
5.3.1	Case 1: Contact considering different fluid loads	75
5.3.2	Case 2: Contact considering different conicity parameters	78
5.3.3	Case 3: Contact considering different torsional stiffness at the base .	81
5.3.4	Case 4: Contact considering different pre-curvatures	84
5.3.5	Case 5: Contact with all previous considerations	88
5.4	Comparison between a experimental sweep and a theoretical sweep	91
5.5	Summary and comments	93

6	Contour profile reconstruction and fluid flow identification	94
6.1	Fluid flow detection	94
6.2	Reconstruction of profile	95
6.2.1	Determination of first contact phase	97
6.2.2	Determination of contact phase of any point	97
6.3	Result sets	97
6.3.1	Case 1: Contact considering different fluid loads	99
6.3.2	Case 2: Contact considering different conicity parameters	100
6.3.3	Case 3: Contact considering different torsional stiffnesss at the base	101
6.3.4	Case 4: Contact considering different pre-curvatures	102
6.3.5	Case 5: Contact with all previous considerations	103
6.3.6	Experimental case	104
6.4	Summary and comments	104
7	Conclusions and outlook	106
	Bibliography	109



List of Abbreviations

- AP : angle preserving
- AUV : autonomous underwater vehicle
- CFD : computational fluid dynamics
- BVP : boundary-value problem
- DP : direction preserving
- FDM : finite difference method
- FEM : finite element method
- FSC : follicle sinus complex
- IVP : initial-value problem
- ODE : ordinary differential equation
- RK : Runge-Kutta method
- RK2 : second order Runge-Kutta method
- RK4 : fourth order Runge-Kutta method
- VIV : vortex induced vibrations

Chapter 1

Introduction

1.1 Motivation

Nature offers a wide range of solutions and adaptations to many situations and in many contexts. Human kind, with the goal of making life easier and solve everyday problems, has been looking into nature for inspiration [Vincent et al. 2006]. Biomimetics (biomimicry, bionics, biognosis, bio-inspired design) is defined as the study and application of nature's methods and principles to modern science and engineering [Li 2008].

Sensors are a crucial part of everyday life, just as humans developed sensors also did nature for different purposes as: acoustic sensors based on bats, flow detector mimicking hair cells, collision avoidance using whiskers, elastic wave sensors, fire monitoring, smell and taste sensing [Bar-Cohen 2006].

This research is part of an investigation project at TU Ilmenau, which consists on studying and developing tactile sensors for surface and flow detection inspired in *whiskers or vibrissae*. The goal is to develop models for tactile sensors to detect direction and magnitude of fluid flows as well as to identify the contour profile of obstacles. The first step to achieve this goal is to determine the mechanical response and behavior of a vibrissa under different *fluid loads* and considering various characteristics found in natural vibrissae. The focus and goal of this master thesis is to determine such behavior in order to set the foundation for future research and complement current investigations at the university.

1.2 Problem statement

Vibrissae of various animals can be modeled as a cantilevered beam under different kinds of loading and support conditions, effects as pre-curvature and conicity can also be accounted for. All these considerations in a physical model must be translated into differential equations that describe the behavior of large deflections of a beam. These differential equations are non-linear, non-autonomous, and a form of boundary-value problems (BVP); therefore numerical procedures for such problems are explored, developed and evaluated. After setting up the mathematical problem, MATLAB is used to implement the numerical procedures for the solution. There is no special focus on a certain type or form of vibrissa, that means all calculations must be in function of dimensionless parameters, so results are independent of the geometry, material properties, magnitude of forces applied, and rigidity of supports. This is also important for further comparison to the results obtained and those found in bibliography, experiments and between calculations with different methods.

Moreover, vibrissae geometry data and material properties are sought in the literature and used to create models in the commercial finite element method (FEM) program ANSYS. These results serve as comparison parameters for the analytical dimensionless results.

A "sweep" of an obstacle contour can be simulated, measuring and recording the observable

quantities or observables at the base, which represent the quantities an animal can feel. The influence of the fluid must be studied as well as the variation of the parameters and characteristics found on natural vibrissae. The vibrissa can be modeled as an elastic, slender beam capable of large deflections. The following steps have been proposed for the approach of the problem:

- become acquainted with non-linear beam theory;
- review corresponding literature of flow detection;
- set up MATLAB programs for the analytical dimensionless problem;
- use the model to gain insight into the influence of different load magnitudes and parameters;
- simulate the contact between a vibrissa and an obstacle under the influence of a fluid flow;
- set up the program to reconstruct the contour profile and check results.

1.3 Overview

The content of the thesis at hand is organized as follows:

- *Chapter 2:* In this chapter, the fundamentals of tactile sensing with vibrissae are stated, as well as a review of practical applications of tactile sensing a flow detection. Also different models to analyze the behavior of vibrissae are reviewed.
- *Chapter 3:* The general physical problem of a vibrissae under a general loading is formulated. The general definitions and parameter are defined, as well as the study cases and load scenarios.
- *Chapter 4:* Various load scenarios with different considerations are studied in order to study the influence of each of the considerations to the general model.
- *Chapter 5:* The obstacle contour contact under fluid influence problem is formulated, using the model developed in previous chapters. Several cases are studied to analyze the influence of each vibrissa parameter on the measurements.
- *Chapter 6:* Using the results from the previous chapter as input, an algorithm is developed to identify the fluid load and reconstruct the obstacle profile contour.
- *Chapter 7:* Conclusions and future work

Chapter 2

State of the Art

2.1 Fundamentals of tactile sensing with Vibrissae

2.1.1 Vibrissae description

Vibrissae or tactile hairs are a specialized type of hair that act as tactile receptors [Pearson 1962] and are a characteristic found on many mammals, they can be found in many sizes and various parts of the body, but the most and frequently studied are the facial or mystacial vibrissae, also called “whiskers” [Prescott et al. 2011].

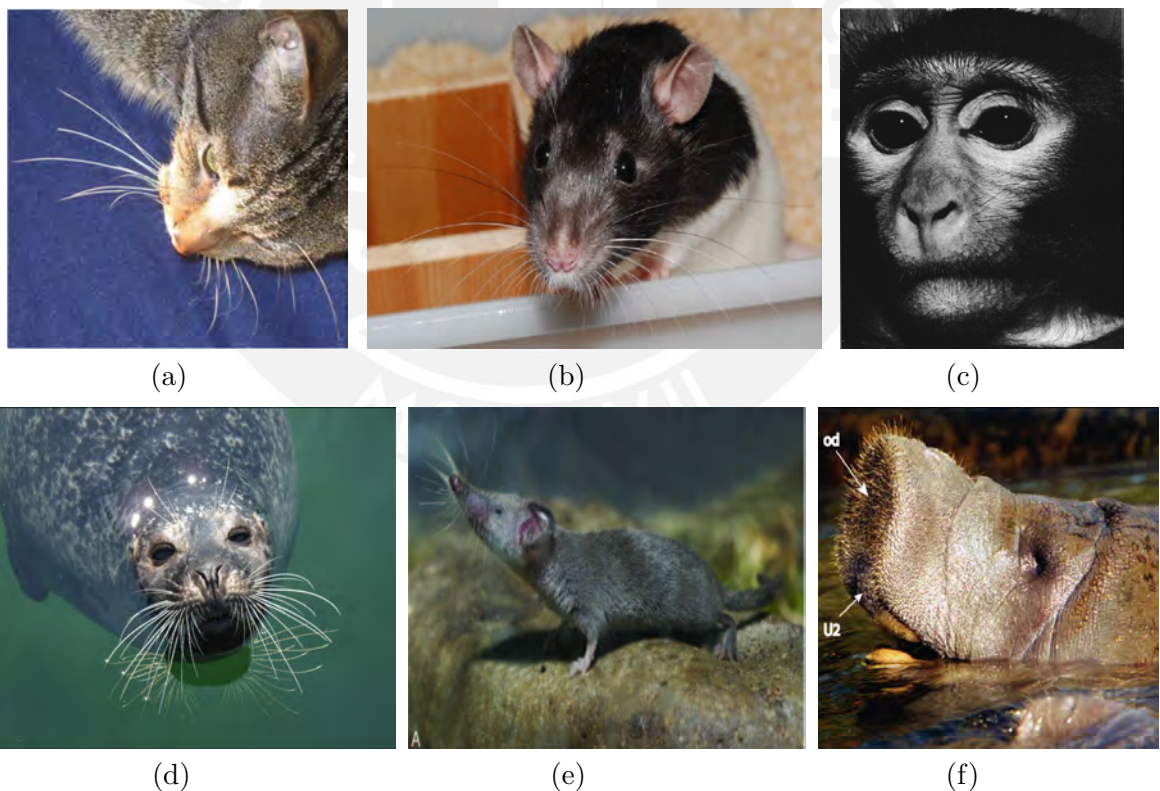


Figure 2.1: Examples of whiskers found on land and sea animals: (a) Whiskers of a house cat “Alfred” [Behn et al. 2009]. (b) Vibrissae on a common rat [Prescott et al. 2011]. (c) Facial vibrissae on a rhesus monkey [Van Horn 1970]. (d) Facial vibrissae of “Henry”, a seal. Rostock Marine Science Center (<http://www.marine-science-center.de/henry.html>). (e) Etruscan shrew and its whiskers [Roth-Alpermann and Brecht 2009]. (f) Manatee face, showing its tactile hairs [Reep and Sarko 2009].

As stated by [Ahl 1986], the main differences between vibrissae and pelage hair are: vibrissae are longer and thicker than normal hair (see Fig. 2.1); the follicles from which they are grown are highly innervated and contain blood-filled sinus tissues, these are known as follicle sinus complex (FSC); and each follicle is precisely represented in the sensory cortex of the brain.

Distribution

Vibrissae can be found on the majority of mammals [Ahl 1986], with the exception of humans and some non-primate species [Van Horn 1970], [Pocock 1914]. A general classification of vibrissae was done by [Ahl 1986] and divides them based solely on the body part found, it is worth noticing that not all animals show vibrissae in the same areas, some may lack them in certain body parts:

- *Facial vibrissae*

- Mystacial: found above the lips and arranged in well defined rows [Ahl 1986], [Hanke and Dehnhardt 2015]. They are present in almost all mammals.
- Rhinal: typically found above the nare of pinnipeds and usually exactly one above each nare [Hanke and Dehnhardt 2015].
- Submental: found below the lips and chin, not always symmetrical.
- Interramal: in the mandibular symphysis [Ahl 1986].
- Supraorbital: above each eye, usually above its medial part [Ahl 1986].
- Suborbital: beneath the eye [Ahl 1986].
- Genal: in the cheek area [Ahl 1986].

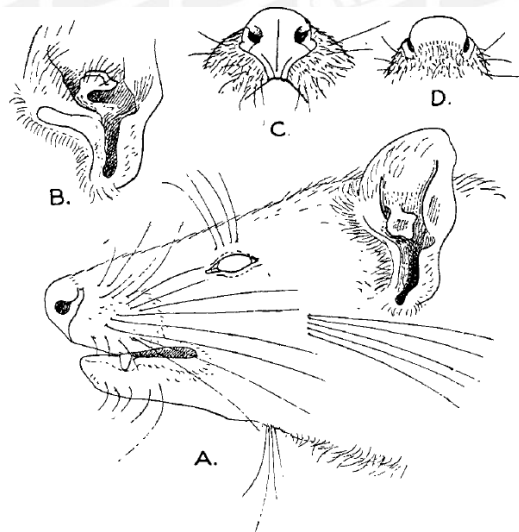


Figure 2.2: Facial features of the *Dasyurus maculatus*, showing its facial vibrissae [Pocock 1926].

- *Body vibrissae* Found on body parts other than the face area.

- Ulnar-carpal: one or more on the palmar surface of the forearm near the wrist [Ahl 1986].
- Medial antebrachial: in the middle of the forearm [Ahl 1986].
- Anconeal: near the elbow. Usually a single anconeal vibrissa per limb is found [Lyne 1952].

- Calcaneal: on the medial part of the ankle [Ahl 1986].
- Venter: on the ventral body surface [Ahl 1986].

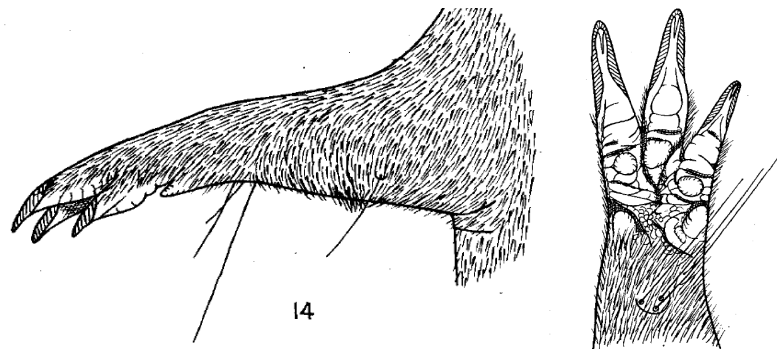


Figure 2.3: Frontal limbs of different bandicoots showing vibrissae [Lyne 1952].

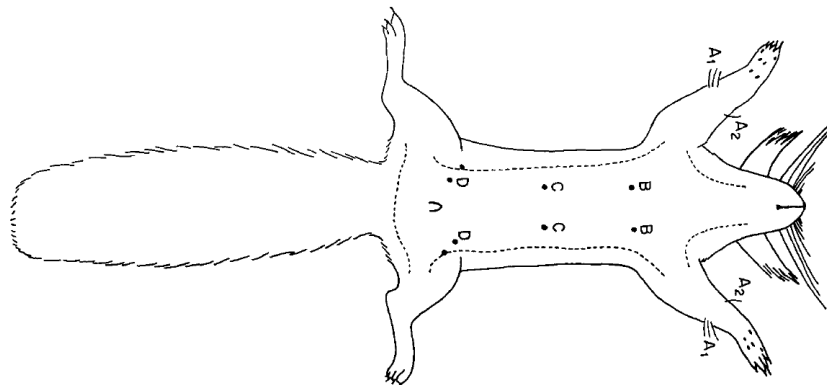


Figure 2.4: Location of venter vibrissae in the *Sciurus vulgaris* [Hyvärinen et al. 1977].

2.1.2 Form and geometry

The length and cross section of vibrissae varies from animal to animal and depending on their main function and body part where they are found. There is also a major variation between vibrissae found on land and sea animals.

The main characteristics of vibrissae can be summarized into certain parameters that further help to build a model:

Length

Depending on the the body part and animal, vibrissa length varies widely. For instance, rat mystacial vibrissae range between 15 and 50 mm [Prescott et al. 2011] (see Fig. 2.5). Seal vibrissae typically range from 50 to 90 mm [Miersch et al. 2011], [Hans et al. 2014]. Chinchillas have vibrissae ranging from 100 to 130 mm, and are up to one third of the body length [Spotorno et al. 2004].

The length of the vibrissae also depends on the mammal's habits. One way to spot this difference is using the ratio of the vibrissa length V and the head length H (for mystacial vibrissae) [Ahl 1987]. For instance, in different species of squirrels the V/H ratio depends on their habit groups (terrestrial, arboreal or aerial). The most developed and long are those that correspond to nocturnal, arboreal and areal squirrels (V/H ratio of 1.670 to

2.111) that cannot depend entirely on their eyes [Ahl 1987].

Due to the large variation of length in vibrissae, the results obtained should be independent on the vibrissa length.

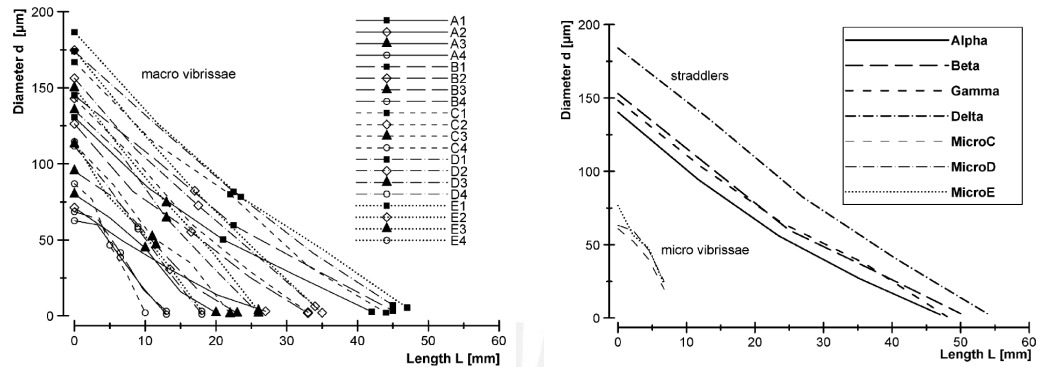


Figure 2.5: Diameter over arc length of rat mystacial vibrissae [Voges et al. 2012].

Composition

The cross section of a vibrissa consists of three layers: an outermost layer called the cuticle, followed by the cortex, and then the medulla, which is hollow [Hartmann 2015]. This explains why the bending stiffness varies along the length of the vibrissa. Even though the medulla is hollow, mechanical models and prototypes usually consider the vibrissae to be a solid material (see Fig. 2.6).

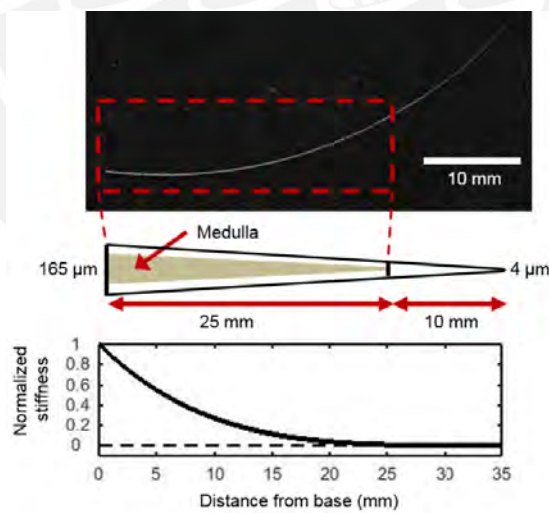


Figure 2.6: Simplified internal composition of a vibrissa and the corresponding variation in stiffness [Hartmann 2015].

Intrinsic curvature

As seen in the many examples of Fig. 2.1, the vibrissae are not straight, they possess an intrinsic curvature contained in a plane. Most of the studies, focusing on the intrinsic curvature of vibrissae, focus on rodent whiskers. However, the findings of such studies can still be used to understand the curvature of a general vibrissa.

The curvature can be approximated intuitively by a quadratic or parabolic fit [Knutsen

et al. 2008], [Hartmann 2015]. A general parabolic fit has the form $y = ax^2 + bx + c$, it can be further simplified with only one coefficient $y = ax^2$ as seen in the example in Fig. 2.7. Moreover, the quadratic coefficient a varies between columns of mystacial vibrissa (see Fig. 2.8).

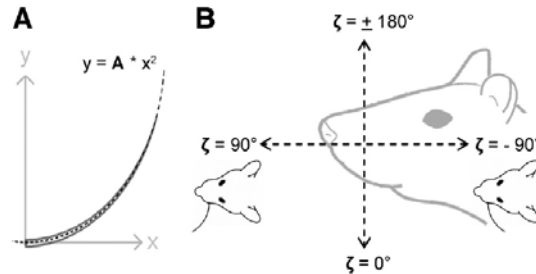


Figure 2.7: Quadratic fit and orientation of the curvature of rat vibrissae. [Quist and Hartmann 2012].

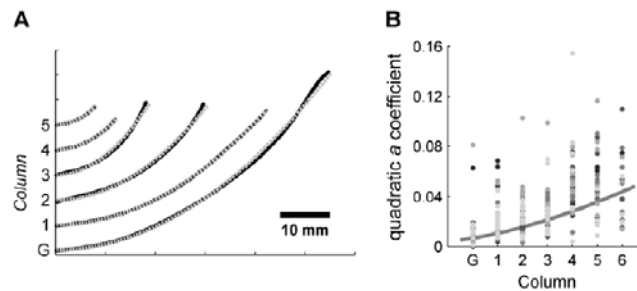


Figure 2.8: Quadratic fit and quadratic coefficient a for different whiskers in different columns [Towal et al. 2011].

Although a parabolic fit provides a close approximation, it is not a coordinate-free representation. An alternative to the quadratic fit is the Césaro coefficients $\kappa(s) = As + B$ [Towal et al. 2011]. In mystacial rat vibrissae, there is a further linear relationship between A and B : $A = -1.747B - 1.644$ (see Fig. 2.9).

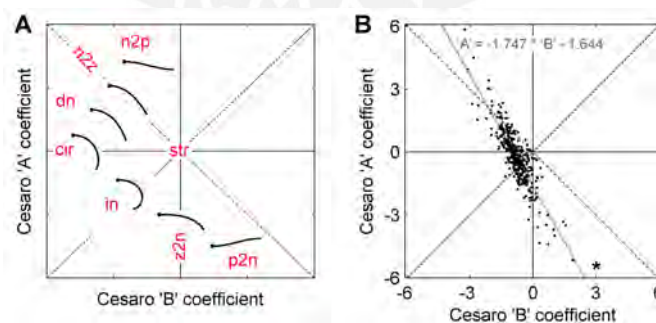


Figure 2.9: Correlation between the Césaro coefficients for rat mystacial vibrissae [Towal et al. 2011].

Diameter variation and form

Vibrissae also feature conicity and other variations of the cross section, this variations however depend on the function of the vibrissa. On land animals, vibrissae typically taper approximately linearly from the base to the tip [Voges et al. 2012], [Hartmann 2015], as

Table 2.1: Explanation of abbreviations in Fig. 2.9. Adapted from Table S2 of [Towal et al. 2011].

Notation:	Meaning:	A	B	Curvature behavior
<i>str</i>	Straight	$A = 0$	$B = 0$	no curvature
<i>cir</i>	Circular	$A = 0$	$B \neq 0$	constant curvature
<i>z2n</i>	zero to negative	$A < 0$	$B = 0$	straight at base and becomes negative
<i>n2z</i>	negative to zero	$A = -B$	$B < 0$	negative at base and becomes straight
<i>in</i>	Increasingly negative	$A < 0$	$B < 0$	negative at base and increases negatively
<i>dn</i>	decreasingly negative	$A > 0$	$B < 0$	negative at base, becomes less negative but not straight
<i>dn</i>	decreasingly negative	$A < -B$	$B < 0$	negative at base, becomes less negative but not straight
<i>n2p</i>	negative to positive	$A > -B$	$B < 0$	negative at base and becomes positive at tip, similar to sigmoid curve
<i>p2n</i>	positive to negative	$A < -B$	$B > 0$	positive at base and becomes negative at tip, similar to sigmoid curve

shown in Fig. 2.5. The ratio between the base and tip diameter varies largely from species to species, it can be as low as 4 to 10, and as large as 15 to 30 in red foxes, as well as 12-14 in seals [Williams and Kramer 2010]. In sea animals, vibrissae are not only conical, upon closer look they usually reveal undulations as shown in Fig. 2.10. This undulations suppress the formation of vortices and vortex induced vibrations (VIV) that usually arise with other cross section geometries [Hanke et al. 2010], [Morrison et al. 2016] (see Fig. 2.11) and help stabilize the force measurement performed by the vibrissae, as shown in Fig. 2.12.

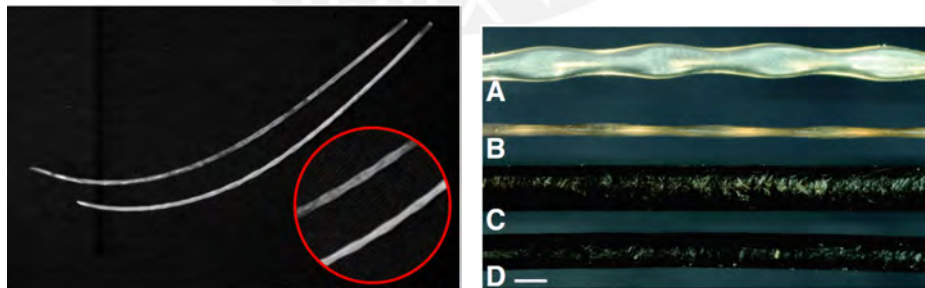


Figure 2.10: Left: Natural curvature of harbor seal vibrissae. In the red circle the undulations can be seen [Valdivia y Alvarado et al. 2012]. Right: Comparison found in [Hanke et al. 2010] and [Miersch et al. 2011] in structure of harbor seal (A,B) and califonia sea lion (C,D) vibrissa; Dorsal (A,C) and frontal (B,D) view. Scale bar: 1 mm.

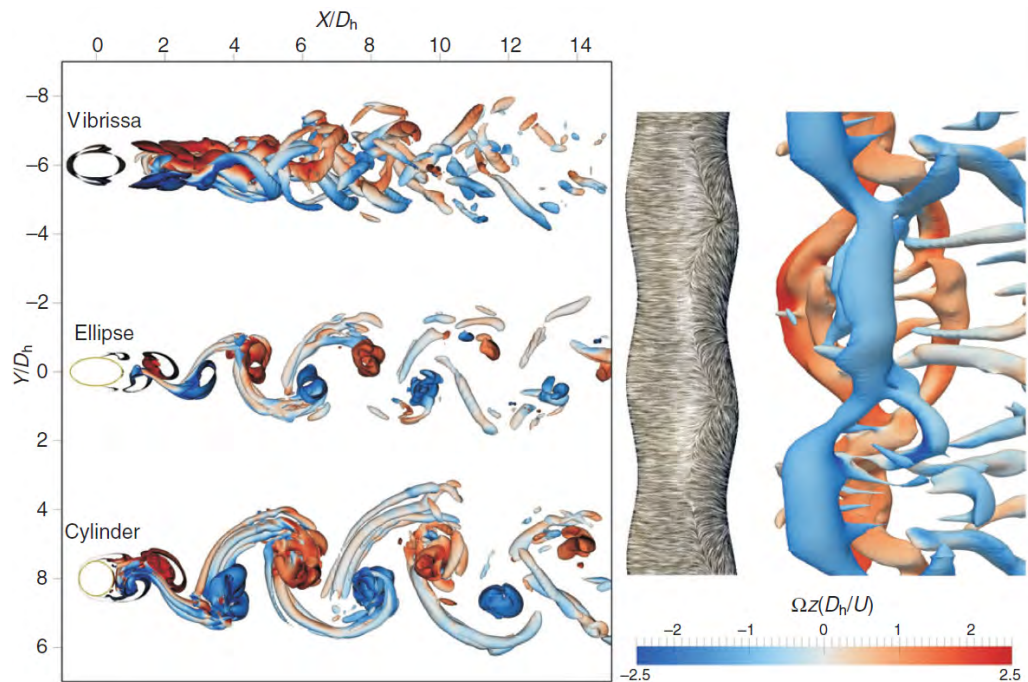


Figure 2.11: Numerical simulation of the wake flow behind cylinder bodies at Re of 500 [Hanke et al. 2010].

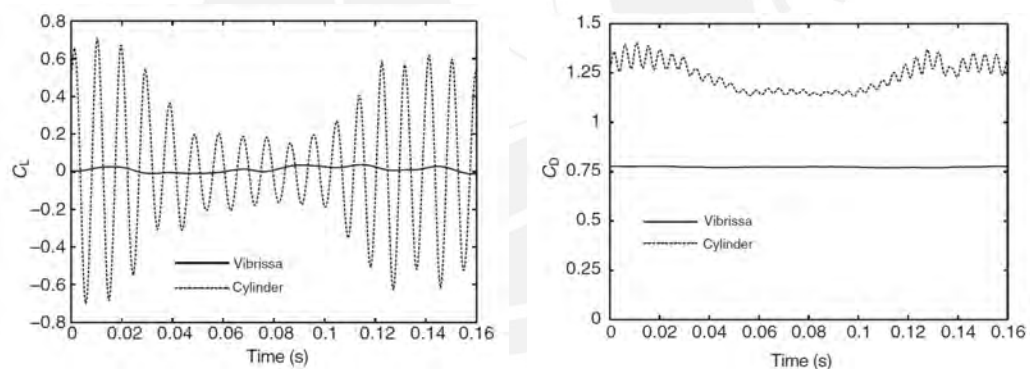


Figure 2.12: Comparison by [Hanke et al. 2010] of the lift C_L and drag C_D coefficient of a cylinder and a vibrissa.

2.1.3 Material properties

When analyzing the mechanical behavior of any material (including vibrissae), the properties that describe how the material deforms under external forces are the elasticity or Young modulus E and shear modulus G (the Poisson modulus ν is also used). When working in three dimensions (3D) mechanics or with large shear strain (as in a Timoshenko beam), G gains importance [Hartmann 2015]. In two dimensions (2D) bending, usually only E is needed, see [Gere and Goodno 2008], [Hibbeler 2011], [Beer et al. 2012]. However, just as the cross section, the elasticity modulus also changes along the length of a vibrissa and depends also if the vibrissa is dried or submerged in water (for sea mammals) as seen in Fig. 2.13. Moreover, the bending stiffness EI decreases dramatically along the length in a fifth-order exponential decrease curve [Hans et al. 2014].

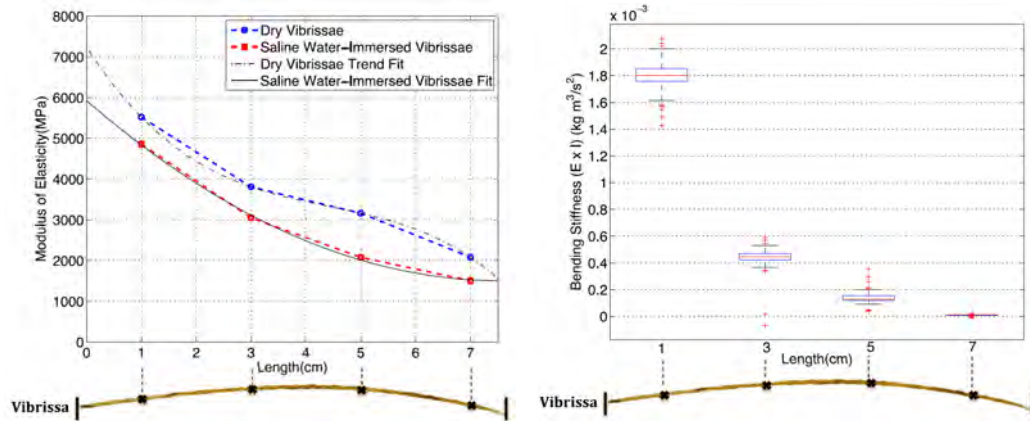


Figure 2.13: Moduli of elasticity along the length and bending stiffness EI variation along the length of a vibrissa of a harbor seal [Hans et al. 2014].

The Young modulus of vibrissae shows large differences according to the position on the mystacial pad. The authors in [Voges et al. 2012] state that the value is around 8 GPa, higher than other hair without sensory tasks such as human hair (3.2 GPa). Another study by [Birdwell et al. 2007] measures the Young’s modulus on different vibrissae on various positions along the length of the vibrissa, their results show a large variation between values of E just depending on the position of the whisker varying from 1.4 to 6.25 GPa.

Table 2.2: Geometry data and average elasticity modulus determined by [Birdwell et al. 2007].

Vib.	Arc Length	ϕ	E
	mm	mm	GPa
β	66.2	0.225	1.40
γ	60.3	0.199	3.75
A1	51.7	0.16	2.75
E2	48.1	0.232	1.9
B2	41.1	0.169	2.3
E3	33.3	0.189	3.9
C3	21.5	0.119	6.25

2.1.4 Follicle sinus complex

Vibrissae are not rigidly clamped to the skin of the animal, instead, they are connected to their own FSC. The FSC presents mechanoreceptors, which are stimulated by the forces and effects of the environment on the vibrissa shaft. The vibrotactile information is then passed to the central nervous system of the animal. Many animals also have musculature in their FSCs, which allow them to move their vibrissae to “look” for objects; this behavior is known as *active sensing*. Some other animals have a very reduced vibrissal movement range and rely mainly on *passive sensing*, in other words, they wait for the object to intercept the vibrissae.

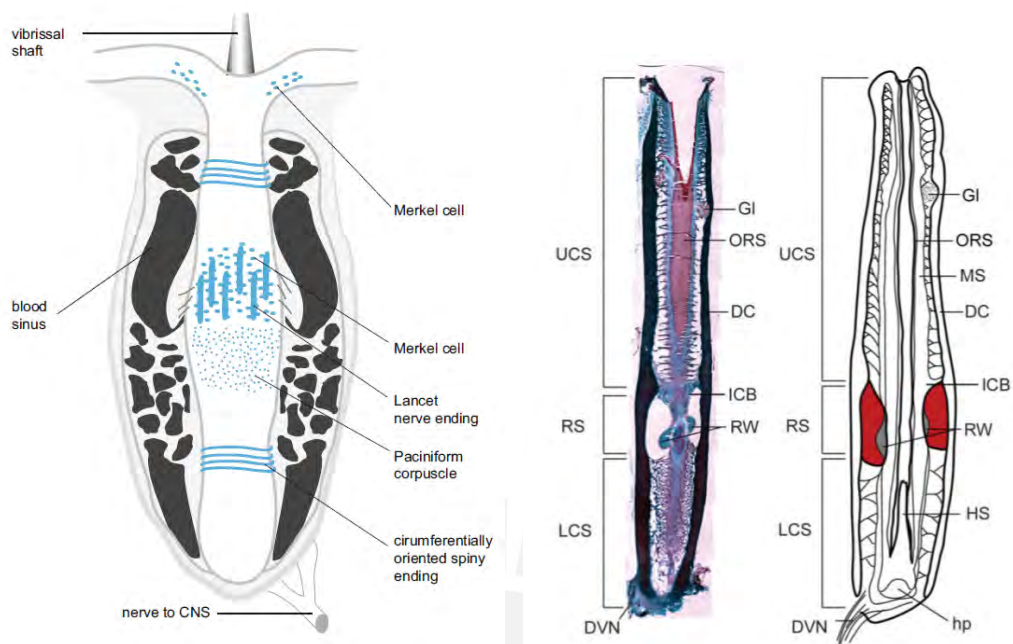


Figure 2.14: Left: Scheme of the follicle sinus complex with various types of receptors (blue) [Behn et al. 2013]. Right: Longitudinal section and scheme of the FSC of a bearded seal [Marshall et al. 2006].

2.1.5 Main functions

- *Localizing*

Rats typically use their vibrissae to locate gaps, objects and obstacles at close quarters [Prescott et al. 2011]. The main coding dimensions measured by vibrissae are: space (object location), intensity (contact parameters such as force, velocity and direction), time (timing of whisker deflections), and posture (position of the object relative to the the head) [Ahissar and Knutsen 2011].

- *Orienting*

Cotton rats use their vibrissae to maintain body position while swimming and the Greenland seal uses vibrissae when resurfacing to notify that it can open its nostrils to breath [Ahl 1986].

- *Tracking*

Tracking is a very important function for predators; they use it to survey and manipulate prey and use their vibrissae to complement other senses. Clipping the vibrissae of grasshopper mice makes them take more time to catch the prey. Despite of having good eyesight at long distances, at close quarters cats use their vibrissae to search and kill prey [Ahl 1986]. Harbor seals use their vibrissae to pick up the hydrodynamic trail of prey fish specially in dark and murky waters [Morrison et al. 2016], [Dehnhardt et al. 2001]; they can track Karman street-like wakes, helical vortices and various wakes, including those of other seals, up to 35 seconds after the wake creation [Hans et al. 2014].

- *Texture discrimination*

Rats can be trained to discriminate multiple textures (microgeometry) with similar sensory thresholds as humans. When a vibrissa moves along a surface, it vibrates and generates a kinetic signature which is the basis of the texture discrimination [Prescott et al. 2011], [Arabzadeh et al. 2009].

- *Shape discrimination*

Rats and shrews are able to identify certain macrogeometric characteristic of prey [Prescott et al. 2011] through oscillatory movements of the vibrissae [Tuna et al. 2012]. However, this functions have been more developed in prototypes (see Section 2.2) to identify shapes.

- *Numerical discrimination*

Results of experiments performed by [Davis et al. 1989] suggests that rats can be trained to discriminate between two, three and four vibrissal deflections. The results indicate some sort of vibrissal short term memory and enumerative capacity [Prescott et al. 2011].

- *Air flow/water currents/vibration*

Harbor seals and sea lions use their vibrissa to pick up vibrations and vortices in the water to identify prey and other seals in their vicinity even in complete darkness [Beem et al. 2012], [Dehnhardt et al. 2001], [Hanke et al. 2010], [Miersch et al. 2011], [Hans et al. 2014]. It is reported that harbor seals can sense such vortices up to 30 seconds after their formation [Dehnhardt et al. 2001].

2.2 Prototypes and application

Sensing is not only a fundamental survival tool for animals, as stated before, humans can also learn and apply such techniques developed by nature. Robotics is a field where sensing is of great importance, artificial whisker systems began in the mid 1980s. Although tactile sensors exist in robotics, they are used as a complement for other sensors, usually only in detecting whether there is physical contact [Prescott et al. 2009]. Usually tactile sensors are sensor array designs, so they provide reliable and accurate data (data transduced is usually: simple contact, force magnitude, 3D shape, slip, thermal properties, etc.) [Nicholls and Lee 1989].

Tactile sensing using vibrissa or whisker like sensors proves to have advantages over other types of sensors, for instance:

- In terrain identification, vehicle-mounted inertial sensors and visual sensors are limited by the mechanical response of the wheels and the assembly itself, which cannot be modified without affecting the mobility of the vehicle itself [Giguere and Dudek 2011].
- High precision and high confidence measurement in critical tasks such as heart motion during surgery usually needs redundant sensing systems, inertia sensors present drift problems and laser proximity are limited to one dimensional measurement. Whisker sensors prove to be a promising option [Bebek and Cavusoglu 2007].
- Although vibrissa-like sensors lack of long range sensing, they allow navigation and discrimination in dark and murky environments [Yokoi et al. 2005].
- Autonomous underwater vehicles (AUV) typically use acoustic technology, however these active devices typically need up to 40% of the probe total energy, and limit the mission length. Vibrissa-like sensors are a low energy and cost alternative [Beem et al. 2013].

2.2.1 Whisking robots

There has been research and development of robots that instead of robot vision, rely on arrays of tactile sensors (see Fig. 2.17) to survey the environment. Sensors can be used in one of two ways:

- *Active sensing*: consists on rotating the tactile sensor in search for obstacles. It is inspired in the “whisking” movements of certain animals. Some modules of vibrissa sensors with incorporated movement such as BIOTACT have been developed.

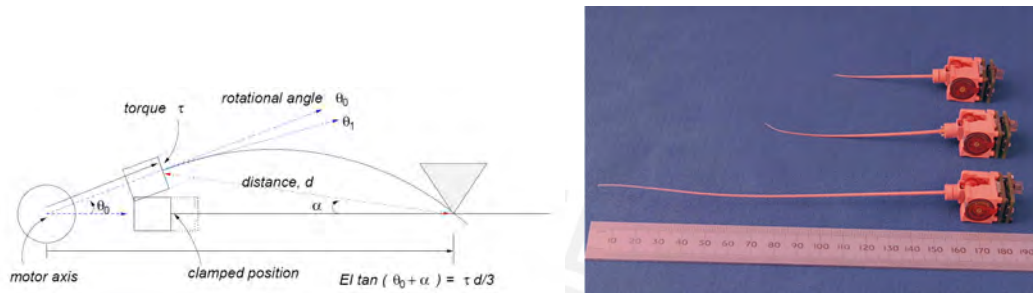


Figure 2.15: Left: Scheme of active sensing by a tactile sensor [Kim and Möller 2005], [Kim and Möller 2006]. Right: BIOTACT sensor module [Sullivan et al. 2012].

- *Passive sensing*: consists on moving the entire robot until the sensor intercepts an obstacle. Most of the tactile sensors work with this principle by default, and require to be mounted on other mobile platforms for active sensing.

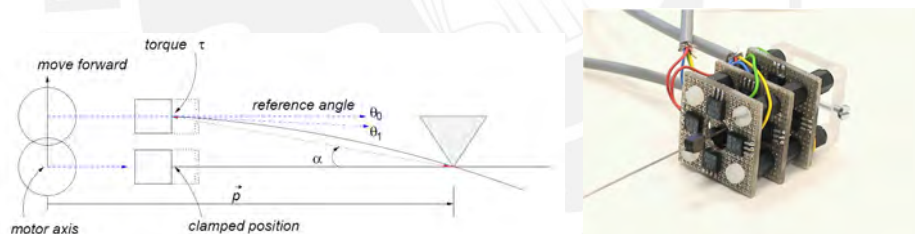


Figure 2.16: Left: Scheme of passive sensing by a tactile sensor. Right: Artificial whisker with magnetic sensors on three horizontal planes [Kim and Möller 2006].

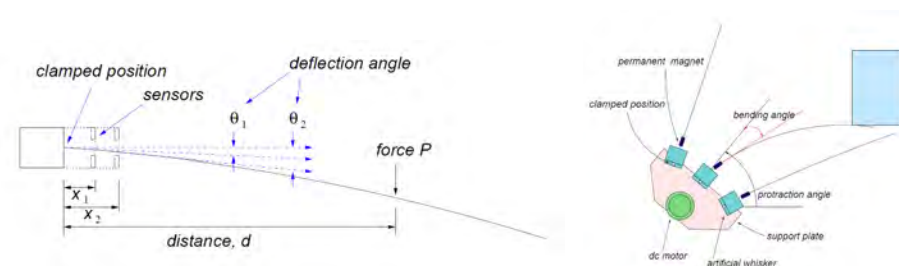


Figure 2.17: Scheme by [Kim and Möller 2006] of a tactile sensor and the array of tactile sensors.

Ganglion cells at FSC the base of the whisker encode deflection amplitude and velocity signals instead of torque. These signals are used to obtain location information of a target object [Kim and Möller 2005]. For this reason, sensors mounted on whisking robots, whether active or passive, are designed to measure deflection angles on different planes.

Whiskerbot

Whiskerbot is a robotic project that relies on six, 200 mm, glass-fiber composite whisker-like sensors (see Fig. 2.18) to survey the close environment. The support for each whisker consists on a plastic bobbin located on a shaft. Optical shaft encoders are used to derive the absolute angle of each whisker. Shape metal alloy fiber (BioMetal®) is wrapped around each bobbin and a electric current is applied, the current heats the BioMetal, contracting its fibers and simulating the “whisking” movement [Pearson et al. 2007].

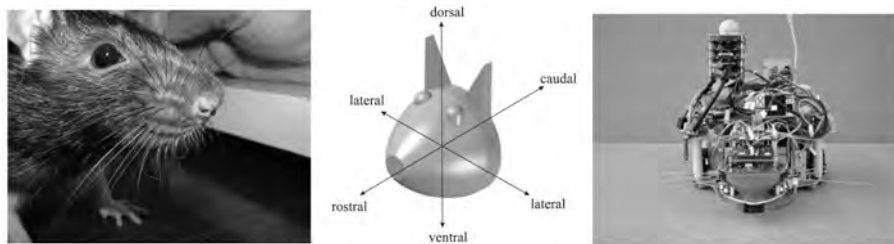


Figure 2.18: Comparison between a rat whiskers and Whiskerbot [Pearson et al. 2007].

SCRATCHbot robot

SCRATCHbot is a prototype designed for testing the utility of vibrissal sensing and mapping of indoor environments. This prototype is able to perform two coordinated movements: rapid whisker movement and quickly reposition the head to orientate the whisker array towards the object of interest (see Fig. 2.19) [Prescott et al. 2009].

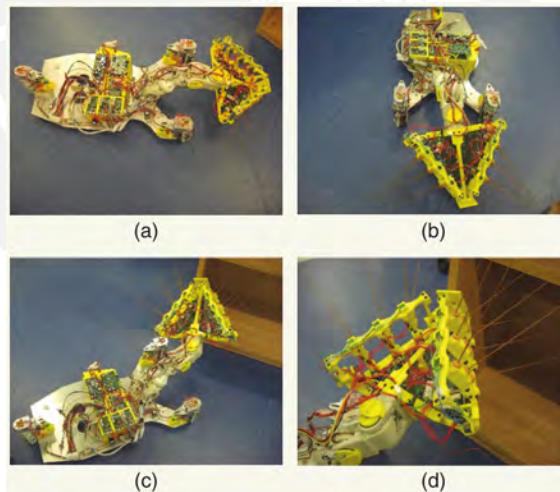


Figure 2.19: Different positions of the SCRATCHbot [Prescott et al. 2009].

Whiskers on a Koala-bot

Another project consists on tactile sensors in active sensing, mounted on a Koalabot robot. It is used for shape detection and discrimination of round objects with varying curvature, different lateral shapes (see Fig. 2.20). The project considers different alternatives to determine contact distance and horizontal and vertical profiles due to the vertical array of the whiskers (see Fig. 2.20) [Kim and Möller 2005], [Kim and Möller 2006], [Kim and Möller 2007].

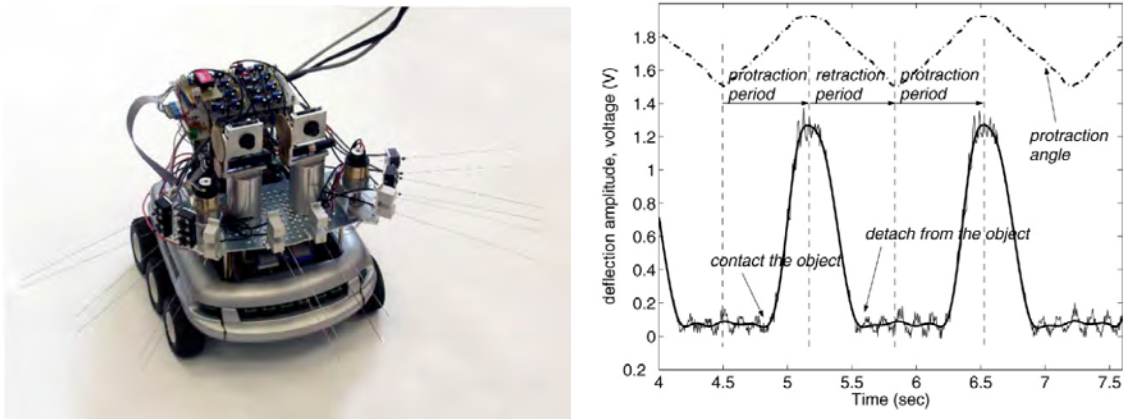


Figure 2.20: Whiskers mounted on a Koala-bot platform and the time course of the deflection amplitude when encountering an object [Kim and Möller 2007].

Feature recognition

In a similar manner, the Koala-bot can detect geometric profiles by arrays of vibrissae, the same principles can be applied to determine features in a surface with an array, as in Fig. 2.21. However, not only the position of the target object has to be determined, but the lateral slip due to friction has to be considered.

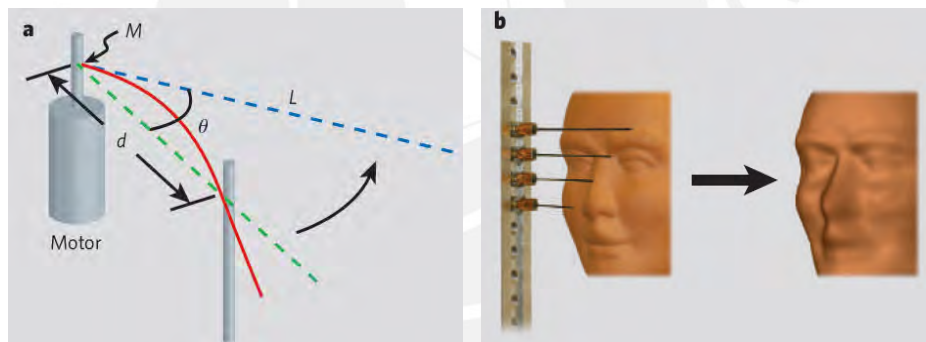


Figure 2.21: Whisker array to determine features in a surface [Solomon and Hartmann 2006], [Solomon and Hartmann 2008].

2.2.2 Platforms for fine work

This platforms are usually used to measure very small forces and used in working environments where high precision is needed, such as surgery rooms.

Tip force sensor for retina surgeries

A tip force sensor developed, inspired by a vibrissa, was developed by [Berkelman et al. 2003] to determine microsurgical forces in retina surgeries. This sensor is able to measure forces below 7.5 mN. Since these forces are below the human sensory threshold, the goal of project is to sense and amplify these forces in order to provide tactile feedback to the operator [Berkelman et al. 2003]. The sensor consist on an array of cantilever beams in a cross configuration (see Fig. 2.22)

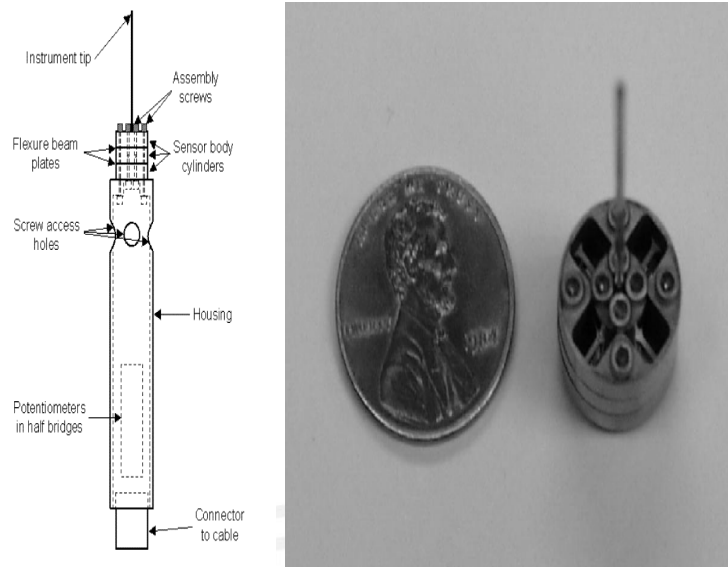


Figure 2.22: Tip force sensor developed by [Berkelman et al. 2003].

Sensors to register heart movements

Heart surgeries require redundant sensors to monitor the movement of the heart, the authors in [Bebek and Cavusoglu 2007] proposed two prototypes of whisker-like sensors to measure such movements to be mounted on surgical robots. The first sensor design consists of a linear position sensor and a deformable structure with strain gauges to measure the 3D position of the tip (see (a) in Fig. 2.23). The second sensor design consists on two deformable beams with strain gauges mounted on them and a linear position sensor. Both beams are rotated 90° with respect to their centroid to capture bending in two directions (see (b) in Fig. 2.23).

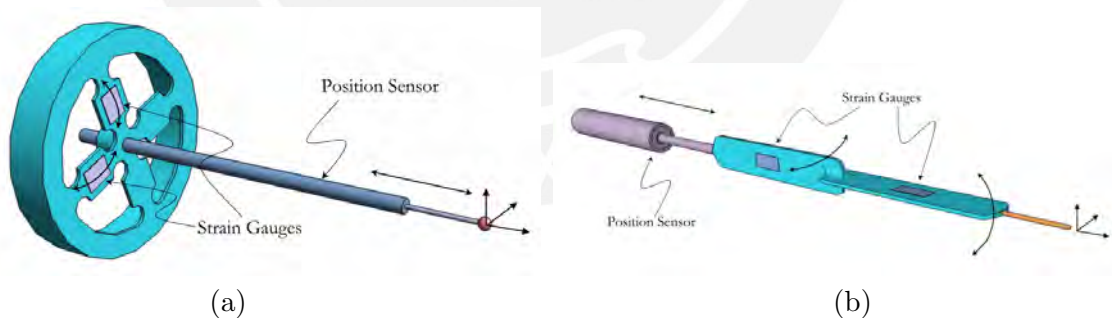


Figure 2.23: Proposed whisker sensors by [Bebek and Cavusoglu 2007].

2.2.3 Flow detecting sensors

Most of the focus on the development of vibrissa like sensors has been done on object detection and surface recognition. Only a small number of applications can be found including the sensing of flows; however there has been recent advances in sensors for such applications.

Bioinspired sensors for underwater applications

A design for bioinspired sensors was performed by [Valdivia y Alvarado et al. 2012], the mechanical model for the vibrissa sensor consists of a cantilever beam on elastic supports

(see Fig. 2.24) to simulate the follicles and determine the influence of the properties of the follicle on the dynamic response of the vibrissa. Since cylinders or cones produce Karman vortex streets (see Fig. 2.11), different geometries for a vibrissa sensor were studied (see Fig. 2.25).

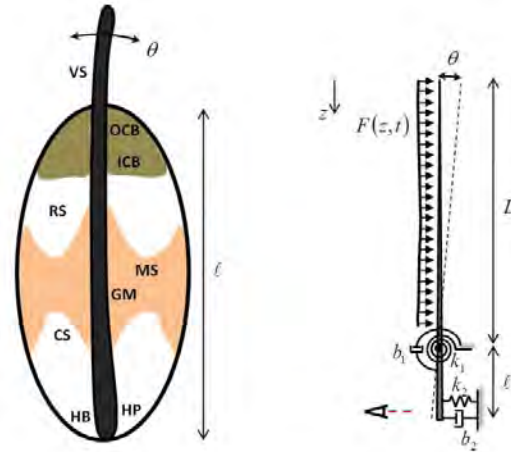


Figure 2.24: Model of the vibrissa-like sensor and the follicle [Valdivia y Alvarado et al. 2012].

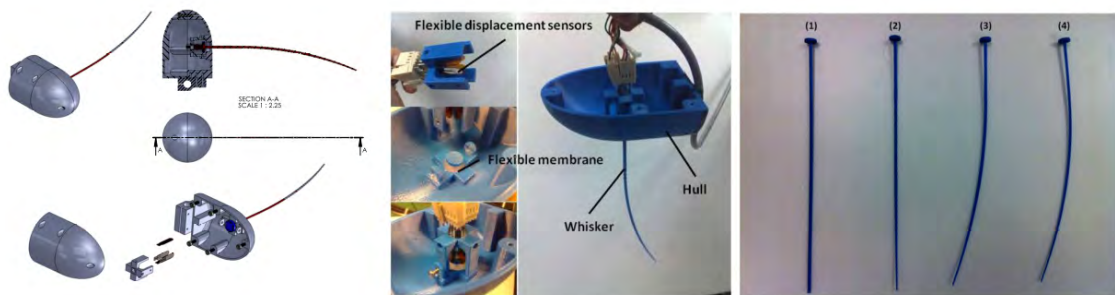


Figure 2.25: Design of a vibrissa like sensor for underwater applications [Valdivia y Alvarado et al. 2012].

The vibrissa sensors developed (in Fig. 2.25) have the following geometries: (1) straight cylinder, (2) straight cylinder with undulations, (3) curved smooth vibrissa, (4) curved vibrissa with undulations. This research helped to prove that curvature and undulations are key factors in reducing noise (e.g. VIV) [Valdivia y Alvarado et al. 2012].

Harbor seal flow sensor

A posterior study focuses on the influence on the geometry of harbor seal vibrissae and their ability to suppress vortex formation (see Fig. 2.11) to obtain more precise measurements. This geometry is however useful to detect incoming vortex. This solution proves to be low cost and low power, which makes it suitable for oceanographic missions [Beem et al. 2013].

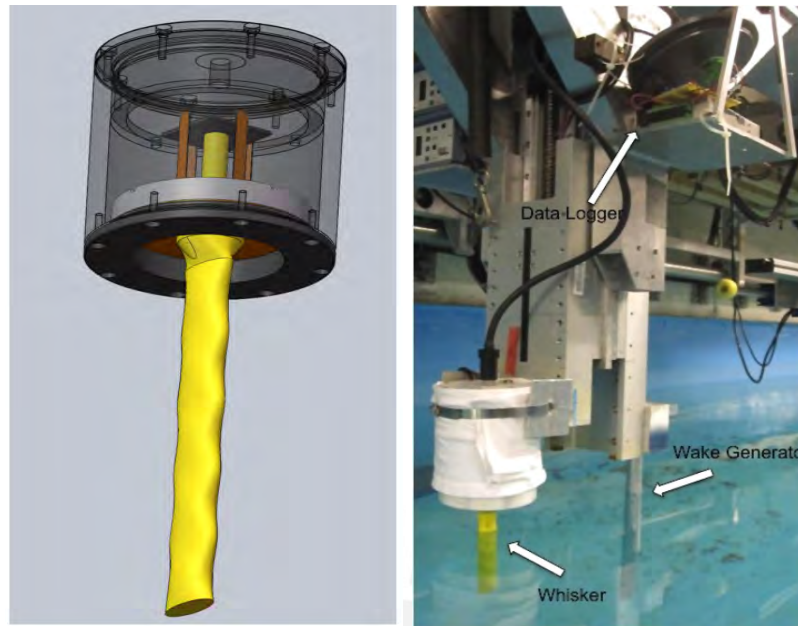


Figure 2.26: Harbor seal vibrissa inspired flow sensor and its experimental setup [Beem et al. 2012], [Beem et al. 2013].

As seen in Fig. 2.26, the vibrissa sensor features undulations along the length to mimic those found on harbor seals (see Fig. 2.10). The base is mounted on four bending sensors (orange) distributed by 90° . To avoid the access of water, a flexible membrane is used to protect the instruments and allow the movement of the vibrissa.

2.3 Mechanical models of vibrissa behavior

Vibrissae can be modeled as tapered cantilever beams that transmits mechanical information to mechanoreceptors in the follicle at the whisker base [Hartmann 2015], which in turn can be modeled as elastic support [Valdivia y Alvarado et al. 2012]. It has also been shown (see Figs. 2.17, 2.15 and 2.16) that the vibrissa is subjected to large deflections when encountering an object.

Models have been developed to understand the behavior of beams under large deflections. These models possess different considerations, loading, geometry, material properties, and numerical procedures to obtain the displacements of each point of the beam when loads are applied. The numerical procedures used are of crucial importance, since the equations that describe the *elastica* are non-linear, non-autonomous differential equations that usually do not have an algebraic exact solution and require iterative methods to be solved. After reviewing the corresponding literature in vibrissae study, two types of models of vibrissa could be identified:

- *Rigid body models.* As the name implies, the vibrissae is modeled as a rigid inverted pendulum with elastic or viscoelastic supports (see Fig. 2.27). These models are usually used to determine vibration response of a single or multiple vibrissae. These models are focused on mapping the functionality of control of the FSC.
- *Deformable body models.* These models consist mainly on a deformable beam, most of the time cantilevered or with elastic support, with or without pre-curvature and conicity, as natural vibrissae. They take into consideration the possible large deflections of the vibrissae (see Fig. 2.28).

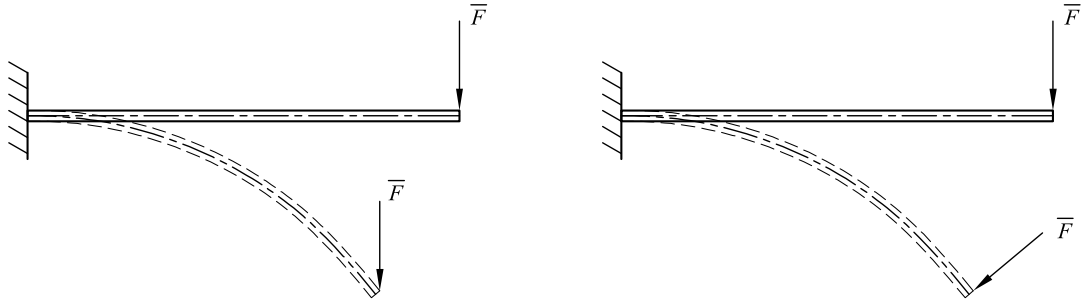


Figure 2.29: Both types of concentrated loads. Left: Direction preserving load. Right: Angle preserving load.

becomes the unity and the equation can be directly solved by integration.

$$\kappa = \frac{M}{EI} = \frac{\frac{d^2 y}{dx^2}}{\left[1 + \left(\frac{dy}{dx}\right)^2\right]^{3/2}} \quad (2.1)$$

This is the approach followed by [Fertis 2007], [Ang et al. 1993], [Chen 2010]. The advantage of this approach is that the coordinates of the points of the elastica curve (x, y) are the direct result of solving (2.1). The main disadvantage of this method is the difficulty to consider AP forces, since these models require the relative angle of the force with the beam, they require part of the solution beforehand, and this leads to an extra iterative solution. Also, in order to take into account tapered beams or complex loading, extra iterations must be performed, greatly increasing the number of iterations needed to reach a solution.

The expression (2.1) can be solved numerically after some algebraic treatment. Three methods of solving this equation are explored:

- *Power series expansion*

This procedure is based on using a power series expansion and the binomial method and the expansion and integration of the series as explained by [Ang et al. 1993], the following expression is reached:

$$y(x) = \frac{P}{2EI} \left(-\frac{x^3}{3} + lx^2\right) + \frac{1}{2} \left(\frac{P}{2EI}\right)^3 \left(-\frac{x^7}{7} + lx^6 - \frac{12}{5}l^2x^5 + 2l^3x^4\right) + \frac{3}{8} \left(\frac{P}{2EI}\right)^5 \left(-\frac{x^{11}}{11} + lx^{10} - \frac{40}{9}l^2x^9 + 10l^3x^8 - \frac{80}{7}l^4x^7 + \frac{16}{3}l^5x^6\right) + \dots + C_2 \quad (2.2)$$

This equation is a function of x , C_2 (which is zero in this case), and l which is the projected length of the beam on the x axis ($x-y$ coordinates correspond to those in Fig. 2.30), the value of l is looked for using iterations based on the bisection method.

- *Direct numerical solution*

Another possibility, explored also by [Ang et al. 1993] and then expanded by [Chen

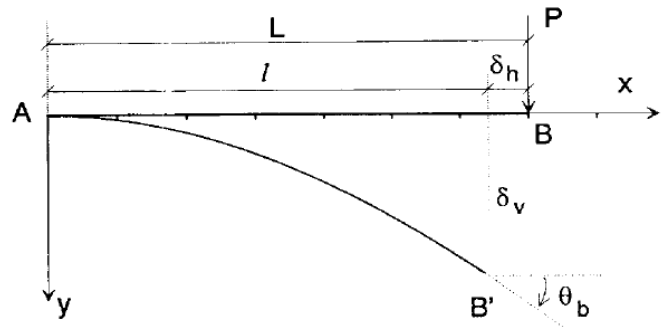


Figure 2.30: General diagram as shown by [Ang et al. 1993] of the large deflection of a cantilever beam.

2010], it is based on solving the following system of equations, that comes from (2.1)

$$\begin{cases} \frac{dz}{dx} = \frac{P(l-x)}{EI} (1+z^2)^{3/2} \\ z = \frac{dy}{dx} \\ \frac{ds}{dx} = \sqrt{1+z^2} \end{cases} \quad (2.3)$$

The system of equations (2.3) was solved also by [Ang et al. 1993]. First a initial value of l is assumed, then $s(l) = L$ is evaluated, being L the arc-length of the beam. If the condition is not satisfied, then another value of l is picked. Each guess of the solution is performed with the *Runge-Kutta approximation*, slowly decreasing the value of l from L to 0. The golden search method or the bisection method can be applied to guess a value of l .

- *Direct numerical solution 2*

This method of solution is an improvement by [Chen 2010] of the procedure done by [Ang et al. 1993], which consists on integrating the first equation in (2.3). Thus obtaining:

$$\frac{z}{\sqrt{1+z^2}} = \int_0^y \frac{M(y)}{EI} dy = G(y) \quad (2.4)$$

It holds $G(y) < 1$ by definition, if during the calculation $G(y) > 1$ is encountered, it means the projective length l is too large and a smaller value should be tested. In Fig. 2.31, the displacements of the free end are plotted, these results are the same as the ones obtained by [Bisshopp and Drucker 1945] using a different approach and solving by *Elliptic Integrals*.

Models based on the deflection angle

Another approach commonly used method consists of using the angle variation of (2.1) stated in (2.5). This procedure is more easily adapted for the AP loads (see Fig. 2.29) and also (as seen later) for the distributed loads and tapered beams. This approach can be found in the works of [Beléndez et al. 2002], [Shvartsman 2007], [Morsch et al. 2009], [Mutyalarao et al. 2010], [Shvartsman 2013].

$$\kappa = \frac{M}{EI} = \frac{d\phi}{ds} \quad (2.5)$$

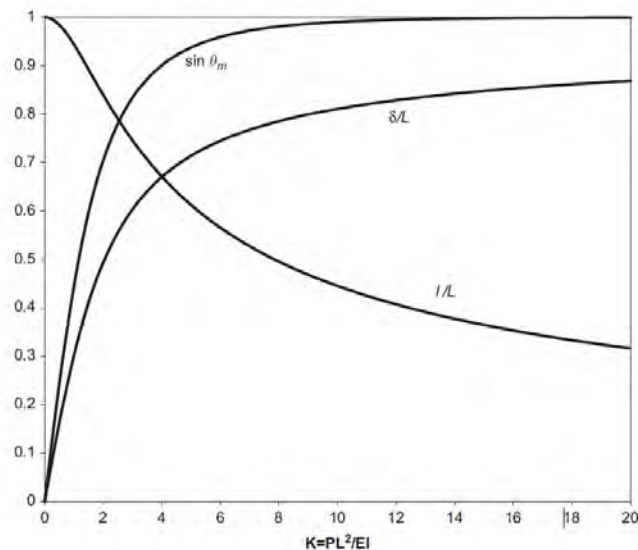


Figure 2.31: Tip displacements obtained by [Chen 2010] for a DP horizontal load at the free tip of a vertical beam.

This method has the advantage of being more flexible, since it can be used to solve problems with both direction and angle preserving tip forces. Because it calculates first the deflection angle ϕ , the bending moment is then directly determined with (2.5). A minor drawback is that the elastica coordinates must be numerically integrated afterwards through (2.6), which may induce a higher relative error.

Remark 2.1 Note that the variable ϕ and $x - y$ coordinates, in (2.5), (2.6) and (2.7) refer now to Fig. 2.32. In this calculation, the s coordinate is regarded as starting from the tip and going to the support. However, the formulation can also be done with s starting at the support and going to the tip.

$$\frac{dx}{ds} = \cos(\phi) \quad \frac{dy}{ds} = \sin(\phi) \quad (2.6)$$

This solution method consists on deriving once (2.5) in order to eliminate any term in function of the coordinates x or y of the elastica curve and replace it with (2.6).

For a cantilever beam with an AP force, as shown in Fig. 2.32, the differential equation (2.5) becomes (from [Mutyalarao et al. 2010]):

$$EI \frac{d^2\varphi}{ds^2} + P \sin(\phi + \alpha - \phi_0) = 0 \quad (2.7)$$

The main characteristic of the AP loads is the way it deflects the beam. While DP loads tend to bend the beam in one direction only, making the tip angle asymptotically get close to a specific value (see Fig. 2.31), the angle preserving load makes the beam bend in a variety of ways as displayed in Fig. 2.33.

There is mainly two methods of approximating a solution for (2.7).

- *Elliptic integral approach:* This method consists of a variable change in order to form an elliptic integral. This method of solution is used by [Ang et al. 1993], [Mutyalarao et al. 2010], [Steigenberger et al. 2015]. This method has the major drawback that the difficulty increases greatly with complex load scenarios [Chen 2010] and makes cannot be applied to tapered beams.
- *Direct numerical solution:* As the name implies, the solution is found after an iterative approach typically using the Runge-Kutta approximation. This is the most

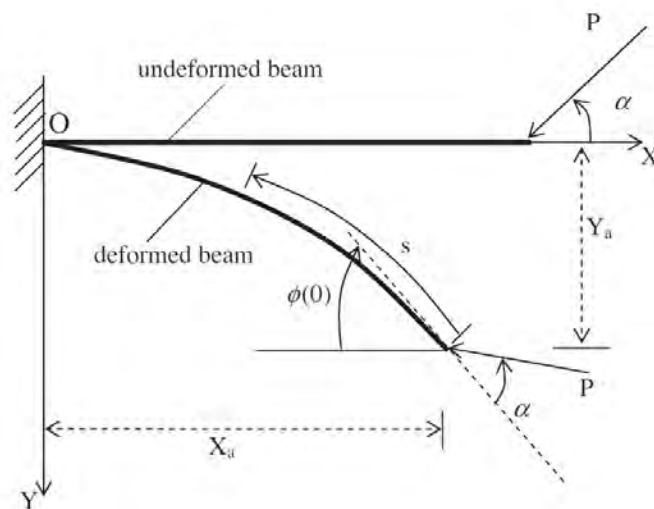


Figure 2.32: Diagram by [Mutyalarao et al. 2010] showing the deformation of a beam under an AP load.

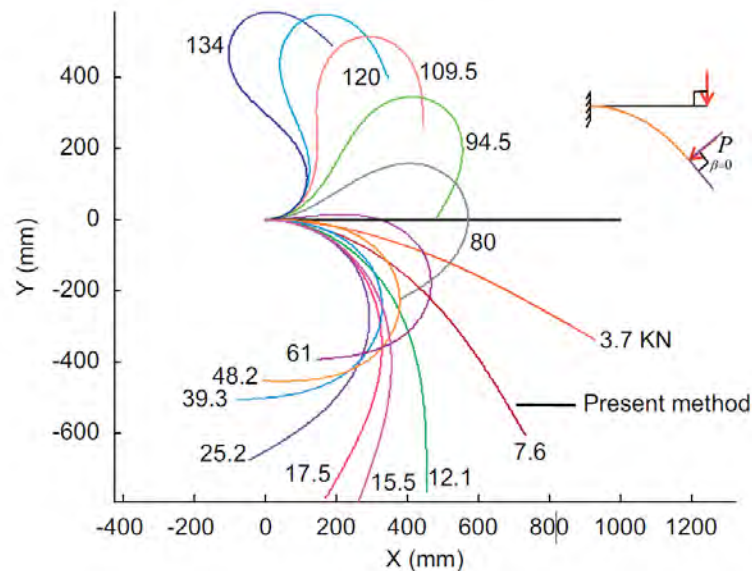


Figure 2.33: Elastica curves obtained by [Nallathambi et al. 2010] for different values of an angle preserving load.

straightforward approach, used by [Beléndez et al. 2002], [Shvartsman 2007], [Morsch et al. 2009], [Shvartsman 2013] and others in more general cases. The main advantage of this solution is the flexibility for many load scenarios, it can even be used to obtain the elastica of conical beams [Kemper 1968].

2.3.2 Models with distributed and combined loading

Modeling vibrissae with distributed loads helps to understand its response under fluid flows. In Fig. 2.24, it is shown that a modeling alternative for a fluid load is as a distributed load, it is also possible to model the FSC as torsional spring instead of a rigid support. The geometric features, such as curvature, conicity and undulations help reduce noise such as VIV [Hanke et al. 2010], [Valdivia y Alvarado et al. 2012], [Beem et al. 2012]. A model considering all these features could not be found in the surveyed literature. Only models

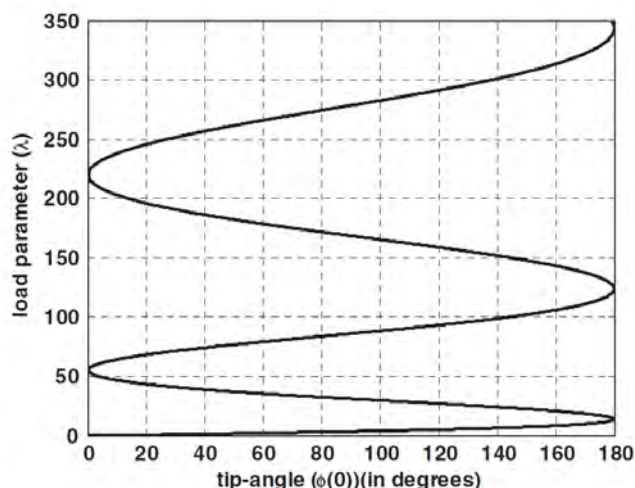


Figure 2.34: Results obtained by [Mutyalarao et al. 2010] of the tip angle as a function of the load parameter for an angle preserving load. Notice how the tip angle oscillates in function of the force parameter.

of distributed loads with uniform and rigidly supported beams could be found. However, these models help to gain insight in the methods to solve more complex problems. Methods of solution depending on the radius of curvature and on elliptic integrals typically fall short due to the disadvantages explained before. The main difficulty in this case is integrating the integral bending moment term. An alternative to calculating this term is considering that the beam suffers only small deflections.

Approximation of the bending moment term - small deflections

This approximation of the bending moment function is performed by [Koo Lee et al. 1993] and [Chen 2010], as seen in Fig. 2.35. It possesses an error in the calculation of the real applied load on the beam, due to the consideration of the load as if the deflections were small. The bigger the force applied, the greater the relative error will be in comparison to other studies, [Koo Lee et al. 1993] obtained a 4.4% relative error when comparing this approximation with previous authors. The relative error obtained in this studies is usually less than 1%.

Integral form of the bending moment

This approach takes the integral expression of the bending moment into account:

$$M = \int_s^L w_0[x(\xi) - x(s)]ds \quad (2.8)$$

This approach is taken from [Kimiaefar et al. 2014], [Rao and Rao 1989] and [Lee 2002]. Solution of the differential equation is performed typically with the Runge-Kutta Method with an initial approximation, and the solution reached typically with the bisection method.

A special case is the approximation by [Rao and Rao 1989] that considers that the distributed load is also an AP load (see Fig. 2.36), this consideration greatly increases the difficulty of the problem by casting an integro-differential fourth order non-linear two point BVP.

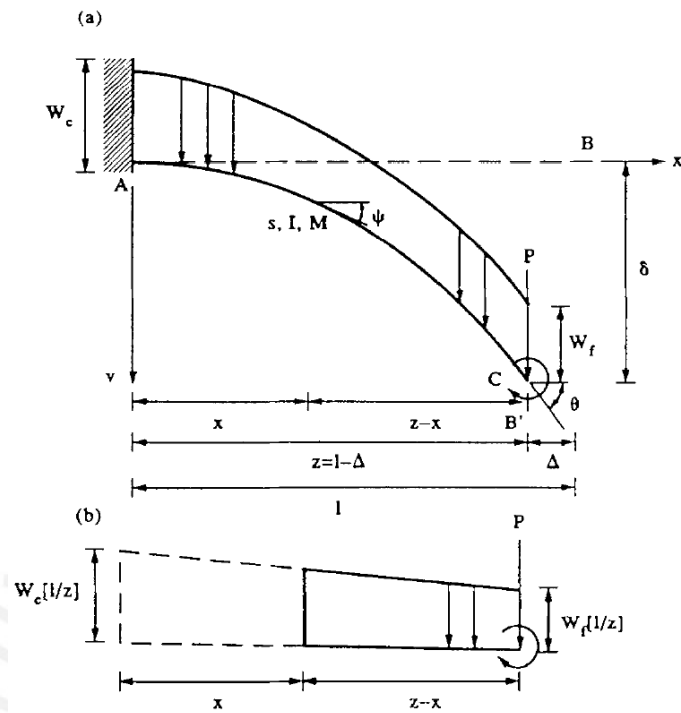


Figure 2.35: Approximation of the distributed load as the distributed load on a small-deflection beam by [Koo Lee et al. 1993].

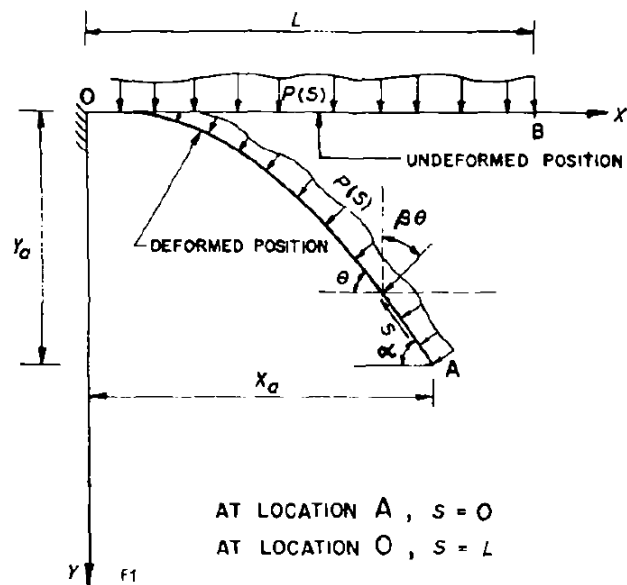


Figure 2.36: Angle preserving distributed load model by [Rao and Rao 1989]

2.4 Numerical procedures

2.4.1 Runge-Kutta Methods (RK)

The RK methods, named after Carl Runge and Wilhelm Kutta, are widely used methods to solve ordinary differential equations (ODE) with initial values, known as initial-value problems (IVP). The most common and widely used of these methods is the fourth order Runge-Kutta method (RK4) which is accurate, stable and easy to implement [Mathews and Fink 1999]. The main advantage of the RK methods, over others such as the Taylor method, is that they do not need to calculate the derivatives of the function f at each point [Chapra and Canale 2010], but determine the value of the solution at each point through a series of continuous calculations.

General procedure

In general, RK methods are all general forms of the Euler method [Zill and Cullen 2008], [O'Neil 2011], to solve first-order IVP, which in general can be stated as (2.9):

$$\begin{cases} \frac{dy}{dt} = f(t, y) \\ y(t_0) = y_0 \end{cases} \quad (2.9)$$

The solution is obtained by replacing f by a weighted average of m terms:

$$y_{n+1} = y_n + h(w_1k_1 + w_2k_2 + \dots + w_mk_m) \quad (2.10)$$

The number m defines the order of the RK method. The general condition is that the weight constants w satisfy the condition: $w_1 + w_2 + \dots + w_m = 1$. The terms k_i are defined recursively, they depend on the previous values. If for example $m = 1$, then $k_1 = f(x_n, y_n)$ and (2.10) becomes $y_{n+1} = y_n + hf(x_n, y_n)$, which is the Euler Method [Zill and Cullen 2008].

For higher order methods, (2.10) must be compared with a Taylor series and force the equivalence between the two equations to produce a system of equations to determine w and k . For instance, for the second order method or RK2, two k terms are defined:

$$\begin{cases} y_{n+1} = y_n + h(w_1k_1 + w_2k_2) \\ k_1 = f(t_n, y_n) \\ k_2 = f(t_n + \alpha h, y_n + \beta hk_1) \end{cases} \quad (2.11)$$

After the match-up with a Taylor series, the following system of equations is obtained:

$$w_1 = 1 - w_2, \quad \alpha := \frac{1}{2w_2}, \quad \beta := \frac{1}{w_2} \quad (2.12)$$

which has four unknowns and three equations, thus an infinite set of solutions. The most common solution for RK2 consists on $w_2 = 1/2$ which yields $w_1 = 1/2$, $\alpha = 1$ and $\beta = 1$.

Fourth order Runge Kutta

The derivation of the RK4 and higher methods is equivalent to the RK2 derivation [Cheney and Kincaid 2008] and is out of the scope of this work. The procedure gives the following equations:

$$\begin{cases} y_{n+1} = y_n + h(w_1k_1 + w_2k_2 + w_3k_3 + w_4k_4) \\ k_1 = f(t_n, y_n) \\ k_2 = f(t_n + \alpha_1h, y_n + \beta_1hk_1) \\ k_3 = f(t_n + \alpha_2h, y_n + \beta_2hk_1 + \beta_3hk_2) \\ k_4 = f(t_n + \alpha_3h, y_n + \beta_4hk_1 + \beta_5hk_2 + \beta_6hk_3) \end{cases} \quad (2.13)$$

The derivation ends up to determine 13 parameters from 11 equations. Just as in the RK2 case, there is an infinite set of solutions, the most common combination gives [Zill and Cullen 2008]:

$$y_{n+1} = y_n + \frac{h}{6}(f_1 + 2f_2 + 2f_3 + f_4) \quad (2.14)$$

$$\begin{cases} k_1 = f(t_n, y_n) \\ k_2 = f\left(t_n + \frac{h}{2}, y_n + \frac{h}{2}k_1\right) \\ k_3 = f\left(t_n + \frac{h}{2}, y_n + \frac{h}{2}k_2\right) \\ k_4 = f(t_n + h, y_n + hk_3) \end{cases} \quad (2.15)$$

If higher accuracy is needed, instead of using higher order RK methods, it is enough to use the RK4 method with a smaller step size h [Mathews and Fink 1999].

Fourth order RK4 for higher order differential equations

A similar procedure as stated before to derive the RK2 and RK4 methods can be used to solve higher order differential equations as a system of first order differential equations [Mathews and Fink 1999], [Cheney and Kincaid 2008], [Zill and Cullen 2008]. For instance, the second order differential equation:

$$\begin{cases} y'' = f(t, y, y') \\ y(t_0) = y_0, \quad y'(t_0) = u_0 \end{cases} \quad (2.16)$$

can be converted into: the following system:

$$\begin{cases} y' = u \\ u' = f(t, y, u) \\ y(t_0) = y_0, \quad u(t_0) = u_0 \end{cases} \quad (2.17)$$

The solution has the same combination as the RK4 method for first order differential equations [Zill and Cullen 2008]:

$$\begin{aligned} y_{n+1} &= y_n + \frac{h}{6}(m_1 + 2m_2 + 2m_3 + m_4) \\ u_{n+1} &= u_n + \frac{h}{6}(k_1 + 2k_2 + 2k_3 + k_4) \end{aligned} \quad (2.18)$$

where:

$$\begin{cases} m_1 = u_n & k_1 = f(x_n, y_n, u_n) \\ m_2 = u_n + \frac{1}{2}hk_1 & k_2 = f\left(x_n + \frac{1}{2}h, y_n + \frac{1}{2}hm_1, u_n + \frac{1}{2}hk_1\right) \\ m_3 = u_n + \frac{1}{2}hk_2 & k_3 = f\left(x_n + \frac{1}{2}h, y_n + \frac{1}{2}hm_2, u_n + \frac{1}{2}hk_2\right) \\ m_4 = u_n + hk_3 & k_4 = f(x_n + h, y_n + hm_3, u_n + hk_3) \end{cases} \quad (2.19)$$

2.4.2 Non-linear finite difference method

Typically, the differential equation of an elastica is given by a second order differential equation with known values at certain points (supports), these kind of problems are BVP. The most common of these problems are two point BVP, in which the known values are usually located at both ends of the interval of the independent variable. The most common methods to approximate the solution are the *shooting method* and the *finite difference method* (FDM). The FDM is usually more stable but requires more computation [Burden and Faires 2011]. However, this method has a drawback when comparing it with other possible solving methods, like the RK4; and it lies on the truncation error, since the RK4 truncation error is in the order of $O(h^4)$ and the FDM is in the order of $O(h^2)$.

The following procedure is based on [Burden and Faires 2011] and [Ascher et al. 1995].

General procedure

The general, non-linear, explicit, two-point BVP:

$$y'' = f(x, y, y'), \quad a < x < b, \quad y(a) = \alpha, \quad y(b) = \beta \quad (2.20)$$

The following procedure is similar to the one applied to linear problems, with the difference that the set of equations is non-linear. In order to solve the non-linear problem, the *Newton-Raphson Method* is applied, any other iterative method can also be used.

After ensuring the existence of the solution (for details see [Burden and Faires 2011]), the domain or the arc length of the vibrissa is divided into $N + 1$ subintervals of the same size, with the endpoints $x_i = a + ih$ with $i = 0, 1, 2, \dots, N + 1$, that gives a step size $h := \frac{b-a}{N}$ (note that dividing the arc length into subintervals of variable size is also possible). Now, Eq. (2.20) takes the discrete form:

$$y_i'' = f(x_i, y_i, y_i') \quad (2.21)$$

by using the *central difference*, the first and second derivative can be approximated [Pal 2007], as follows:

$$y_i' = \frac{y(x_{i+1}) - y(x_{i-1}))}{2h} \quad (2.22)$$

$$y_i'' = \frac{y(x_{i+2}) - 2y(x_i) + y(x_{i-2}))}{h^2} \quad (2.23)$$

inserting (2.22) and (2.23) into (2.21) and ignoring the truncation error term (higher order terms in a Taylor series):

$$\frac{y(x_{i+1}) - 2y(x_i) + y(x_{i-1}))}{h^2} = f\left(x_i, y(x_i), \frac{y(x_{i+1}) - y(x_{i-1}))}{2h}\right) + O(h^2) \quad (2.24)$$

Ignoring the truncation error term is possible by choosing a small step size h , since the truncation error increases along large step sizes [Iott et al. 1985]. Each point of the solution $y(x_i)$ can be approximated with $y(x_i) = w_i$, and boundary conditions, which correspond to $i = 0$ and $i = N + 1$ become:

$$w_0 := \alpha, \quad w_{N+1} := \beta$$

and the general form

$$-\frac{w_{i+1} - 2w_i + w_{i-1}}{h^2} + f\left(x_i, w_i, \frac{w_{i+1} - w_{i-1}}{2h}\right) = 0 \quad (2.25)$$

for the remaining $i = 1, 2, \dots, N$.

Equation (2.25) can be written for each $i = 1, \dots, N$, as a set of $N \times N$ non-linear system of equations:

$$\begin{aligned}
 2w_1 - w_2 + h^2 f\left(x_1, w_1, \frac{w_2 - \alpha}{2h}\right) - \alpha &= 0, \\
 -w_1 + 2w_2 - w_3 + h^2 f\left(x_2, w_2, \frac{w_3 - w_1}{2h}\right) &= 0, \\
 -w_2 + 2w_3 - w_4 + h^2 f\left(x_3, w_3, \frac{w_4 - w_2}{2h}\right) &= 0, \\
 &\vdots \\
 -w_{N-1} + 2w_N + h^2 f\left(x_N, w_N, \frac{\beta - w_{N-1}}{2h}\right) - \beta &= 0
 \end{aligned} \tag{2.26}$$

Newton-Raphson Method

In order to approximate (w_1, w_2, \dots, w_N) from (2.26), a sequence of iterations must be performed (since it is a non-linear problem). The initial set of points $(w_1^{(0)}, w_2^{(0)}, \dots, w_N^{(0)})$ close to the solution has to be defined, e.g. a linear distribution between α and β . The iteration process is represented by the equation:

$$w^{(k)} = w^{(k-1)} - J(w^{(k-1)})^{-1} F(w^{(k-1)}) \tag{2.27}$$

where:

- $w^{(k)}$: current approximation of the solution.
- $w^{(k-1)}$: previous approximation of the solution.
- $F(w^{(k-1)})$: system of equations, in this case (2.26)
- $J(w^{(k-1)})$: jacobian of F

Calculation of the Jacobian J of (2.26) gives a tridiagonal matrix, defined by (note that $j = 1, 2, \dots, N$):

$$J(w_1, \dots, w_N)_{ij} = \begin{cases} -1 + h/2 f_{,y'}\left(x_i, w_i, \frac{w_{i+1} - w_{i-1}}{2h}\right), & \text{for } i = j - 1, j = 2, \dots, N; \\ 2 + h^2 f_{,y}\left(x_i, w_i, \frac{w_{i+1} - w_{i-1}}{2h}\right), & \text{for } i = j, j = 1, \dots, N; \\ -1 - \frac{h}{2} f_{,y'}\left(x_i, w_i, \frac{w_{i+1} - w_{i-1}}{2h}\right), & \text{for } i = j + 1, j = 1, \dots, N - 1 \end{cases} \tag{2.28}$$

also with $w_0 = \alpha$ and $w_{N+1} = \beta$.

By altering the order of (2.27) and introducing the variable $v^{(k)} = w^{(k)} - w^{(k-1)}$:

$$\begin{aligned}
 J(w_1, \dots, w_N)_{ij}(v_1, \dots, v_n)^T &= F^T \\
 &= - \left(2w_1 - w_2 - \alpha + h^2 f \left(x_1, w_1, \frac{w_2 - \alpha}{2h} \right), \right. \\
 &\quad - w_1 + 2w_2 - w_3 + h^2 f \left(x_2, w_2, \frac{w_3 - w_1}{2h} \right), \dots, \\
 &\quad - w_{N-2} + 2w_{N-1} - w_N + h^2 f \left(x_3, w_3, \frac{w_N - w_{N-2}}{2h} \right), \\
 &\quad \left. - w_{N-1} + 2w_N - \beta + h^2 f \left(x_N, w_N, \frac{\beta - w_{N-1}}{2h} \right) \right)^T
 \end{aligned} \tag{2.29}$$

Equation (2.29) is actually a tridiagonal system of linear equations, with the vector v of unknowns. In order to solve for w , the first approximation $w^{(0)}$ is assumed as a straight line from α to β . Equations (2.26) and (2.28) are evaluated with $w^{(0)}$. With both J and F , the tridiagonal system in (2.29) is solved and $v^{(1)}$ is obtained, $w^{(1)}$ is determined with $w^{(k)} = v^{(k)} + w^{(k-1)}$. The process is then repeated, until $v^{(k)}$ or the difference between w^k and w^{k-1} is small enough to be ignored.

2.4.3 Bisection Method

The bisection method is a root-finding algorithm for problems of the form $f(x) = 0$. This method is based on the intermediate value theorem that states: For a continuous function $f(x)$ defined on the interval $[a, b]$, if $f(a)$ and $f(b)$ have opposite signs then there must be a value p such that $f(p) = 0$. The procedure can be easily described in the following conditions (from [Burden and Faires 2011]):

- To begin, the mid value c of the interval $[a, b]$ must be set as:

$$c := \frac{a + b}{2}$$

- If $f(c) = 0$, then $p = c$, and the program ends.
- If $f(c) \neq 0$, then $f(c)$ must have the same sign as $f(a)$ or $f(b)$.
 - If $f(c)$ and $f(a)$ have the same sign, then $p \in (c, b)$. Set $a := c$, $b := b$ and start again.
 - If $f(c)$ and $f(b)$ have opposite signs, then $p \in (a, c)$. Set $a := a$, $b := c$ and start again.

Figure 2.37 shows that if the intermediate value theorem is fulfilled, there must be at least one solution. The value of c can be regarded as solution if the difference between a and b is small enough to be ignored [Cheney and Kincaid 2008].

2.5 Concretization of thesis goals

The reviewed literature suggests that even though research has been performed on sensing flows with tactile sensors, there is still investigations to be performed on the mechanical response of the vibrissa itself and its response to high loading. The present work contributes to this field of research by investigating the mechanical behavior of the vibrissa

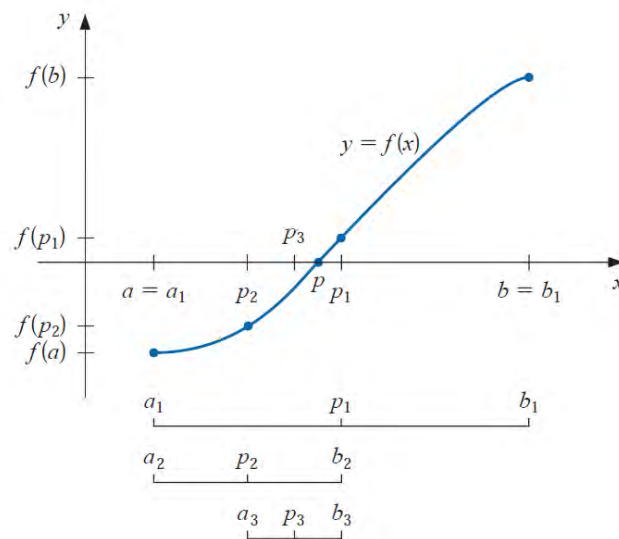


Figure 2.37: Graphic representation of the bisection method. Source: [Burden and Faires 2011].

and the influence of different parameters on such behavior.

As stated by [Hartmann 2015], a vibrissa can be modeled as a cantilever beam, the follicles can be modeled as a elastic supports which consist of springs at the base [Valdivia y Alvarado et al. 2012]. This indicates that the models of large deflection of cantilever beams, such as the ones explored in Section 2.3, can be used to study the vibrissa behavior. Vibrissa geometric characteristics include different lengths, conicity, and an inherent curvature. Thus, the mechanical-mathematical model to develop must include these features. There is also a need to compare the results obtained to those found in literature; however the different geometries make a direct comparison rather difficult.

As stated before, there is no special focus on certain vibrissa type. The results must be independent from geometry, material properties, applied load magnitude, and rigidity of support. In order to take these into consideration, dimensionless results are sought. Thus the Euler-Bernoulli equation must be casted into a dimensionless form that depends on dimensionless parameters describing the various features of a vibrissa.

In summary, the goals of the present work are:

- Build a mechanical-mathematical model of a general vibrissa under fluid loads, as a cantilever beam which is subjected to large deflections, with the Euler-Bernoulli beam theory. Important remark: there is no focus in a specific type of vibrissa.
- Cast the Euler-Bernoulli equations into a dimensionless form, that depends on four dimensionless parameters that describe: force, geometry, and material properties; conicity; pre-curvature; and rigidity of support.
- Implement numerical approximations of the solution of the Euler-Bernoulli equations, which are in general: non-linear, non-autonomous, mixed boundary, ODEs.
- Analyze the influence of the variation of each dimensionless parameter.
- Set up basis for the further development of flow detection with tactile sensors.

Chapter 3

Formulation of the mechanical-mathematical problem

3.1 General model

A general model for a cantilever beam representing a vibrissa with different considerations is set up to investigate the influence of various parameters concerning the geometry and the support of the vibrissae with respect to the bending behavior and further use for object and fluid detection.

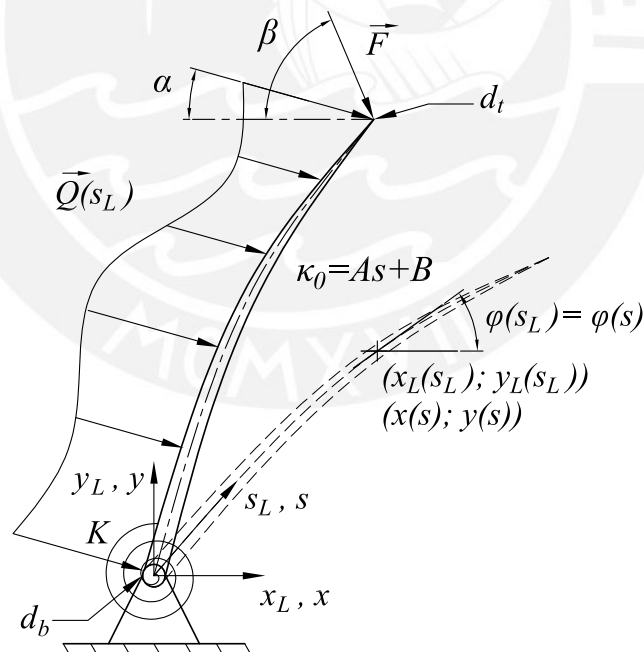


Figure 3.1: General vibrissa with all considerations

Remark 3.1 (Notation) The subindex L corresponds to length parameters with dimensions and parameters without the subindex represent their dimensionless counterparts. For instance s_L and s . See Section 3.2.5 for details.

The parameters shown Fig. 3.1 are listed below:

- s_L : arc length of the vibrissa.

- x_L and y_L : coordinates of each point of the neutral axis of the elastica curve.
- φ : deflection angle measured from x -axis to y -axis.
- d_b and d_t : diameter of the vibrissa at the base and tip respectively.
- I_b : moment of inertia at the base, depends on d_b .
- L : arc length of the vibrissa.
- κ_{0L} : pre-curvature function of the vibrissae
- K : stiffness of the torsional spring at the base of the vibrissa.
- \vec{F} : concentrated load. It represents a contact load on the shaft of the vibrissa.
- \vec{Q} : distributed load over the length. It represents the load of a fluid flow over the surface of the vibrissa. It depends on the diameter of the cross section, the flow velocity and its density and viscosity. When both \vec{F} and \vec{Q} are present, the model can represent surface detection under the influence of a fluid load.
- E : modulus of elasticity or Young's modulus of the material.

As seen in Fig. 3.1, the general model considers a variety of loads, pre-curvature, conicity and elastic support at the base. However, the model displayed is too broad to analyze at a single time, the influence of each change in parameter must be accounted for and in order to compare the different solutions and further apply them into real problems, it must be transformed into a dimensionless form.

3.2 Deduction of the equation of the system

3.2.1 Geometry of the vibrissa

In order to consider the geometry features of vibrissae, two parameters are introduced:

Conicity

The conicity of the vibrissa, which directly influences the moment of inertia, has to be taken into consideration. From the geometry of an extended vibrissa (see Fig. 3.2) the diameter of the cross section at any position s_L is deduced as:

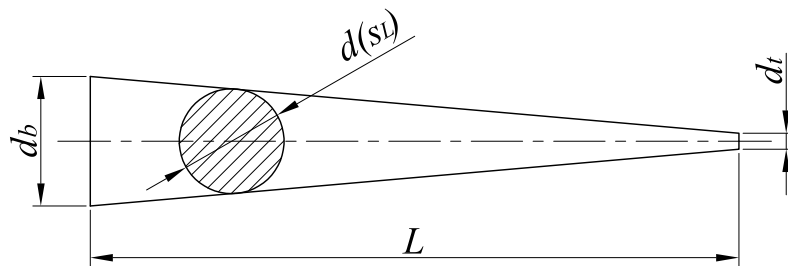


Figure 3.2: Cone geometry for a straight vibrissa.

$$d(s_L) := d_b - \frac{d_b - d_t}{L} s_L \quad (3.1)$$

A parameter to describe the conicity of the beam is defined as the ratio of the tip and base diameter:

$$\vartheta := \frac{d_t}{d_b} \quad \left[\frac{m}{m} \right] \quad (3.2)$$

By mixing (3.2) and (3.1), the diameter at any point is obtained in function of the base diameter and the diameter ratio:

$$d(s_L) = d_b \left(1 - \frac{1 - \vartheta}{L} s_L \right) \quad (3.3)$$

By using (3.3), the moment of inertia of the cross section at any s can be determined in function of the base moment of inertia I_b and the diameter ratio ϑ :

$$I(s_L) = I_b \left(1 - \frac{1 - \vartheta}{L} s_L \right)^4 \quad (3.4)$$

Note that since this is a 2D analysis, $I(s_L) = I_z(s_L)$.

Remark 3.2 (Definition of the conicity parameters) *Note that other authors define the conicity parameters in a different matter, such as [Kemper 1968] and [Scharff et al. 2016]. However, they represent the same model and yield same results with only difference in the representation.*

Pre-curvature

The pre-curvature is also a major characteristic in vibrissae. As explained before in Section 2.1.2, it can be described either by a polynomial function (e.g. quadratic or parabolic function) in cartesian coordinates or using intrinsic coordinates in the form of a Cesáro function, that describes the pre-curvature κ_{0L} as a function of the arc length s_L . A close approximation, according to [Towal et al. 2011], consists on a linear Cesáro function (3.5). Note that a linear Cesáro equation provides a large number of “shapes” for the pre-curvature as shown in Fig. 2.9. More complex and detailed scenarios are possible with a higher-order polynomial Cesáro function or with non-linear Cesáro functions (examples of such functions can be found on [Yates 1952], [Lawrence 1972] and [Weisstein 2016]). However, since there is no special focus on a specific type of vibrissae, and using higher-order polynomial functions has not been found on the surveyed literature, a linear Cesáro equation is used.

$$\kappa_{0L}(s_L) = A_L s_L + B_L \quad (3.5)$$

Special cases are defined as follows:

- If $A = 0$ and $B \neq 0$, then the pre-curvature is constant along the arc length, which corresponds to a circular curve.
- If $A \neq 0$ and $B = 0$, the the pre-curvature describes an Euler’s spiral [Lawrence 1972].

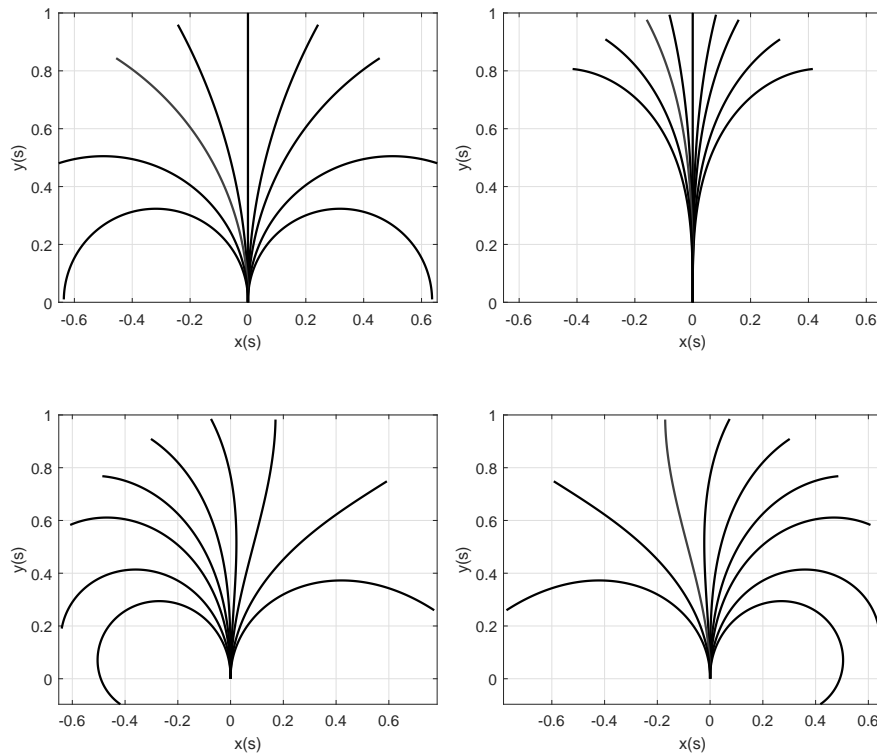


Figure 3.3: Various pre-curved vibrissae with varying values of A and B . Top left: $A = 0$ for all and $B \in \{-\pi, -2, -1, -0.5, 0, 0.5, 1, 2, \pi\}$. Top right: $B = 0$ for all and $A \in \{-3, -2, -1, -0.5, 0, 0.5, 1, 2, 3\}$. Bottom left: $A = 0$ for all and $B \in \{-\pi, -2, -1, -0.5, 0, 0.5, 1, 2, \pi\}$. Bottom right: $A = -2$ and $B \in \{-\pi, -2, -1, -0.5, 0, 0.5, 1, 2, \pi\}$.

3.2.2 Geometry of the elastica curve

The elastica curve can be described using Cartesian coordinates, which are related to the deflection angle φ and the x and y coordinates using a system of differential equations:

$$\left. \begin{aligned} x'_L &= \frac{dx_L}{ds_L} = \cos \varphi \\ y'_L &= \frac{dy_L}{ds_L} = \sin \varphi \\ \varphi' &= \frac{d\varphi}{ds_L} = \kappa(s_L) \end{aligned} \right\} \quad (3.6)$$

The term $\kappa(s_L)$ is known as curvature and provides the relationship between the geometry and loading: the constitutive load, which is shown in (3.7):

$$\kappa_{0L} = \frac{M_z(s_L)}{EI(s_L)} \quad (3.7)$$

3.2.3 Euler-Bernoulli equation

According to the Euler-Bernoulli theory [Fertis 2007], [Gere and Goodno 2008], [Hibbeler 2011], [Beer et al. 2012], the deflection angle and curvature radius can be related with the

geometric expression:

$$\rho_L d\varphi = ds_L \quad (3.8)$$

Furthermore, for a linear elastic material, the curvature can be related to the internal bending moment M_z , the material properties E and the cross section I as follows:

$$\kappa_L = \frac{1}{\rho_L} = \frac{d\varphi}{ds_L} \quad (3.9)$$

then, using the constitutive law (3.7):

$$\frac{d\varphi}{ds_L} = \frac{M_z(s_L)}{EI(s_L)} \quad (3.10)$$

Note that M_z depends on the external loads (F and Q) and the cross section moment of inertia depends on ϑ (recall (3.4)).

3.2.4 Analysis of the cross-section

The method of sections is used to determine the internal cross section of the beam model in Fig. 3.1, the cross section analysis can be seen in Fig. 3.4.

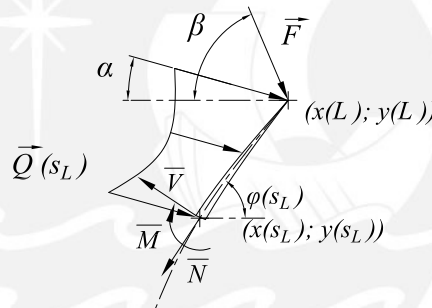


Figure 3.4: Section analysis of the beam, showing the internal loads acting on the section.

Based on Fig. 3.4, the internal bending moment can be defined using the moment equilibrium equation:

$$\begin{aligned} M_z(s_L) = & -F[\cos(\beta)(y_L(L) - y_L(s_L)) + \sin(\beta)(x_L(L) - x_L(s_L))] \\ & - \int_{s_L}^L Q(\xi)[\cos(\alpha)(y_L(\xi) - y_L(s_L)) + \sin(\alpha)(x_L(\xi) - x_L(s_L))]d\xi \end{aligned} \quad (3.11)$$

note that ξ is an integration variable.

Remark 3.3 (Consideration for the distributed load) *For the sake of simplicity, the distributed load is considered as a uniformly distributed force: $Q(s) = Q$. The actual distribution of the load would have to be determined from experiments or numerical simulations on fluids, for various Reynold numbers, which is out of the scope of this thesis.*

Remark 3.4 (Application of the concentrated force and further notation) *In general terms, the concentrated load can be applied in any point of the vibrissa shaft. Thus, turning the bending moment equation into a piecewise equation. However, further calculations in the next chapters do not require this general case, as the main focus lies in*

the segment between the support and the point of application of the concentrated load. This segment can be modeled as shown in Fig. 3.1, and the remaining segment can be modeled as undeformed. From now on, the subindex 1 is used to refer to the application point, which corresponds to the tip of the vibrissa.

Plugging (3.11) and (3.4) into (3.10), the system of equations for the model becomes:

$$\left. \begin{aligned} x'_L(s_L) &= \cos \varphi(s) \\ y'_L(s_L) &= \sin \varphi(s) \\ \varphi'(s_L) &= - \frac{F[\cos(\beta)(y_L(s_{1L}) - y_L(s_L)) + \sin(\beta)(x_L(s_{1L}) - x_L(s_L))] + Q \int_{s_L}^{s_{1L}} \cos(\alpha)(y_L(\xi) - y_L(s_L)) + \sin(\alpha)(x_L(\xi) - x_L(s_L))d\xi}{EI_b(1 + (\vartheta - 1)s_L/L)^4} + As_L + B \end{aligned} \right\} \quad (3.12)$$

3.2.5 Definition of dimensionless parameters

To further analyze the problem, the following dimensionless parameters are introduced.

Geometric dimensionless parameters

The dimensionless coordinates are defined with the help of the dimensional coordinate and the length of the vibrissa:

- dimensionless arc-length s :

$$s := \frac{s_L}{L} \left[\frac{m}{m} \right] \quad (3.13)$$

- dimensionless x -coordinate:

$$x := \frac{x_L}{L} \left[\frac{m}{m} \right] \quad (3.14)$$

- dimensionless y -coordinate:

$$y := \frac{y_L}{L} \left[\frac{m}{m} \right] \quad (3.15)$$

Load dimensionless parameters

All loads applied to the vibrissae must also be transformed into a dimensionless form for further use. The transformation is done using load parameters, which are a function of the arc-length of the vibrissa L , cross section at the base I_b , and material properties E :

- for a concentrated load F , the force parameter is obtained by dividing the dimensional force magnitude F by the dimensional factor f_0 :

$$F = f \cdot f_0 = f \frac{EI_b}{L^2} \rightarrow f = \frac{F}{f_0} \quad (3.16)$$

$$f := \frac{FL^2}{EI_b} \left[\frac{N \cdot m^2}{Nm^{-2} \cdot m^4} \right] \quad (3.17)$$

- for a distributed load q , a similar procedure is followed, obtaining:

$$q := \frac{QL^3}{EI_b} \left[\frac{Nm^{-1} \cdot m^3}{Nm^{-2} \cdot m^4} \right] \quad (3.18)$$

- for the stiffness of the torsional spring k_t , yet a similar procedure is followed:

$$k := \frac{KL}{EI_b} \left[\frac{Nm \cdot m}{Nm^{-2} \cdot m^4} \right] \quad (3.19)$$

3.2.6 Dimensionless form of the system equation

The next step of the analysis is to transform the dimensional equations (3.6) and (3.12) into a dimensionless form, so they do not depend on a specific geometry, material or load. This transformation is done with the help from the dimensionless parameters mentioned above, see (3.13), (3.14), (3.15), (3.17), (3.18) and (3.19).

$$\left. \begin{aligned} x'(s) &= \cos(\varphi(s)) \\ y'(s) &= \sin(\varphi(s)) \\ \varphi'(s) &= \frac{-f(y(s_1) - y(s)) \cos(\beta) - f(x(s_1) - x(s)) \sin(\beta)}{(1 + (\vartheta - 1)s)^4} \\ &\quad - \frac{q \int_s^{s_1} [(y(\xi) - y(s)) \cos(\alpha) + (x(\xi) - x(s)) \sin(\alpha)] d\xi}{(1 + (\vartheta - 1)s)^4} + As + B \end{aligned} \right\} \quad (3.20)$$

boundary conditions for the elastic support:

$$\varphi(0) = \varphi_0, \quad \frac{d\varphi(1)}{ds} = A + B, \quad x(0) = 0, \quad y(0) = 0 \quad (3.21)$$

The moment provided by the torsional spring at the base and the internal bending moment at the base must be equal to guarantee equilibrium:

$$m(0) + k \left(\frac{\pi}{2} - \varphi_0 \right) = 0 \quad (3.22)$$

Note that for a rigid support the base deflection angle $\varphi_0 = \pi/2$, and the condition of the elastic support is not needed.

In order to approximate a solution for (3.20), terms depending of the tip coordinates (x_1, y_1) and the integral part of the distributed load moment have to be eliminated or transformed into another form, since they require an a-priori solution. This can be achieved by deriving once the last equation in (3.20). Note that $\frac{d^2\varphi}{ds^2} = \kappa'$:

$$\begin{aligned} \kappa' &= \frac{-f[-\sin(\varphi) \cos(\beta) - \cos(\varphi) \sin(\beta)] - q(s_1 - s)[- \sin(\varphi) \cos(\alpha) - \cos(\varphi) \sin(\alpha)]}{(1 + (\vartheta - 1)s)^4} \\ &\quad - \frac{4(\vartheta - 1)}{(1 + (\vartheta - 1)s)^5} \left[-f(y(s_1) - y(s)) \cos(\beta) - f(x(s_1) - x(s)) \sin(\beta) \right. \\ &\quad \left. - q \int_s^{s_1} [(y(\xi) - y(s)) \cos(\alpha) + (x(\xi) - x(s)) \sin(\alpha)] d\xi \right] + A \end{aligned} \quad (3.23)$$

Even though (3.23) appears to be more difficult to solve, it can be simplified by arranging the second term into a similar form of (3.20), similarly as the procedure found in [Kemper 1968].

$$\begin{aligned} \kappa' &= \frac{-f(-\sin(\varphi) \cos(\beta) - \cos(\varphi) \sin(\beta)) - q(1 - s)[- \sin(\varphi) \cos(\alpha) - \cos(\varphi) \sin(\alpha)]}{(1 + (\vartheta - 1)s)^4} \\ &\quad - \frac{4(\vartheta - 1)}{(1 + (\vartheta - 1)s)} [\varphi' - As - B] + A \end{aligned} \quad (3.24)$$

It can be further compressed by applying the trigonometric identity of the sine of the sum of two angles. Thus, the system is transformed into four differential equations: ¹

¹Trigonometric identity: $\sin(a \pm b) = \sin a \cos b \pm \cos a \sin b$

System equation

$$\left. \begin{aligned} x' &= \cos \varphi \\ y' &= \sin \varphi \\ \varphi' &= \kappa \\ \kappa' &= \frac{f \sin(\varphi + \beta) + q(1 - s) \sin(\varphi + \alpha)}{(1 + (\vartheta - 1)s)^4} - \frac{4(\vartheta - 1)}{(1 + (\vartheta - 1)s)} [\varphi' - As - B] + A \end{aligned} \right\} \quad (3.25)$$

with the same boundary conditions shown in (3.21) and (3.22) for the elastic support case.

3.2.7 Main set of parameters for investigations

Equation (3.25) represents the elastica and deformation of the model in Fig. 3.1 and can be used for different load scenarios and geometries. The influence of the following main parameters is analyzed and studied in the following chapters:

- f : dimensionless tip concentrated load with an inclination β . Only a single load is at a time is applied to the system. The influence of its magnitude and direction is analyzed and two kinds of force are investigated: DP and AP loads.
- q : dimensionless distributed load with an inclination α . Only a constant fluid flow load is applied at a time to the system. Again, the influence of its magnitude and direction is analyzed. A difference between solution methods using the FDM and RK4 approach is also studied.
- ϑ : conicity parameter. The influence of the variation of the conicity in a range of $0 < \vartheta \leq 1$ is analyzed. Note that $\vartheta = 1$ describes a cylindrical beam.
- A and B : pre-curvature Cesáro variables. Different combinations of these parameters and their influence are studied. Note that for a beam without pre-curvature $A, B = 0$.
- k : dimensionless torsional stiffness of the elastic support. The influence of the variation of the torsional stiffness on the general stiffness of the system is studied.

In summary, the following set of parameters describe the vibrissa type:

$$\boxed{f \text{ and } \beta, \quad q \text{ and } \alpha, \quad \vartheta, \quad A \text{ and } B, \quad k} \quad (3.26)$$

Solution using FDM In order to approximate a solution using the FDM, the derivatives of (3.25) are needed for the Jacobian, according to the method explained in Section 2.4.2. Note that $\varphi' = d\varphi/ds$.

$$\begin{aligned} \frac{dF}{d\varphi} &= \frac{f \cos(\varphi + \beta) + q(1 - s) \cos(\varphi + \alpha)}{(1 + (\vartheta - 1)s)^4} \\ \frac{dF}{d\varphi'} &= -\frac{4(\vartheta - 1)}{1 + (\vartheta - 1)s} \end{aligned} \quad (3.27)$$

After approximating φ , (x, y) coordinates can be integrated using the first two equations in (3.25) and the corresponding boundary conditions.

3.3 Load scenarios

The following load scenarios are defined to compare results and see the influence of each consideration. Each load case is tested with different values of the force parameters.

- First, a uniform, straight beam, rigidly supported with a concentrated load at the free end (tip load) is analyzed. This model serves to introduce the numerical methods for the more complex scenarios.

Table 3.1: Loading scenarios for a tip load.

Case	Loading	Type	Support
1	tip force	direction preserving	rigid support
2	tip force	angle preserving	rigid support

- Distributed load scenarios are also analyzed, first with a rigid support and then with an elastic support, in order to determine the influence of each consideration for further comparison. The load cases are the following:

Table 3.2: Loading scenarios for a distributed load.

Case	Loading	Support	Obs.
3	distributed force	rigid support	
4	distributed force	elastic support	
5	distributed force	rigid support	conicity
6	distributed force	elastic support	conicity
7	distributed force	rigid support	pre-curvature
8	distributed force	elastic support	pre-curvature
9	distributed force	rigid support	conicity & pre-curvature
10	distributed force	elastic support	conicity & pre-curvature

- Finally, a combined loading, between a concentrated load and a distributed load is applied. The load scenerarios are the same as in Table 3.2.

Table 3.3: Loading scenarios for combined loading.

Case	Loading	Support	Obs.
11	combined loading	rigid support	
12	combined loading	elastic support	
13	combined loading	rigid support	conicity
14	combined loading	elastic support	conicity
15	combined loading	rigid support	pre-curvature
16	combined loading	elastic support	pre-curvature
17	combined loading	rigid support	conicity & pre-curvature
18	combined loading	elastic support	conicity & pre-curvature

Chapter 4

Preliminary studies: mechanical behavior of beams under various load scenarios

In the previous chapter, the differential equation that governs the behavior of the beam model of a vibrissa under a concentrated and a distributed load is deduced (see (3.25)). In this chapter, different scenarios are considered, in order to analyze the influence of each parameter found in the system equation. These scenarios are defined in Tables 3.1 and 3.2.

4.1 General solution procedure

Two algorithms are implemented for the approximation of the solution, one for the rigid support case and another for the elastic support case. Both algorithms are based on the *shooting method*: Given a φ_1 (and φ_0 for the elastic support cases) the FDM algorithm is executed. If the conditions at the tip and the base are met, then the starting values are taken as a solution; if not, then new values of φ_1 and φ_0 are picked. As shown in the block diagrams in Figs. 4.1 and 4.2

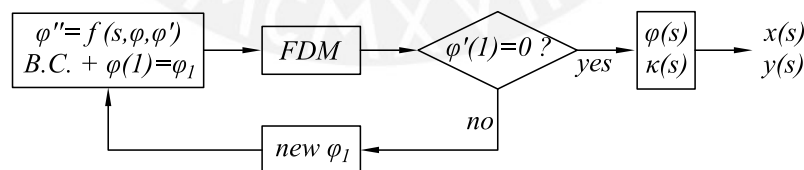


Figure 4.1: Block diagram used for the approximation of the solution for models with rigid support.

For both algorithms the search of new values is performed with the help of `fzero` function found in MATLAB, that implements the bisection method to search for the new value. This method can also be implemented by the user. After testing different values of the step size, $h = 0.01$ is chosen for comparison between results. A tolerance of $tol = 10^{-6}$ is used. Additionally, a maximum number of iterations of 100000 is used for the FDM.

For the cases with elastic support, since there is two iterations to be done, `fsolve` from MATLAB is tried. However, it does not offer acceptable results. Thus, an approach of using two loops with `fzero` is chosen.

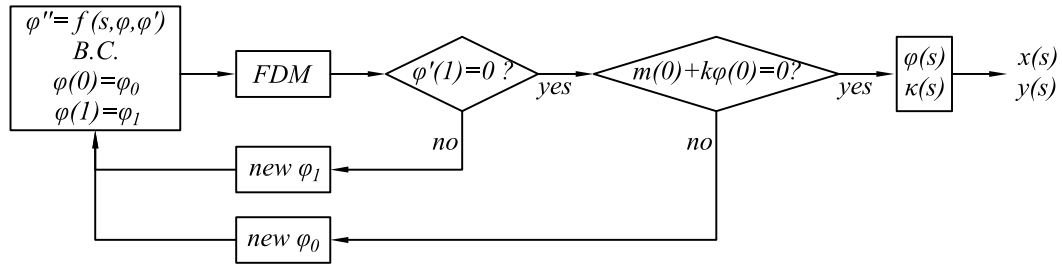


Figure 4.2: Block diagram used for the approximation of the solution for models with elastic support.

4.2 Concentrated force at the free end

The initial study case consists of a cantilever beam with a concentrated load at the free end, its cross section is considered to be constant along the length of the beam and there is no pre-curvature. Therefore, the following parameters are kept constant: q , ϑ , A , B , k . While the other parameters are varied.

$$\boxed{q = 0, \quad f, \quad \beta \in \{0, 45^\circ\}, \quad \vartheta = 1, \quad A = 0, \quad B = 0, \quad k = +\infty} \quad (4.1)$$

Remark 4.1 From now on, the boxed parameters describe the geometrical and load considerations for each study case. No further description is necessary for any case, since they all use the differential system of equations (3.25).

Note that two scenarios can be considered for this case, a DP load and an AP load as seen in Fig. 2.29.

4.2.1 Case 1: Direction preserving tip load

By applying the considerations in (4.1), (3.25) takes the form:

$$\kappa' = f \sin(\varphi + \beta) \quad (4.2)$$

with the boundary conditions of a rigid support.

The algorithm of solution displayed in Fig. 4.1 is used to approximate the elastica curve. The same algorithm is also used with the RK4 method for comparison purposes. One of the most important results that allow comparison are the tip (x, y) - coordinates of the deformed beam. For both approaches described before, the tip coordinates are displayed in Fig. 4.3, which can be compared to the results displayed in Fig. 2.31: both figures show that the beam tends to bend to a horizontal position, defined by $\beta = 0$. When the force angle is changed to $\beta = 45^\circ$, the beam tends to bend to this angle. The elastica curves are also plotted for quantitative and qualitative comparison (see Fig. 4.5).

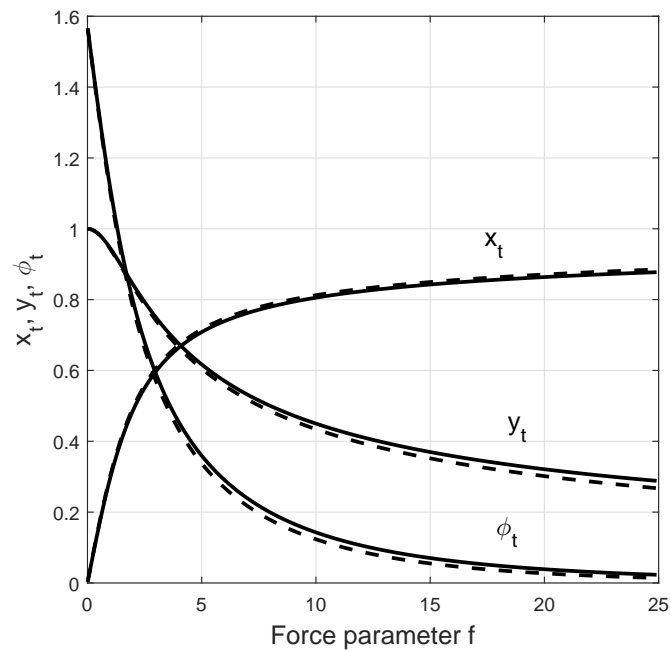


Figure 4.3: Tip coordinates (DP tip load) obtained through both approaches in function of f and $\beta = 0$. Continuous line: solution through FDM, dashed line: solution through RK4. For both methods: Step size $h = 0.01$ and tolerance of 10^{-6} .

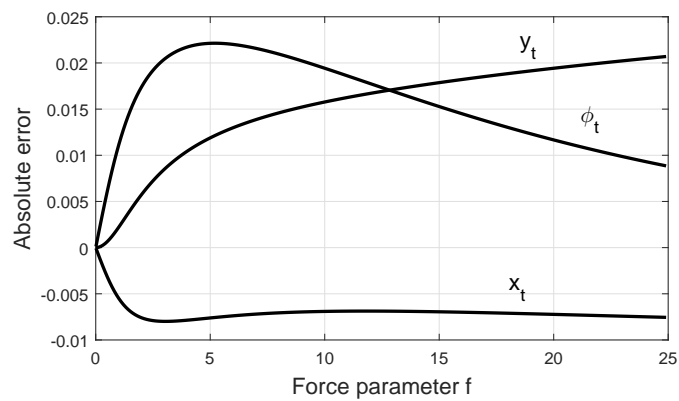


Figure 4.4: Absolute error between results in Fig. 4.3.

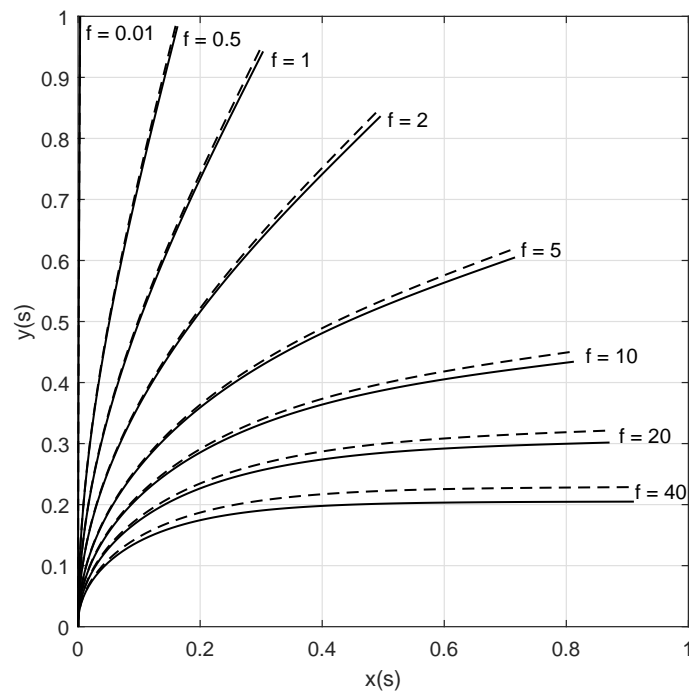


Figure 4.5: Elastica curves as function of f through both approaches. $\beta = 0$. Continuous line: solution through RK4, dashed line: solution through FDM. For both methods: Step size $h = 0.01$ and tolerance of 10^{-6} .

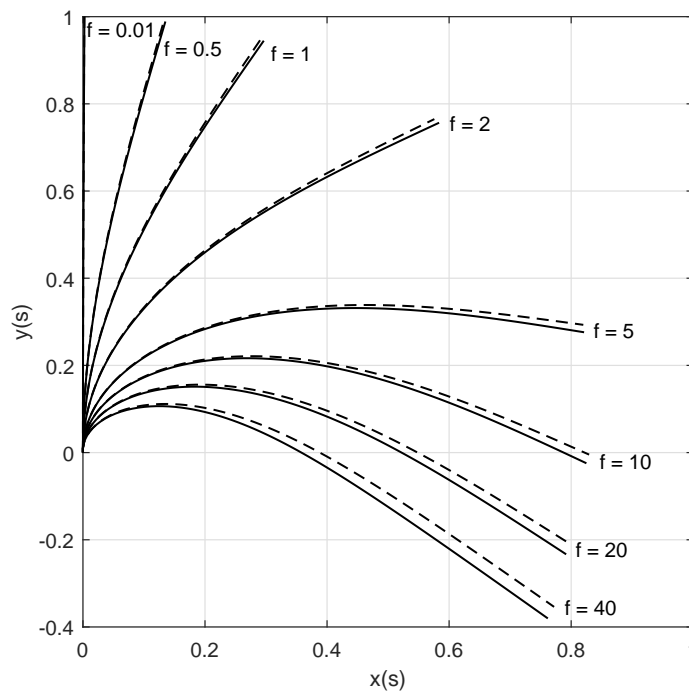


Figure 4.6: Elastica curves as function of f through both approaches. $\beta = 45^\circ$. Continuous line: solution through RK4, dashed line: solution through FDM.. For both methods: Step size $h = 0.01$ and tolerance of 10^{-6} .

Remark 4.2 To have an idea of the magnitude of the dimensionless values, the solutions found can be converted to a dimensional form. For instance, given the values of a rat's beta vibrissa in Table 2.2, the corresponding dimensional factor f_0 is 0.00004019. Thus, for a dimensionless force $f = 0.01$, the dimensional force is $F = 4.019 \cdot 10^{-7}$ N and for a dimensionless force $f = 40$, the dimensional force is 0.001607578 N. This values help to visualize the order of magnitude of the forces to which a vibrissa is subjected. To give further insight, for a 1 m long steel beam (200 GPa) with a 20 mm diameter circular cross section, a dimensionless force of 0.01 translates into 15.7 N (approximately 1.6 kg) and a dimensionless force of 40 translates into 62831 N, which is roughly 6.3 metric Tons.

In Figs. 4.3, 4.5 and 4.6, a difference between the results of both methods is observed (absolute error is plotted instead of relative due to the fact that for the tip deflection angle for large loads, the results tend to 0/0). Even though both work with the same tolerance (10^{-6}), the FDM has a higher truncation error, as explained before in Section 2.4.2. In order to have a better approximation with FDM, a smaller step-size should be used.

The variation of the force inclination angle β is also explored. Its effect is more clearly seen with large loads, due to the fact that the beam will try to bend in the direction given by the inclination.

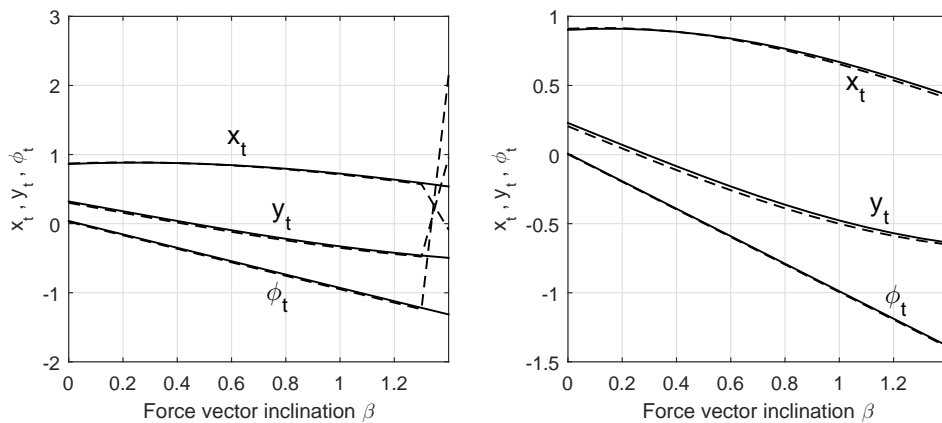


Figure 4.7: Tip coordinates (DP tip load) obtained through both approaches in function of force inclination β . Left: $f = 20$, right: $f = 40$. Continuous line: FDM, dashed line: RK4. For both methods: Step size $h = 0.01$ and tolerance of 10^{-6} .

Even when the RK4 approximation provides results with lesser truncation error, it was found that the algorithm itself is very sensitive to the initial approximation of $\kappa(0) = \kappa_{assumed}$, the FDM is less sensible. The following reasons have been found to increase the sensitivity to the initial approximation with both methods:

- very high loads,
- force inclination angle β close to $\pi/2$ (see (a) in Fig. 4.7),
- applying the load in one step.

A solution to help reduce the sensitivity to the initial conditions is applying the load in load-steps. However, this may greatly increase the solution time since the problem has to be solved multiple times, especially in posterior cases.

4.2.2 Case 2: Angle preserving tip load

The formulation of the cantilever beam under an AP load at the free end is similar as the last case. However, since the force is considered AP, a modification of the differential equation (3.25) is needed.

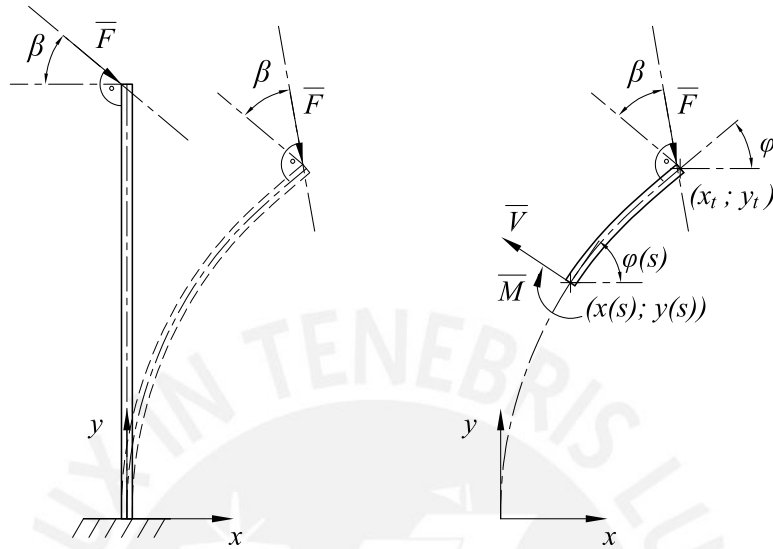


Figure 4.8: Sketch of the deformation and section analysis of the cantilever beam under an AP load

The main change is the appearance of a new term φ_1 in the differential equation, see (4.3). The boundary conditions are the same used in the previous scenario, corresponding to a fixed, rigid support.

$$\kappa' = f \cos(\varphi + \beta - \varphi_1) \quad (4.3)$$

The algorithm shown in Fig. 4.1 can be applied to approximate (4.3) using the FDM. Similarly as the previous case, the tip results are plotted. It is worth noticing that the curves are not smooth and present strong deviations near certain values. This problems are encountered first when the tip angle φ_1 reaches its minimum value ($-\pi/2$) at around $f = 15$ and then starts to bend to the negative side of the x axis. A similar phenomena occurs at $f = 25$. The authors of [Nallathambi et al. 2010] also faces this issue, it can be resolved by identifying beforehand this points where φ_1 starts to go “backwards” (reaches $-\pi/2$) and increasing the tolerance in this range. It is near these points that the results are extremely dependent on the initial value given for the iteration.

This behavior is already explained in the previous scenario. After reviewing Fig. 4.9, it is shown that for AP loads of $f = 5$ a similar elastica is obtained for a DP load of $f > 20$. This suggest that an AP load $f > 5$ could already be considered as very high load. Also another possible error source is that the maximum number of iterations (100000) is reached during the simulation with no result found within the specified tolerance 10^{-4} , this may indicate that a larger number of iterations must be set to achieve the desired tolerance.

Important remark: No further analysis is done for this load scenario, since very high loads do not produce physically meaningful results. Large deformations such as the ones shown in Fig. 4.10 are not always physically possible, since most linear-elastic materials may reach the yield point before “coiling” and are subjected to material non-linearities. These high loading scenarios are only possible with beams with high slenderness.

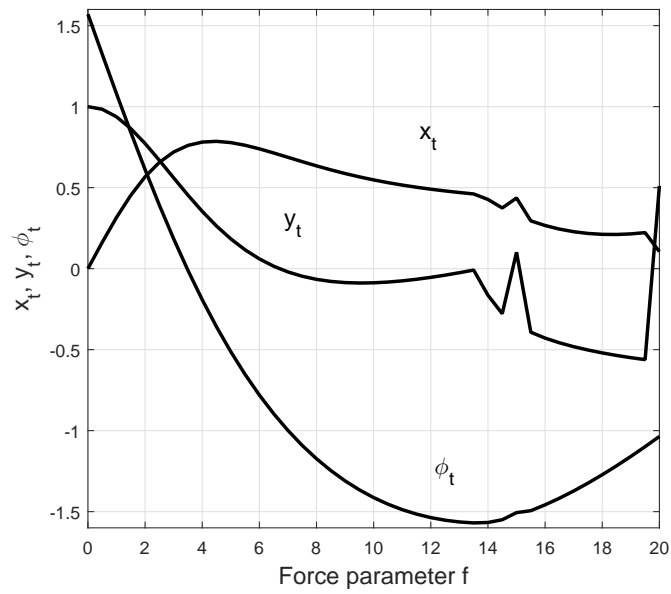


Figure 4.9: Tip coordinates obtained through finite difference method. Step size $h = 0.01$ and tolerance of 10^{-4} .

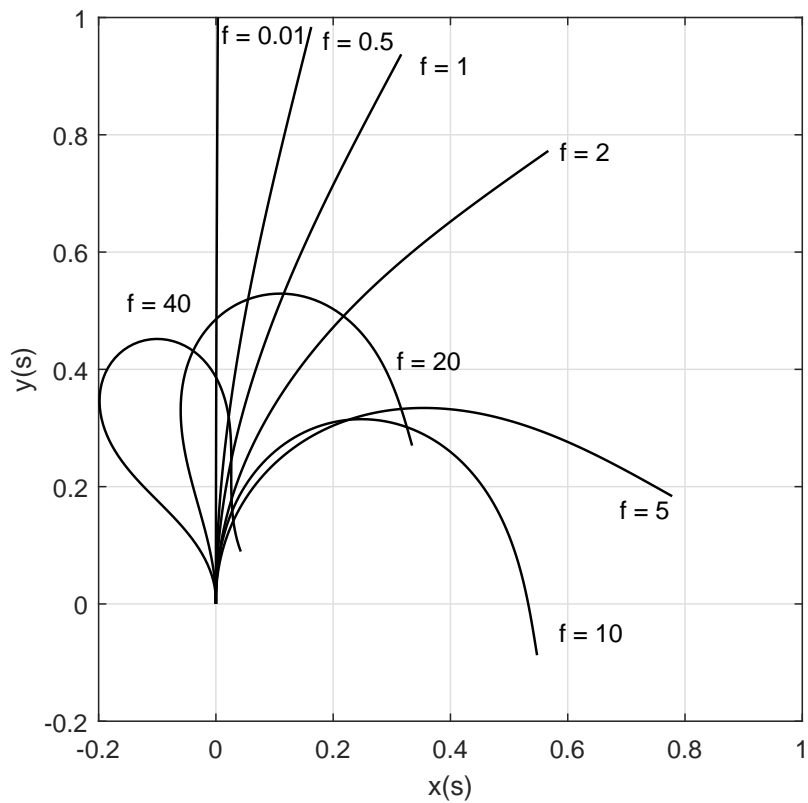


Figure 4.10: Elastica curves as function of f through both approaches. Step size $h = 0.01$ and tolerance of 10^{-4} .

4.3 Distributed load along the shaft

As shown in Table 3.2, different scenarios of beams under distributed loads are analyzed in order to study the influence of each parameter in the results.

4.3.1 Case 3: Rigid support, constant cross section and straight beam

This is the first case considered for a cantilever beam under distributed load. This model has the following fixed parameters: f, ϑ, A, B, k . While the other parameters are varied.

$$q > 0, \quad \alpha \in \{0, 45^\circ\}, \quad f = 0, \quad \vartheta = 1, \quad A = 0, \quad B = 0, \quad k = +\infty \quad (4.4)$$

Based on the considerations on (4.4), the system differential equation becomes:

$$\kappa' = q_d(1 - s) \sin(\varphi + \alpha) \quad (4.5)$$

In a same manner as explained in the DP tip load, the FDM and RK4 methods are applied to solve (4.5) by using the algorithm displayed in Fig. 4.1

Again, the coordinates of the tip of the deformed beam are of great importance to compare results. As seen in Fig. 4.11, the tip angle tends to zero, meaning that the beam tends to bend to a horizontal position which corresponds to $\alpha = 0$, similarly as the DP tip load case. The behavior described before for a DP load can also be seen in Fig. 4.12. However, this tendency to bend to a horizontal position is “slower” for a distributed DP load (Fig. 4.12) than for a single DP tip load (Fig. 4.5). The reason is that part of the distributed load is acting close to the support, thus producing a small moment. The DP tip load, on the other hand, acts on the farthest point of the beam, thus producing a larger moment. Furthermore, the magnitude of a distributed DP load is dependent on the length of the beam where it is applied, whereas a DP tip load is independent of the length.

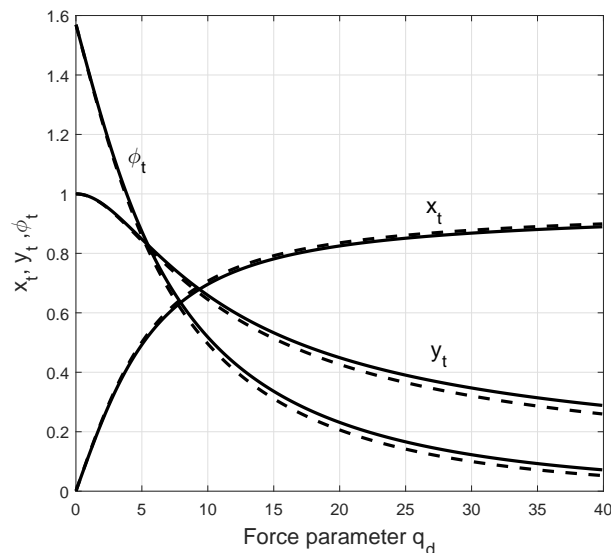


Figure 4.11: Tip coordinates obtained through both approaches in function of the force parameter q . Force inclination $\alpha = 0$. Continuous line: Solution through RK4, dashed line: solution through FDM.

When comparing the results obtained through FDM and RK4 methods, there is also an evident variation; just as in the DP tip load case, this difference is also due to the

truncation error between the applied methods. A sensitivity to the starting values is also found; as in the DP tip load case, the sensitivity is higher with the RK4 method.

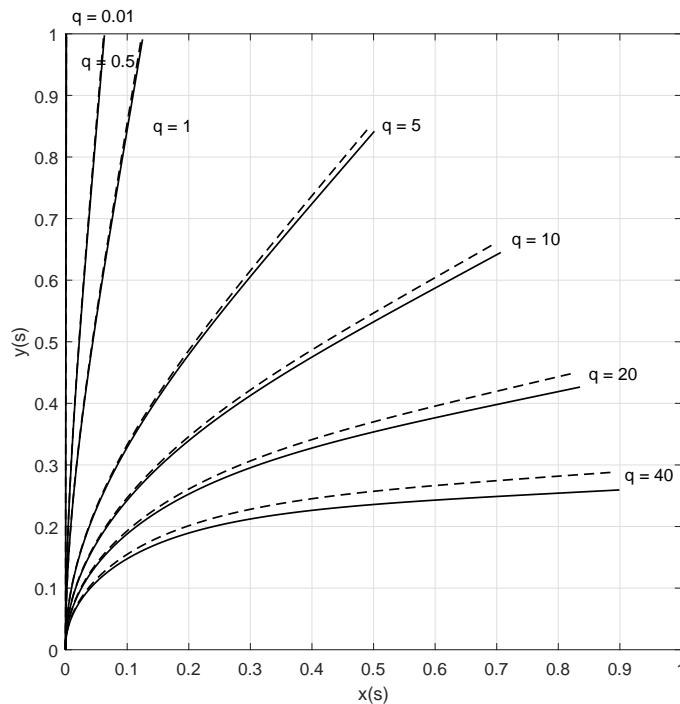


Figure 4.12: Elastica curves for different values of the load parameter q obtained through both methods. Force inclination $\alpha = 0$. Continuous line: Solution through RK4, dashed line: solution through FDM.

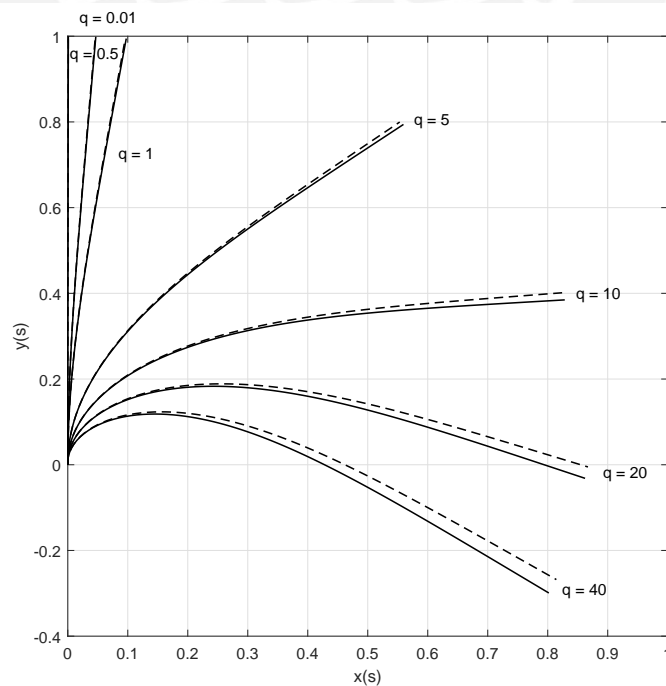


Figure 4.13: Elastica curves for different values of the load parameter q obtained through both methods. Force inclination $\alpha = 45^\circ$. Continuous line: Solution through RK4, dashed line: solution through FDM.

Once again, as the force increases the beam tends to bend to the angle of the force α , as shown in Fig. 4.13, where it bends to 45° .

4.3.2 Case 4: Elastic support, constant cross section and straight beam

A variation of the previous case consists on varying the stiffness of the support:

$$q > 0, \quad \alpha = 0, \quad f = 0, \quad \vartheta = 1, \quad A = 0, \quad B = 0, \quad k > 0 \quad (4.6)$$

The differential equation is the same as in the last scenario, see (4.5). However, the boundary conditions are changed to those of a elastic support (3.21) and (3.22).

The solution is approximated through the FDM, using the algorithm displayed in Fig. 4.2. To compare and appreciate the influence of the elastic support, elasticas are plotted with the same force parameter q and varying support stiffness k .

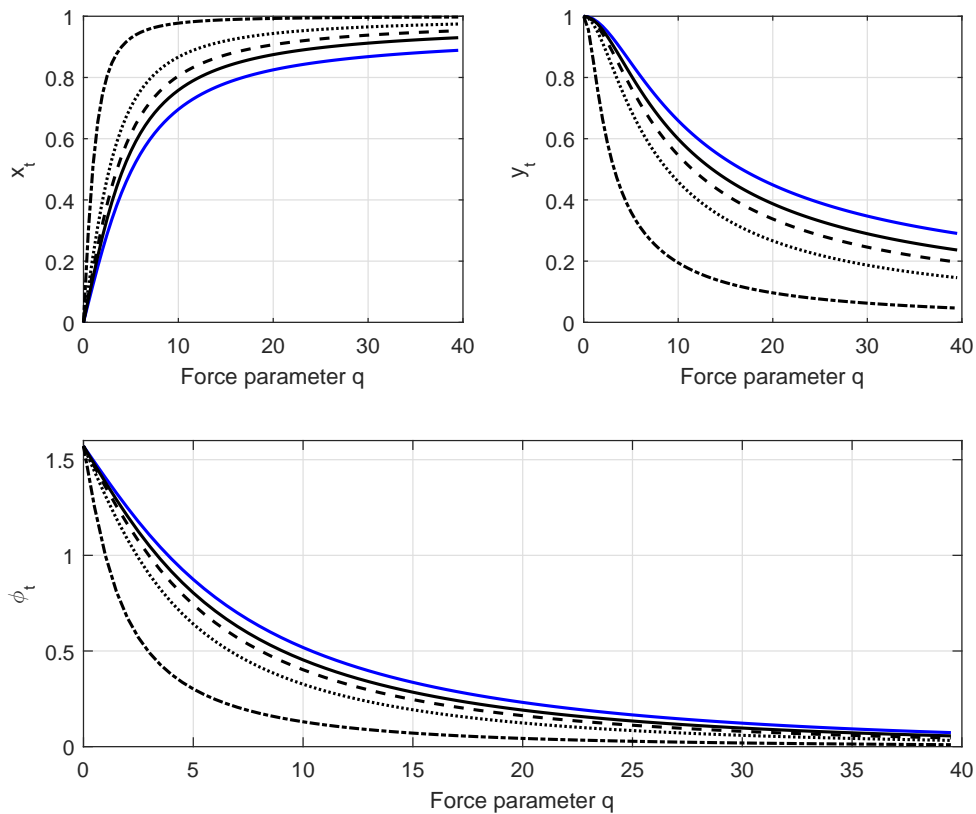


Figure 4.14: Tip coordinates for a beam under different distributed horizontal loads $\alpha = 0$. Continuous blue line: $k = +\infty$, continuous black line: $k = 20$, dashed line: $k = 10$, dotted line: $k = 5$, dashed and dotted line: $k = 1$.

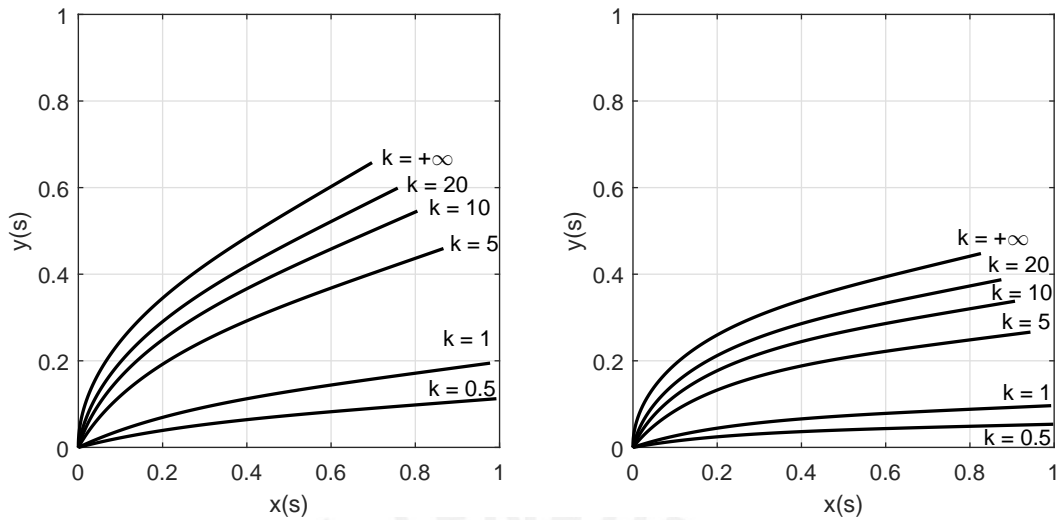


Figure 4.15: Elastica curves for a beam on elastic support (various stiffnesses) under an horizontal ($\alpha = 0$) Left: $q = 10$, right: $q = 20$.

It can be seen in Fig. 4.15 that with low stiffness in the support, the beam actual deflection is small, since most of the deformation is absorbed by the torsional spring. It can be concluded that the stiffness of the torsional spring has a large influence on the stiffness of the system, due to the fact that it absorbs the force applied.

4.3.3 Case 5: Rigid support, conical, straight beam

A characteristic found in vibrissae is their natural conicity. The beam (that represents the vibrissa) is regarded as conical, rigidly supported and not pre-curved. The parameters q and ϑ are varied, while the rest are kept constant.

$$q > 0, \quad \alpha = 0, \quad f = 0, \quad 0 < \vartheta < 1, \quad A = 0, \quad B = 0, \quad k = +\infty \quad (4.7)$$

Applying these considerations converts the system equation into:

$$\kappa' = \frac{qa(1-s)\sin(\varphi + \alpha)}{(1 + (\vartheta - 1)s)^4} - \frac{4(\vartheta - 1)}{1 + (\vartheta - 1)s}\varphi' \quad (4.8)$$

with the boundary conditions of a rigid support. Again the algorithm shown in Fig. 4.1 is used.

It is worth noticing that for certain combinations of conicity ϑ and force q the solution does not converge, this problem is also encountered by Kemper 1968, who used a trial&error-method for these combinations. The FDM however reduces the combinations for which there is no convergence in the results. Even though, the combinations of conicity and force parameters that produce divergence seem to be random, this phenomenon is more common with conicity parameters ϑ lower than 0.2. Since the bending stiffness of the beam is reduced, the resulting elastica is similar to that of a uniform beam with a larger force parameter (it was discussed before that large force parameters may produce instability and divergence in the results).

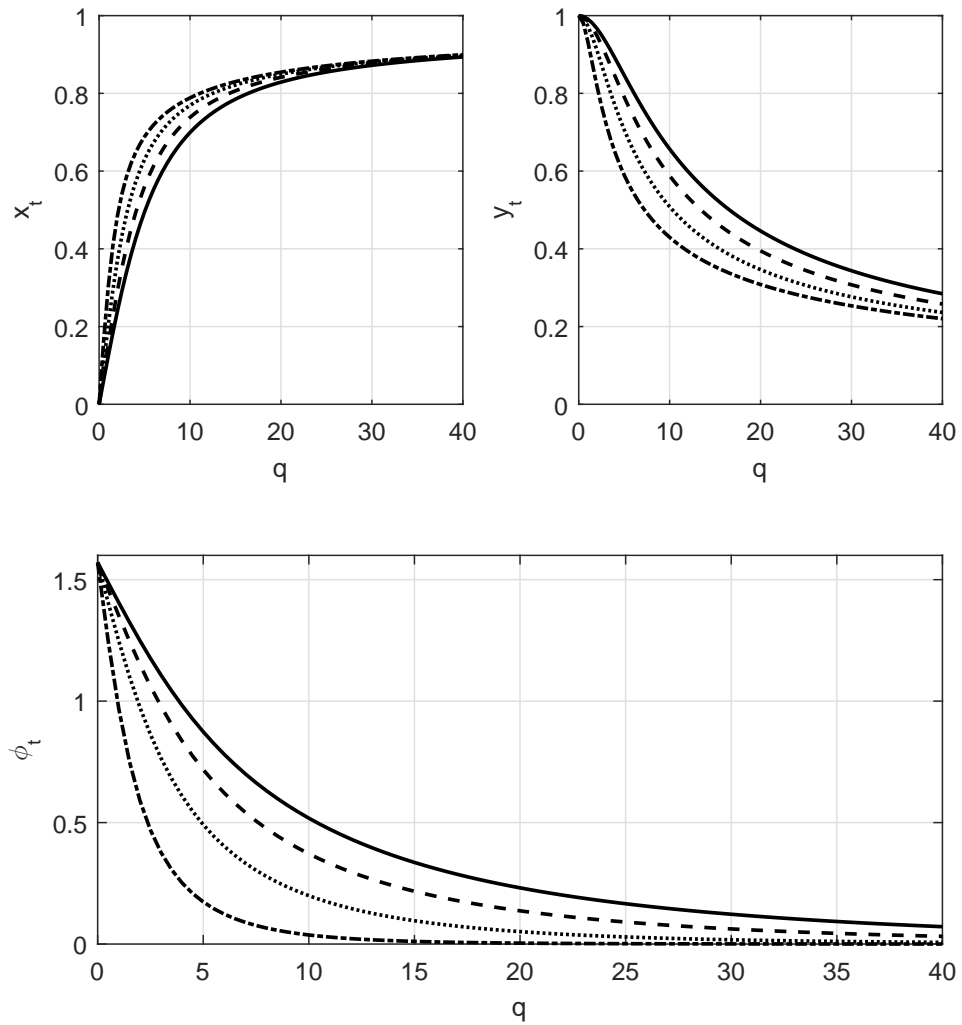


Figure 4.16: Tip coordinates in function of the force parameter q and α and varying ϑ : Continuous line: $\vartheta = 1$, dashed line: $\vartheta = 0.75$, dotted line: $\vartheta = 0.5$, dashed and dotted line: $\vartheta = 0.25$.

4.3.4 Case 6: Elastic support, conical, straight beam

A complement of the conical beam consideration is the elastic support at the base, which means that the parameter k is now varied along q .

$$q > 0, \quad \alpha = 0, \quad f = 0, \quad 0 < \vartheta < 1, \quad A = 0, \quad B = 0, \quad k > 0 \quad (4.9)$$

The differential equation is the same as in the last scenario, see (4.8), along with the boundary conditions of a elastic support. The solution is sought with the algorithm in Fig. 4.2.

The influence of the elastic support becomes evident when comparing the tip results for different torsional stiffness of the support. The tip of the beam tends to go a horizontal position with a lower load due to the combined effect of loss of bending stiffness due to conicity and the elastic support. Figure 4.17 show how reducing the torsional stiffness k at the base influences the tip coordinates of beams of varying θ values.

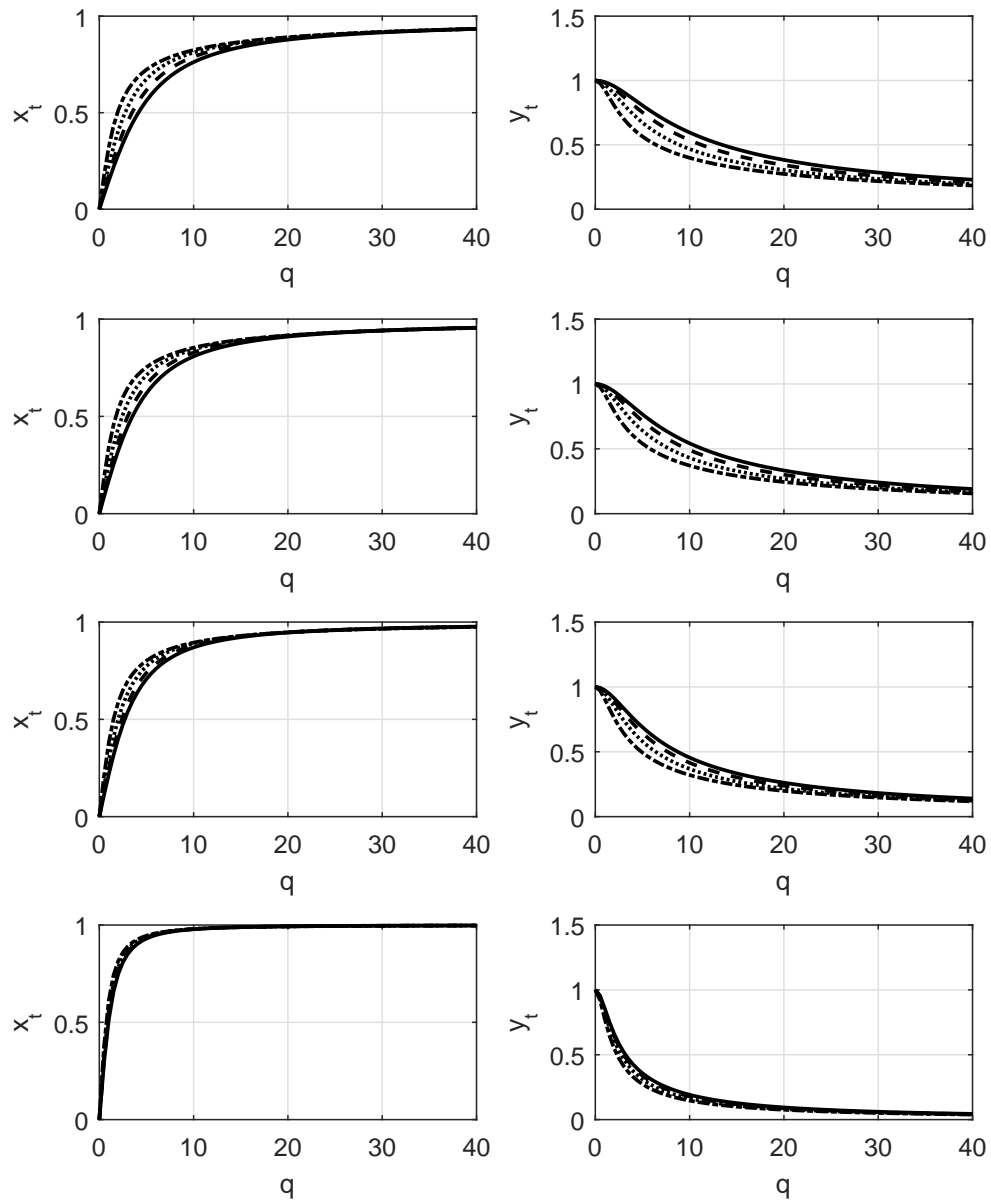


Figure 4.17: Tip coordinates x_t and y_t as a function of the load parameter q_d for different torsional stiffness of the torsional spring at the base k . Top row: $k = 20$, second row: $k = 10$, third row: $k = 5$, bottom row: $k = 1$.

4.3.5 Case 7: Rigid support, constant cross section, pre-curved beam

As explained before, pre-curvature helps reduce VIV and improves the measurements. For this scenario, the variation of q and the pre-curvature parameters A and B is studied, the other parameters are kept constant.

$$\boxed{q > 0, \quad \alpha = 0, \quad f = 0, \quad \vartheta = 1, \quad A, B, \quad k = +\infty} \quad (4.10)$$

The differential equation then becomes:

$$\kappa' = q_d(1 - s) \sin(\varphi + \alpha) + A \quad (4.11)$$

with the following boundary conditions of a rigid support. Once again, the solution procedure follows the algorithm in Fig. 4.1.

This scenario takes into consideration different variations of the pre-curvature equation κ_0 (see (3.5)). For this case, instead of showing the coordinates of tip of the beam after deformation, only the elasticas with different pre-curvature parameters are plotted, since they provide a better visualization of the deformation and the influence of the pre-curvature.

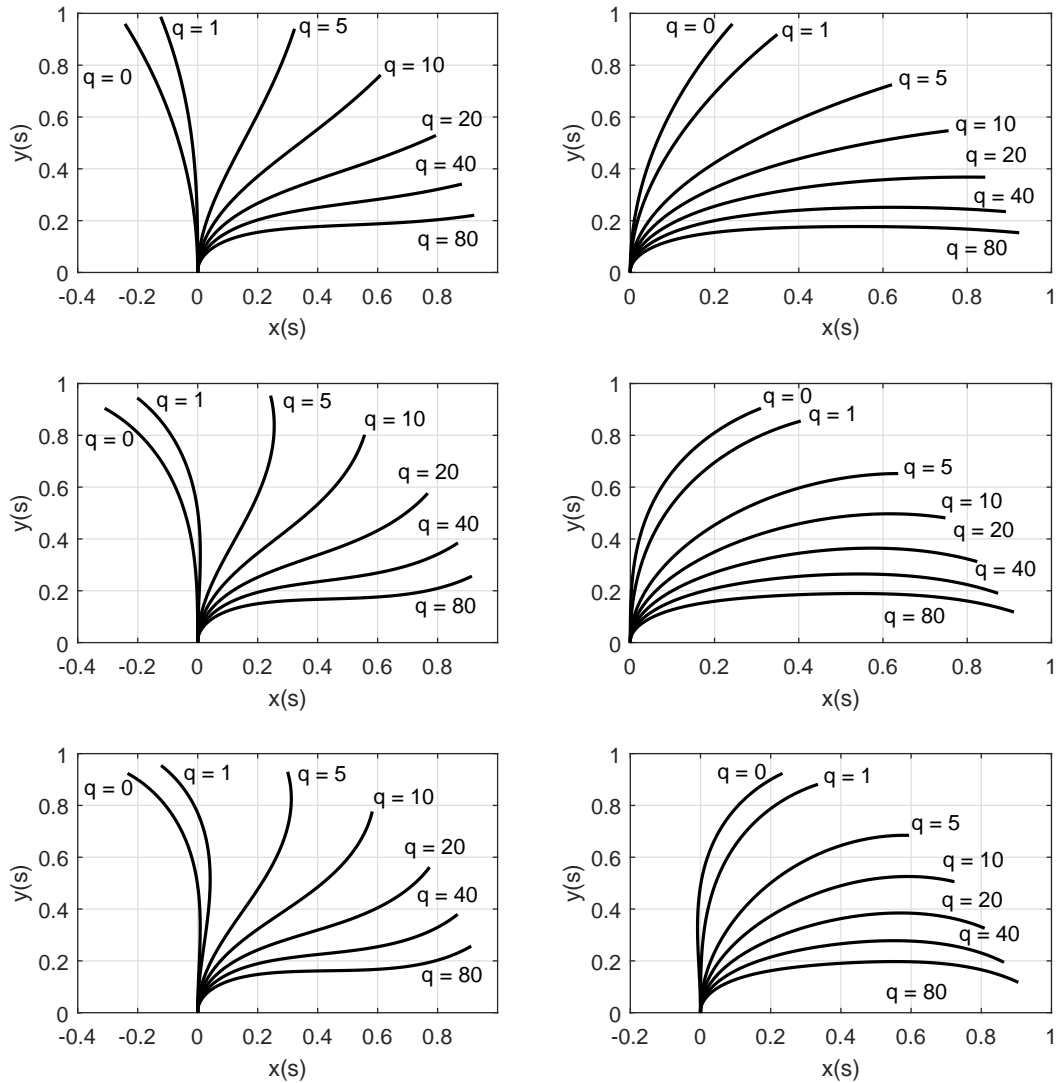


Figure 4.18: Elasticas of multiple pre-curved beams. Top left: $A = 0$ and $B = 0.5$, top right: $A = 0$ and $B = -0.5$, middle left: $A = 2$ and $B = 0$, middle right: $A = -2$ and $B = 0$, bottom left: $A = 3$ and $B = -0.5$, bottom right: $A = -3$ and $B = 0.5$.

Note that the behavior changes for different pre-curvatures:

- for constant positive pre-curvatures $A = 0, B > 0$ and $A > 0, B > 0$: the pre-curvature points at the “opposite direction” as the force. By increasing the force, the curvature changes sign and an inflection point appears. This point moves along the shaft but never reaches the tip, since in this point the bending moment is zero. Note that in the top left graph in Fig. 4.18 the purple elastica represent a load of 80, an extremely high value.
- for constant negative pre-curvatures $A = 0, B < 0$ and $A < 0, B < 0$: the pre-curvature points at the “same direction” as the force. Thus, there is no inflection point and the shaft bends even more, as if a larger load was applied on the beam.

This pre-curvature achieves great deflections “faster” with lower values of internal bending moment as seen in top right graph in Fig. 4.18. Lower internal bending moment translates into lower internal normal stress.

- for variable pre-curvatures $A \neq 0$, $B \neq 0$: depending on the values of A and B , the behavior is similar to one of the cases explained above.

4.3.6 Case 8: Elastic support, constant cross section, pre-curved beam

A complement of the curved beam consideration is the elastic support at the base, the variation of k is now studied.

$$\boxed{q > 0, \quad \alpha = 0, \quad f = 0, \quad \vartheta = 1, \quad A, B, \quad k > 0} \quad (4.12)$$

The deflection is governed by (4.11) with boundary conditions corresponding to a elastic support.

In a similar manner to the rigidly supported curved beam, the elasticas with different support rigidity are shown, instead of the tip coordinates, since they provide a better visualization of the deformation and the influence of the pre-curvature.

It can be appreciated Fig. 4.19 in that once again the stiffness of the support has a great influence on the behavior of the system. For very small stiffness at the base, most of the deformation is absorbed by the spring, thus the beam suffers small strain and stress, this happens regardless of the pre-curvature. For pre-curvature that points in the “same direction” as the force, the beam bends horizontally “faster” than any previous cases, due to the combined effect of the pre-curvature and the elastic support.

4.3.7 Case 9: Rigid support, conical and pre-curved beam

This case describes the behavior of a vibrissa with the former considerations, conicity and pre-curvature. The variation of ϑ , A and B are studied.

$$\boxed{q = 10, \quad \alpha = 0, \quad f = 0, \quad 0 < \vartheta < 1, \quad A, B, \quad k = +\infty} \quad (4.13)$$

$$\kappa' = \frac{q_d(1-s)\sin(\varphi+\alpha)}{(1+(\theta-1)s)^4} - \frac{4(\theta-1)}{1+(\theta-1)s}(\varphi' - As - B) + A \quad (4.14)$$

With the boundary conditions of a rigid support. The algorithm for the approximation of the solution is the one displayed in Fig. 4.1. Once again different pre-curvature equations are evaluated, therefore, it is more useful to plot the elastica curves to appreciate the deformation.

The reduction in bending stiffness due to tapering produces an extra deformation at the tip of the beam when compared to the untapered model, as seen in Fig. 4.20. When reducing ϑ , the tip of the beam tends to bend to the direction of the force faster than with a beam with constant pre-curvature. The direction of the precurvature only delays or accelerates this change.

For beams with pre-curvature pointing in the same and opposite direction as the force, even larger deformations are achievable due to the tapering, when comparing it with the untapered model. Tapering also reduces the internal bending moment, since the system stiffness is reduced.

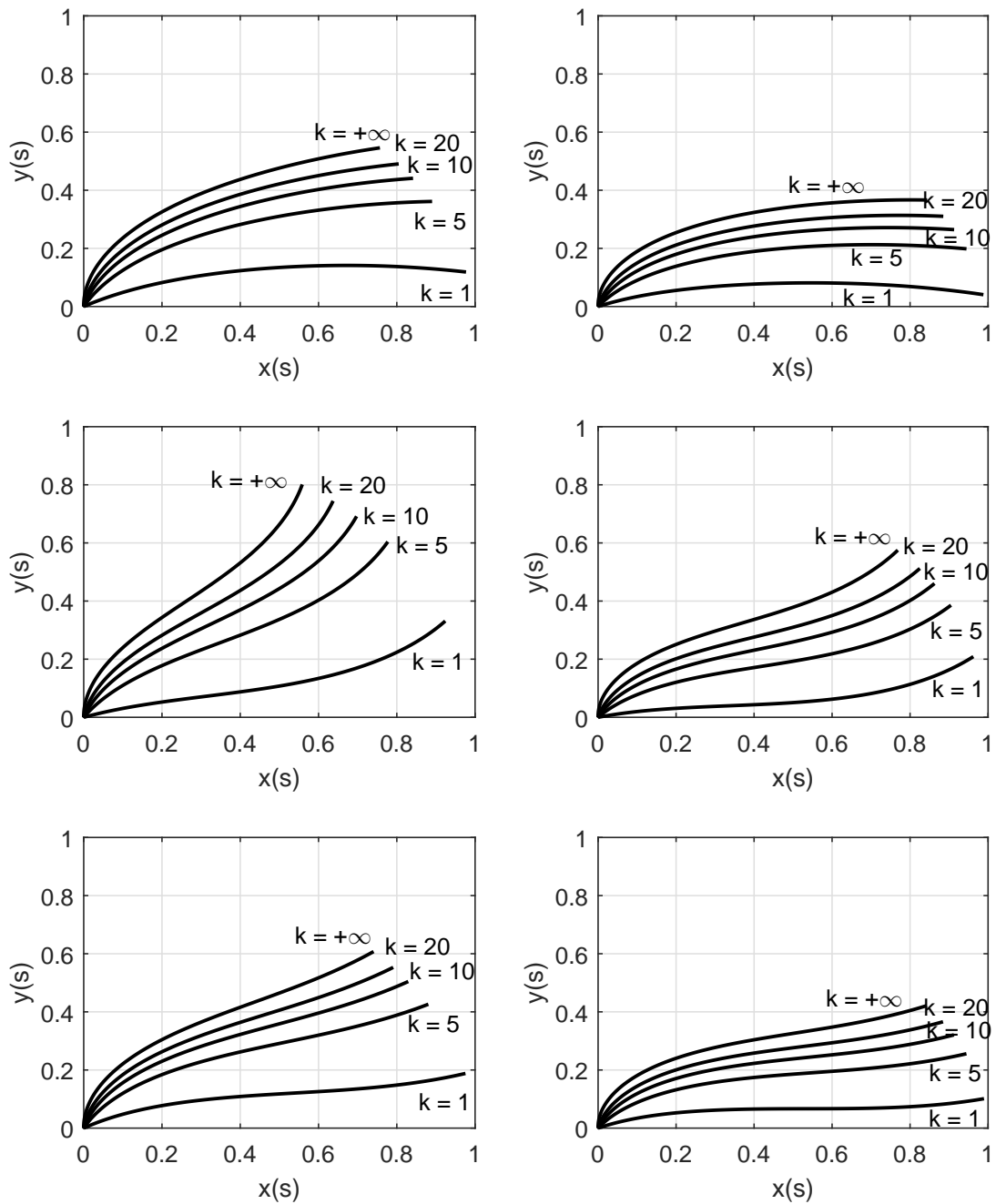


Figure 4.19: Elasticas of pre-curved beams under a distributed load of $q = 10$ on the left column and $q = 20$ on the right column. The pre-curvature parameters for the top row are $A = 0$ and $B = -0.5$; for the middle row $A = 2$ and $B = 0$; and $A = 2$ and $B = -1$ for the bottom row.

4.3.8 Case 10: Elastic support, conical and pre-curved beam

This case describes completely the behavior of a vibrissa with the four former considerations in a more accurately manner. Vibrissae like sensors for fluid flow detection must take all these considerations into account: conicity, pre-curvature, and elastic support:

$$\boxed{q = 10, \quad \alpha = 0, \quad f = 0, \quad 0 < \vartheta < 1, \quad A, B \neq 0, \quad k > 0} \quad (4.15)$$

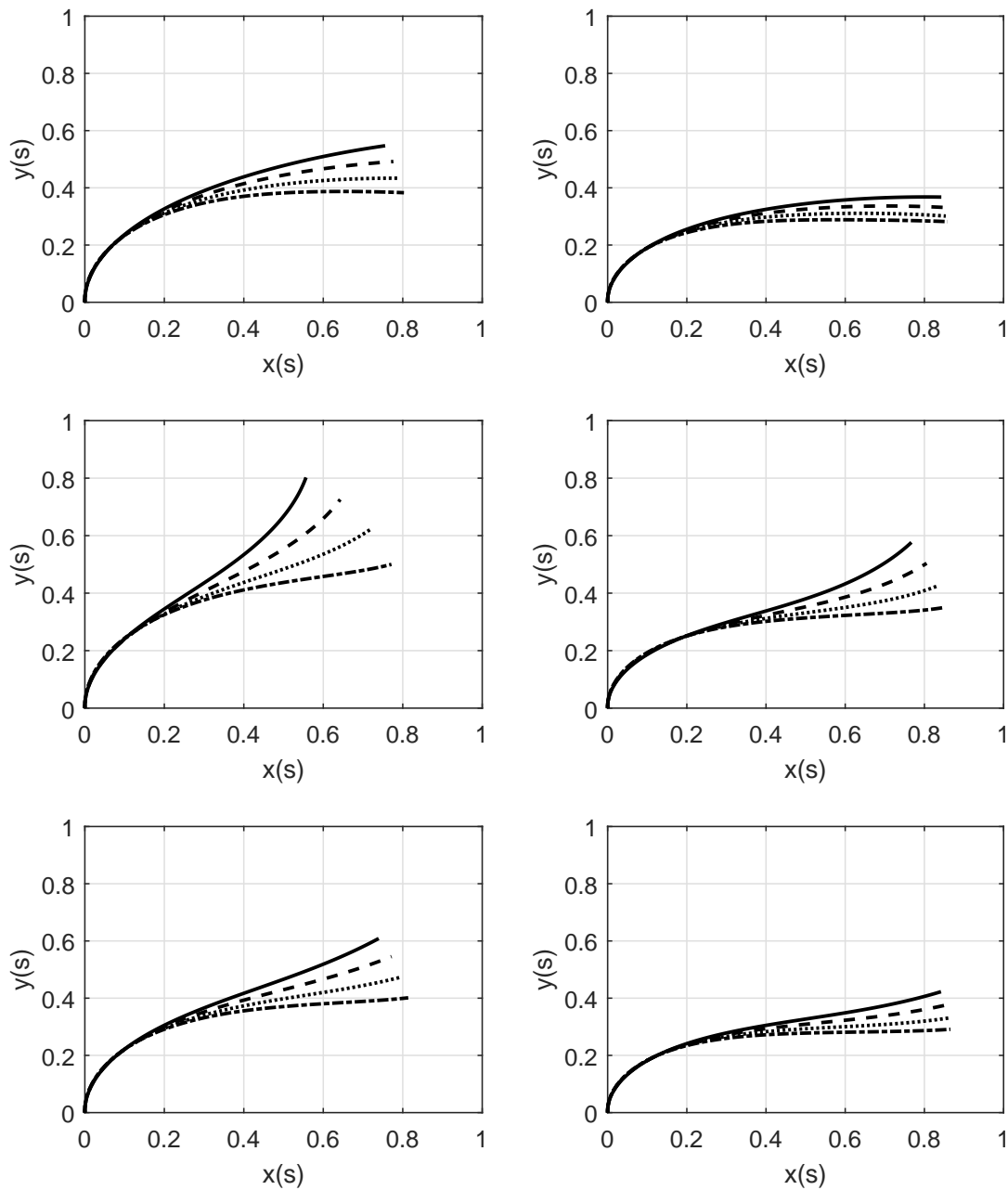


Figure 4.20: Elasticas of multiple vibrissae with different ϑ , with different pre-curvatures: Top right: $A = 0$ and $B = -0.5$, top left: $A = -2$ and $B = 0$, bottom: $A = 1$ and $B = -0.5$. All beams are under a distributed loads of $q = 10$ and $\alpha = 0$. Continuous line: $\vartheta = 1$, dashed line: $\vartheta = 0.75$, dotted line: $\vartheta = 0.5$, dashed and dotted line: $\vartheta = 0.25$.

The differential equation then becomes (4.14) with the boundary conditions of an elastic support, shown in (3.21) and (3.22).

In a similar manner as in the case in Section 4.3.8, elasticas with different parameters are displayed in order to appreciate the behavior of the bent vibrissae.

It can be seen in Fig. 4.21 the influence of each parameter. For example, torsional stiffness higher than 20, could be considered as “infinite” or a rigid support for practical purposes. It can also be deduced that reducing the conicity parameter θ tends to produce a straightening of the tip of the beam due to the loss of stiffness.

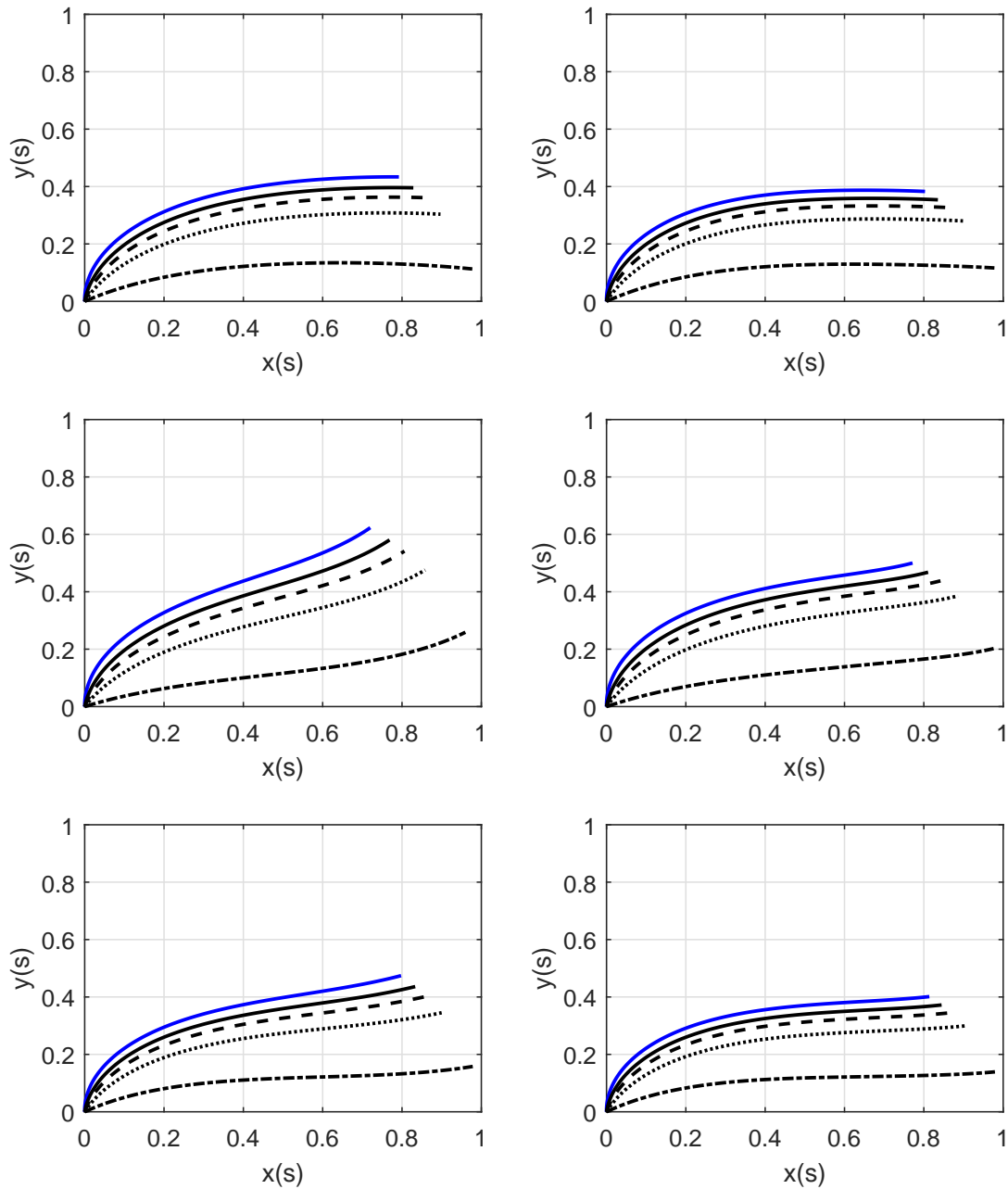


Figure 4.21: Elasticas of conical, pre-curved vibrissae, with varying stiffness of the elastic support. Top row: $A = 0$ and $B = -0.5$, middle row: $A = 2$ and $B = 0$, bottom row: $A = 2$ and $B = -1$. Left column: $\vartheta = 0.5$, right column: $\vartheta = 0.25$. For all cases: $q = 10$. The stiffness at the support changes with every curve: Continuous blue: $k = +\infty$, continuous black: $k = 20$, dashed: $k = 10$, dotted: $k = 5$, and dashed dotted $k = 1$.

4.4 Combined loading

Equation (3.25) considers both a single concentrated load at the end of the beam and a distributed load along the shaft. In the previous sections, only one load at the time is considered. In this section, the influence of both loads at the same time is analyzed, the relationship between the magnitudes of both forces is used to compare results.

$$\lambda := \frac{ql}{f} \quad (4.16)$$

Remark 4.3 Notice that the length of the vibrissa l is used in (4.16), since the distributed force needs a longitude in order to be dimensionally compatible with the concentrated load. The values of λ that are analyzed are:

$$\lambda \in \{0.5, 1, 2\} \quad (4.17)$$

For all scenarios, the selected loads are:

Table 4.1: Values of q , f and λ for study cases 9 to 16.

Scenario	1	2	3
λ	0.5	1	2
q	5	5	5
f	10	5	2.5

Remark 4.4 Note that for the analysis the distributed force is kept constant. During the object detection analysis in the forthcoming chapters, it is considered that there is no change in the fluid load. Furthermore, the tip load varies in magnitude and direction depending on the contour.

4.4.1 Case 11: Combined load, uniform beam, no pre-curvature, rigid support

The considerations of the first case of combined load are summarized in (4.18):

$$q = 5, \quad \alpha = 0, \quad f \in \{2.5, 5, 10\}, \quad \beta \in \{30^\circ, 45^\circ\}, \quad \vartheta = 1, \quad A, B = 0, \quad k = +\infty \quad (4.18)$$

The results displayed (see Fig. 4.22) show the results for different values of β . By increasing β , the beam tends to bend to said angle. This fact becomes evident with higher f , or $\lambda = 0.5$.

4.4.2 Case 12: Combined load, uniform beam, no pre-curvature, elastic support

The considerations of the second case of combined load are summarized in (4.19). The variation of the stiffness of the spring at the support is evaluated:

$$q = 5, \quad \alpha = 0, \quad f \in \{2.5, 5, 10\}, \quad \beta = 30^\circ, \quad \vartheta = 1, \quad A, B = 0, \quad k > 0 \quad (4.19)$$

A further analysis of the last scenario considers a variable stiffness of the torsional spring. It can be seen again that for low values of k (e.g. bottom right in Fig. 4.23), the deformation of the beam is reduced (compared to top left in Fig. 4.23).

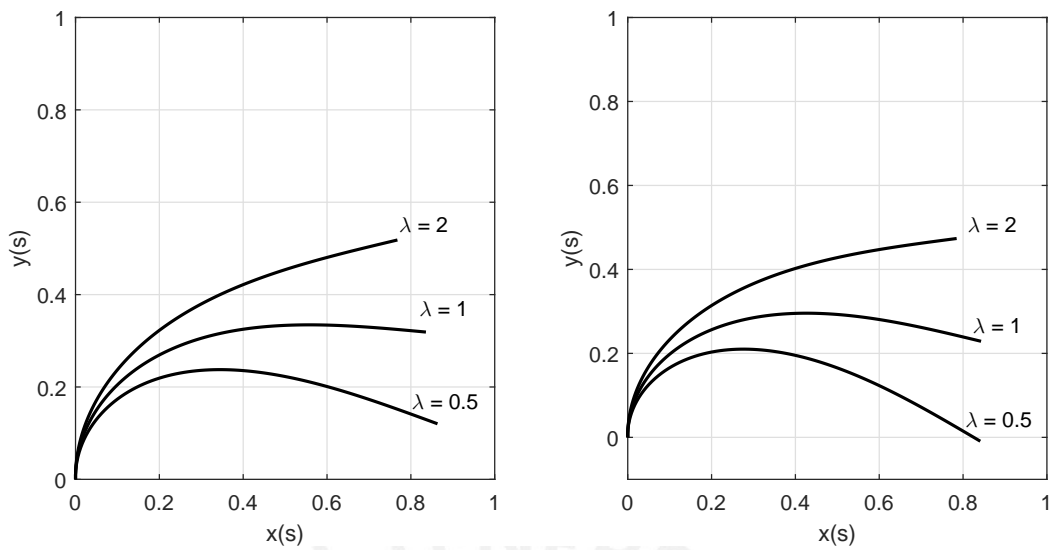


Figure 4.22: Elasticas for $q = 5$, $\alpha = 0$, $\lambda \in \{0.5, 1, 2\}$. Left: $\beta = 30^\circ$, right: $\beta = 45^\circ$.

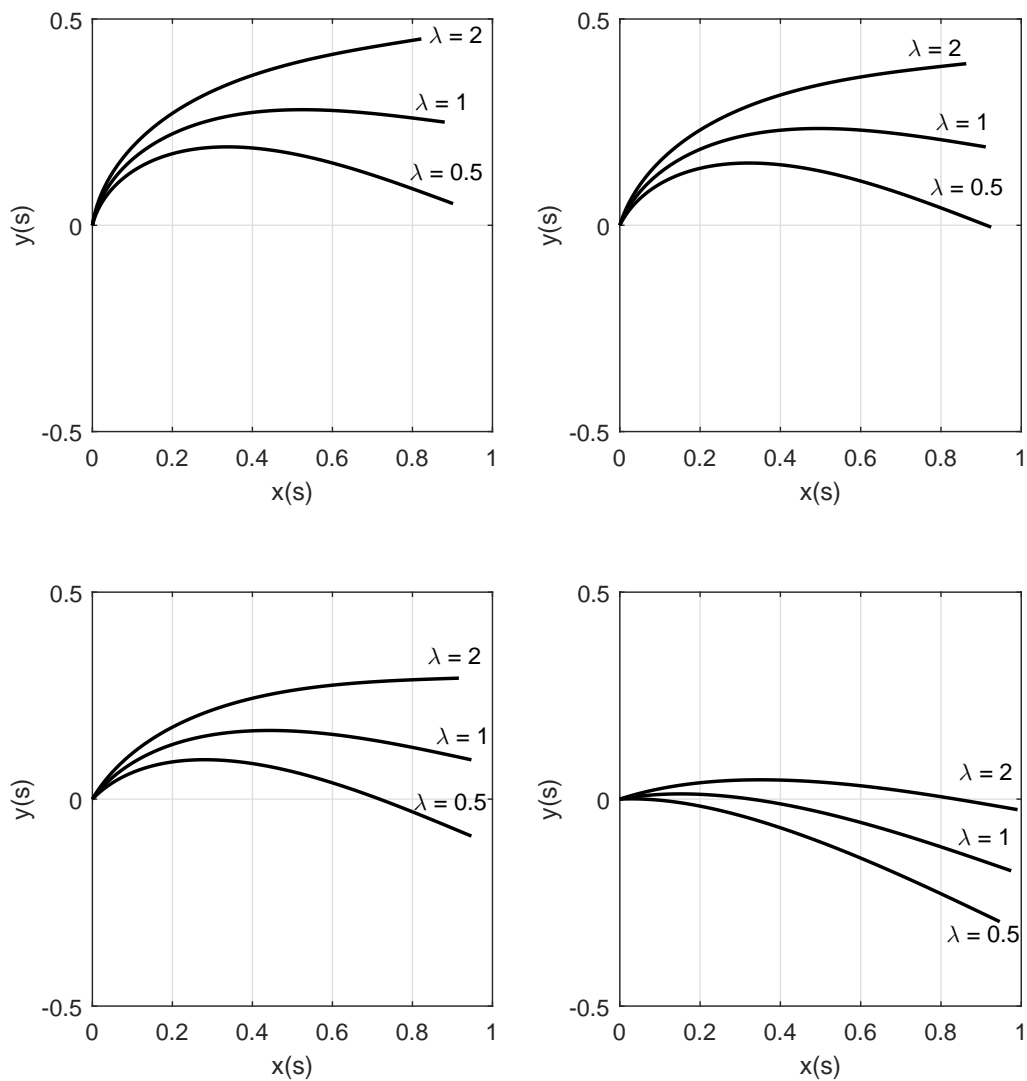


Figure 4.23: Elasticas for $q = 5$, $\alpha = 0$, $\lambda \in \{0.5, 1, 2\}$, $\beta = 30^\circ$. Top left: $k = 20$, top right: $k = 10$, bottom left: $k = 5$, bottom right: $k = 1$.

4.4.3 Case 13: Combined load, tapered beam, no pre-curvature, rigid support

The considerations of the third case of combined load are summarized in (4.20). The variation of the conicity parameter ϑ is evaluated:

$$\boxed{q = 5, \quad \alpha = 0, \quad f \in \{2.5, 5, 10\}, \quad \beta = 30^\circ, \quad 0 < \vartheta < 1, \quad A, B = 0, \quad k = +\infty} \quad (4.20)$$

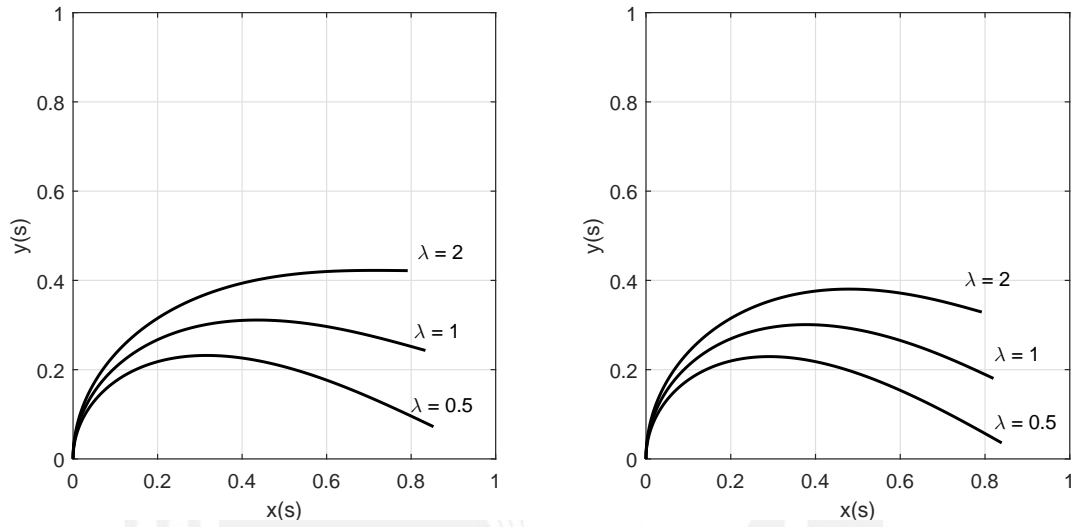


Figure 4.24: Elasticas for $q = 5$, $\alpha = 0$, $\lambda \in \{0.5, 1, 2\}$, $\beta = 30^\circ$. Left: $\vartheta = 0.75$, right: $\vartheta = 0.5$.

When comparing the results in Fig. 4.24 to those in Fig. 4.22. The loss of bending stiffness becomes more apparent at the tip of the beam, which tends to “straighten” to the direction of the load.

4.4.4 Case 14: Combined load, tapered beam, no pre-curvature, elastic support

The considerations of the fourth case of combined load are summarized in (4.21). The variation of the conicity parameter ϑ and the stiffness of the support are evaluated:

$$\boxed{q = 5, \quad \alpha = 0, \quad f \in \{2.5, 5, 10\}, \quad \beta = 30^\circ, \quad 0 < \vartheta < 1, \quad A, B = 0, \quad k > 0} \quad (4.21)$$

In a similar manner as in case 2, the deformation of the beam decreases, since the torsional spring absorbs the deformation. This fact becomes once again evident by examining Figs. 4.24 and 4.25.

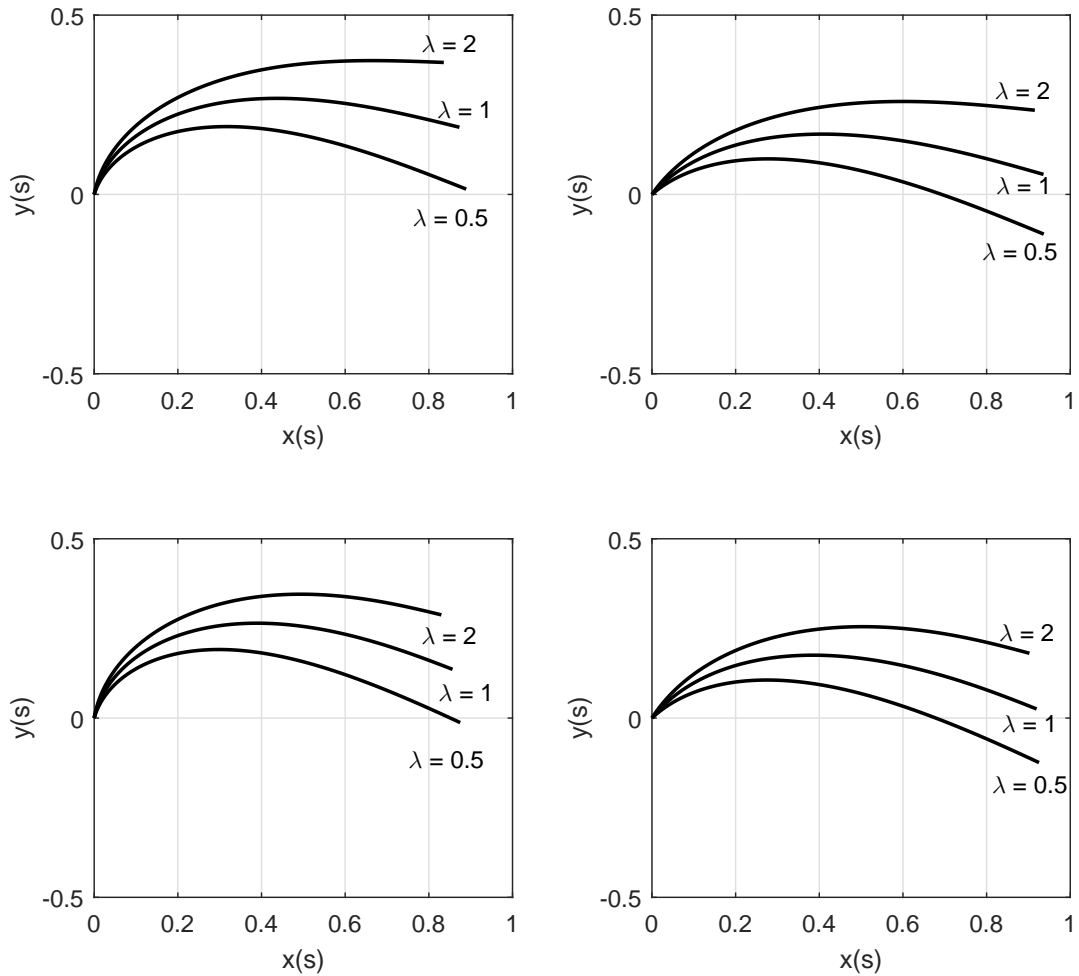


Figure 4.25: Elasticas for $q = 5$, $\alpha = 0$, $\lambda \in \{0.5, 1, 2\}$, $\beta = 30^\circ$. Top row: $\vartheta = 0.75$, bottom row: $\vartheta = 0.5$. Left column: $k = 20$, right column: $k = 5$.

4.4.5 Case 15: Combined load, uniform beam, pre-curved, rigid support

The considerations of the fifth case of combined load are summarized in (4.21). The variation of the parameters A and B are evaluated:

$$\boxed{q = 5, \quad \alpha = 0, \quad f \in \{2.5, 5, 10\}, \quad \beta = 30^\circ, \quad \vartheta = 1, \quad A, B, \quad k = +\infty} \quad (4.22)$$

Once again, a negative pre-curved helps to increase the deformation of the beam, without an increase in the internal bending moment. A positive pre-curved, however, increases the internal bending moment, since requires higher loads to achieve large deformations. Mixed pre-curveds eventually fall into one of the previous categories, depending on the values of A and B .

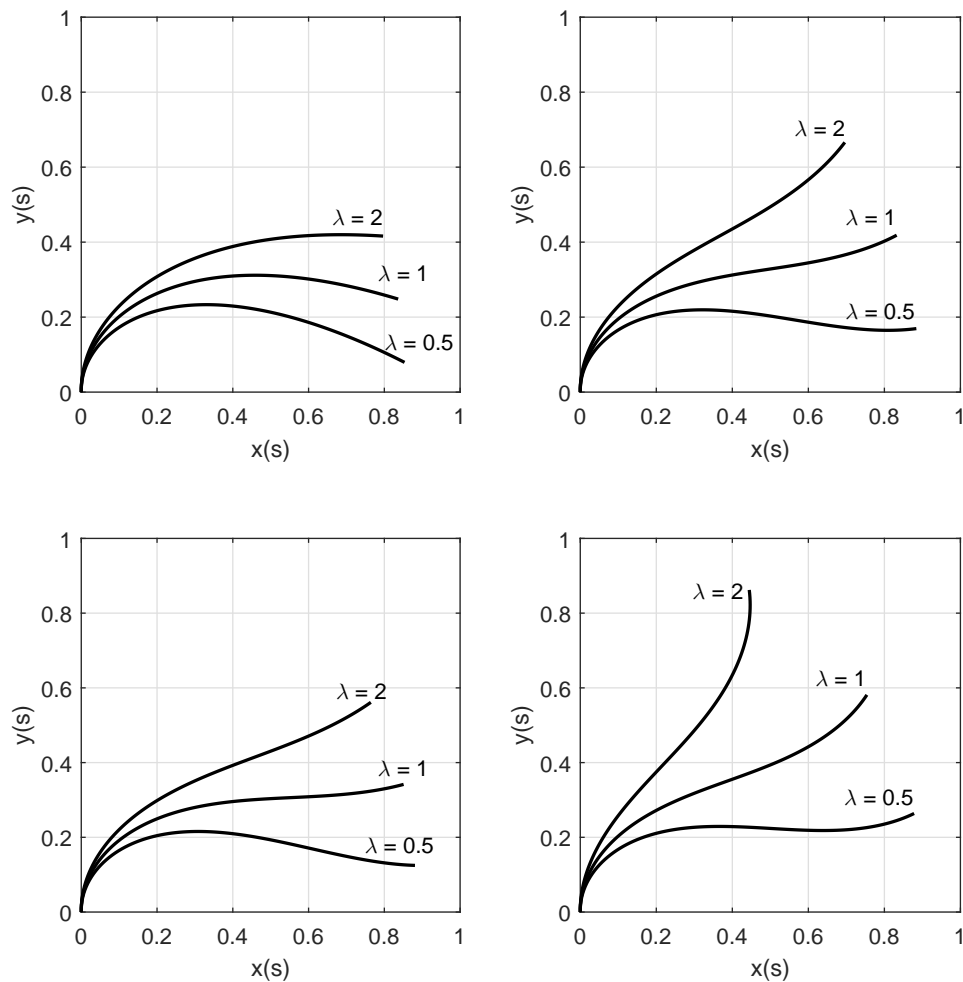


Figure 4.26: Elasticas for $q = 5$, $\alpha = 0$, $\lambda \in \{0.5, 1, 2\}$, $\beta = 30^\circ$. Top left: $A = 0$ and $B = -0.5$, top right: $A = 2$ and $B = 0$, bottom left: $A = 2$ and $B = -0.5$, bottom right: $A = 2$ and $B = 1$.

4.4.6 Case 16: Combined load, uniform beam, pre-curvature, elastic support

The considerations of the fifth case of combined load are summarized in (4.21). The variation of the parameters A and B as well as the support stiffness k are evaluated:

$$\boxed{q = 5, \quad \alpha = 0, \quad f \in \{2.5, 5, 10\}, \quad \beta = 30^\circ, \quad \vartheta = 1, \quad A, B, \quad k > 0} \quad (4.23)$$

Once again, the main change is that the spring absorbs the deformation and the beam does not bend as much as in the previous scenario. Compare the the results in the top row of Fig. 4.26 to the results in both columns in Fig. 4.27. It can be seen that the extra deformation is due to the torsional stiffness.

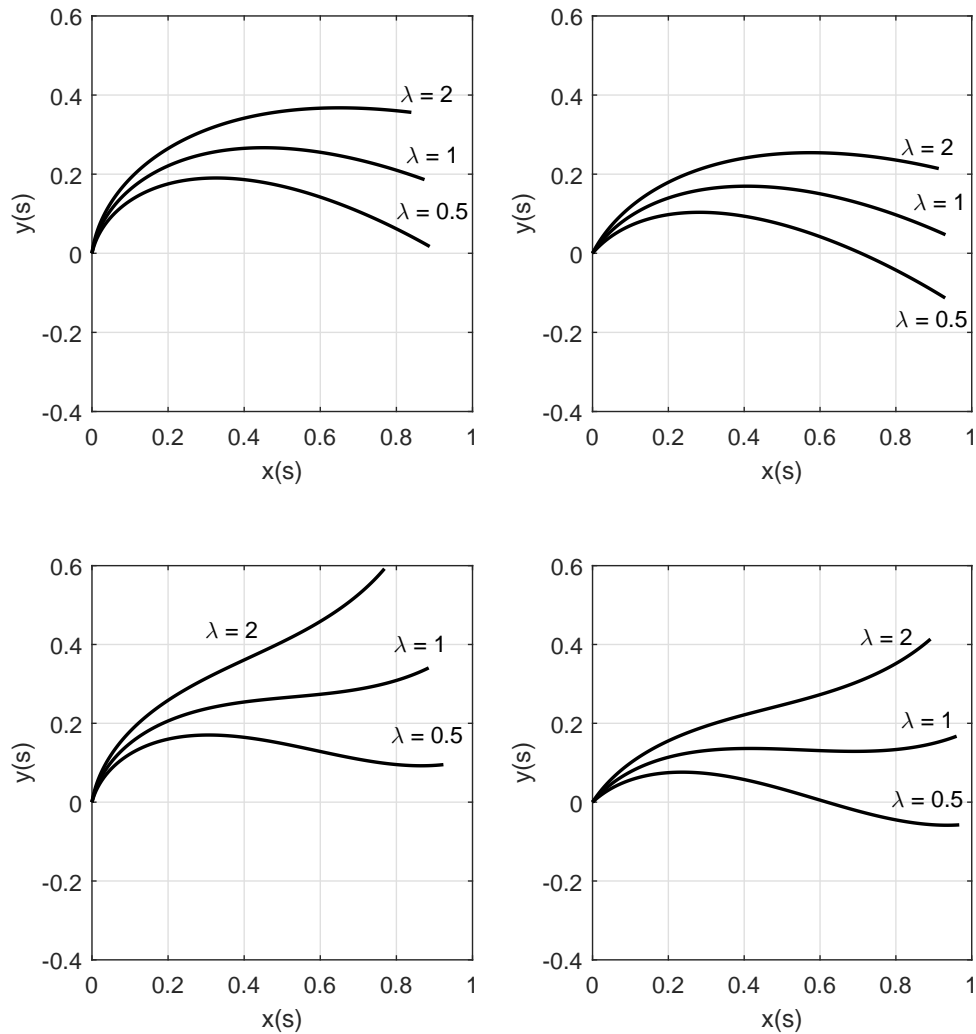


Figure 4.27: Elasticas for $q = 5$, $\alpha = 0$, $\lambda \in \{0.5, 1, 2\}$, $\beta = 30^\circ$. Top row: $A = 0$ and $B = -0.5$, bottom row: $A = 2$ and $B = 0$. Left column: $k = 20$, right column: $k = 5$.

4.4.7 Case 17: Combined load, tapered beam, pre-curvature, rigid support

The considerations of the seventh case of combined load are summarized in (4.21). The variation of the parameters A and B as well as the conicity parameter ϑ are evaluated:

$$q = 5, \quad \alpha = 0, \quad f \in \{2.5, 5, 10\}, \quad \beta = 30^\circ, \quad 0 < \vartheta < 1, \quad A, B, \quad k = +\infty \quad (4.24)$$

Regardless of the pre-curvature, it is seen in each row of Fig. 4.28 that the conicity ϑ reduces the stiffness significantly at the tip of the beam. Similarly as in the last scenario, low values of ϑ may produce divergence when searching for the result. A positive pre-curvature at the tip of the beam apparently reduces the risk of divergence, due to the fact that the positive pre-curved cases require higher loads than the negative pre-curved cases to reach similar deformations.

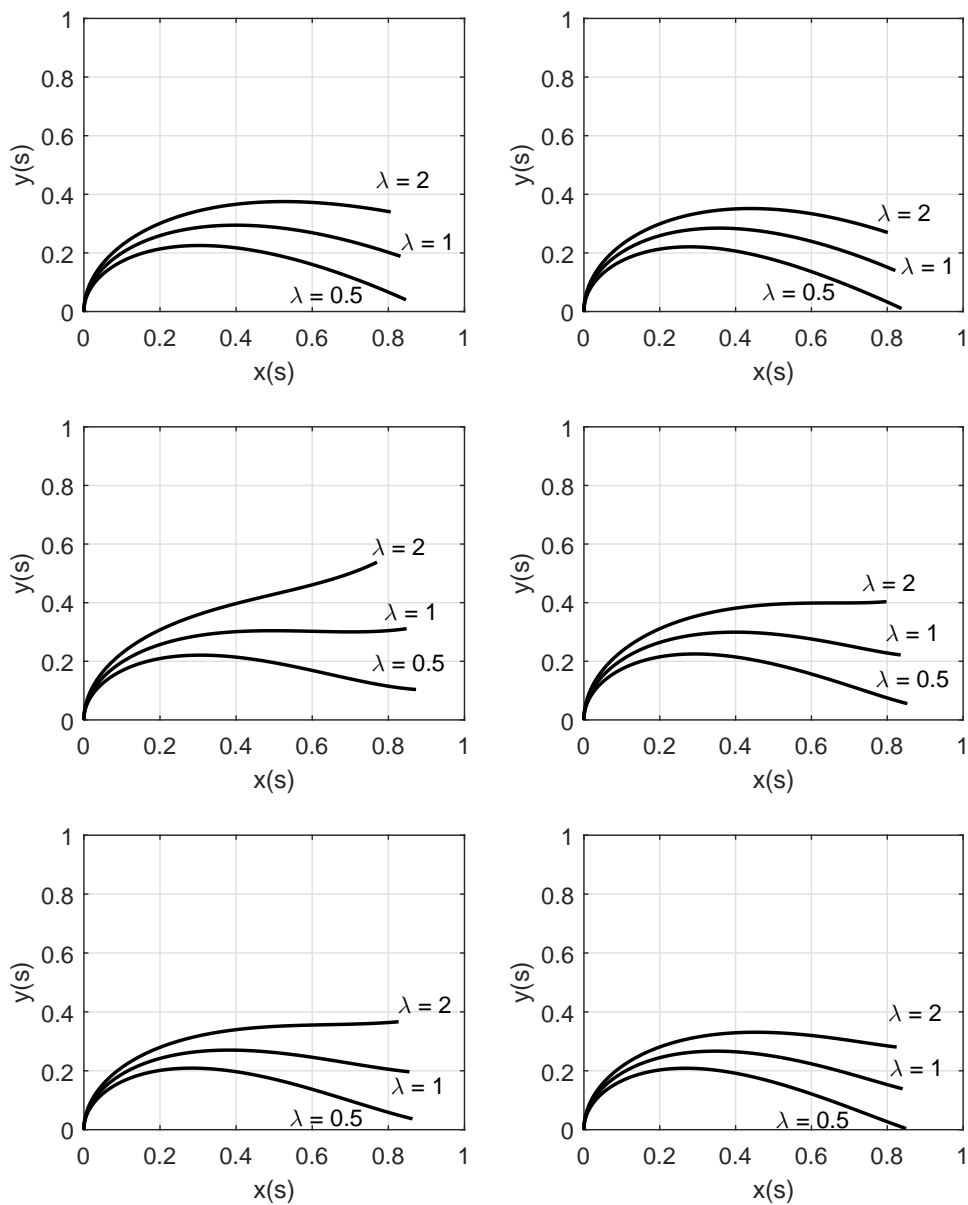


Figure 4.28: Elasticas for $q = 5$, $\alpha = 0$, $\lambda = [0.5, 1, 2]$, $\beta = 30^\circ$. Top row: $A = 0$ and $B = -0.5$, middle row: $A = 2$ and $B = 0$, bottom row: $A = 2$ and $B = -1$. Left column: $\vartheta = 0.75$, right column: $\vartheta = 0.5$.

4.4.8 Case 18: Combined load, tapered beam, pre-curvature, elastic support

Finally, the influence of the torsional spring k is also evaluated along the conicity parameter ϑ and the pre-curvature parameters A and B .

$$q = 5, \quad \alpha = 0, \quad f \in \{2.5, 5, 10\}, \quad \beta = 30^\circ, \quad 0 < \vartheta < 1, \quad A, B, \quad k > 0 \quad (4.25)$$

As in the previous cases with elastic supports, the torsional spring “absorbs” a part of the force, see Fig. 4.29. Furthermore, the combined effect of the torsional spring and the conical parameter ϑ produces a larger deformation in the beam.

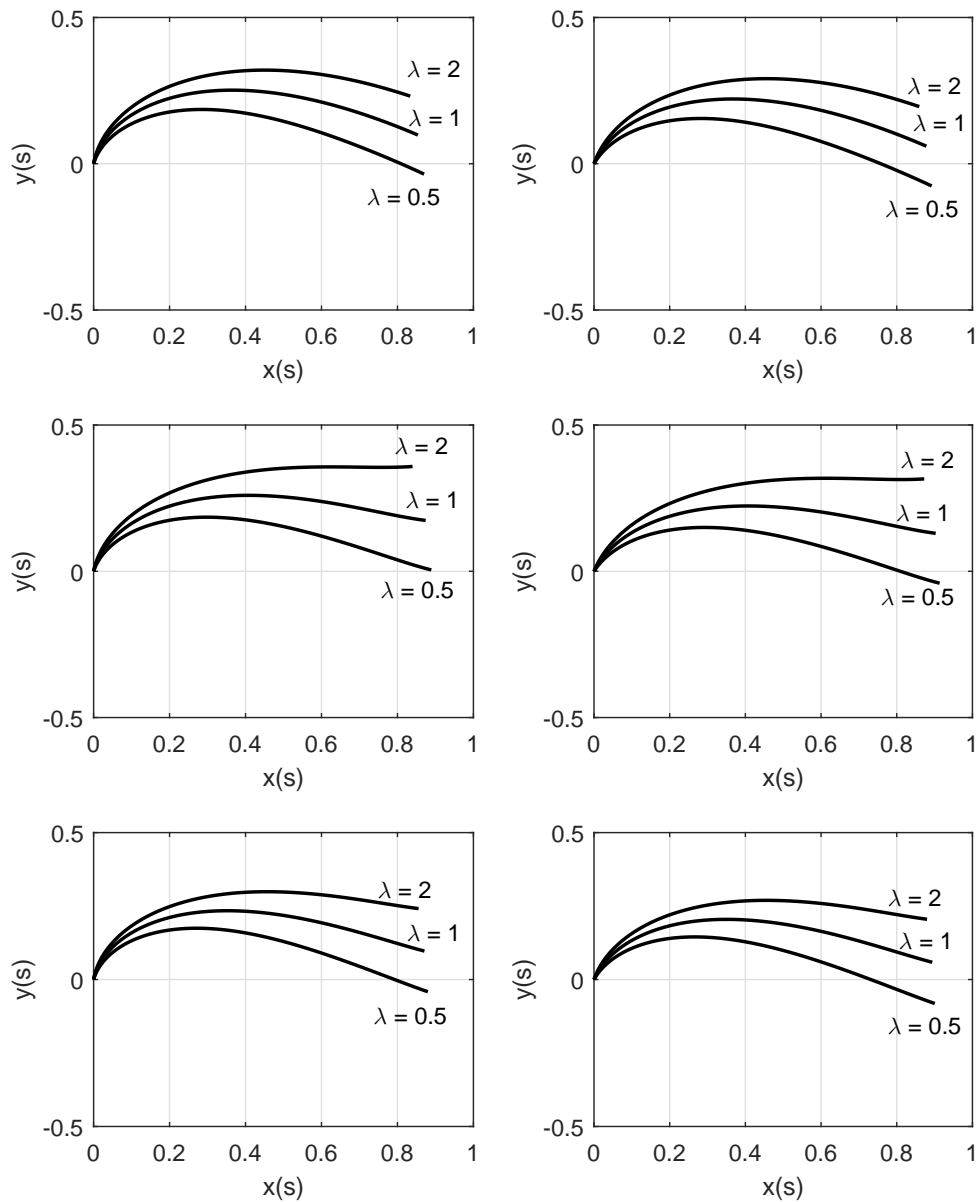


Figure 4.29: Elasticas for $q = 5$, $\alpha = 0$, $\lambda \in \{0.5, 1, 2\}$, $\beta = 30^\circ$. $\vartheta = 0.5$. Top row: $A = 0$ and $B = -0.5$, middle row: $A = 2$ and $B = 0$, bottom row: $A = 2$ and $B = -1$. Left column: $k = 20$, right column: $k = 10$.

4.5 Comparison of results with FEM-software

Similar simulations are also performed in ANSYS to compare the results obtained and guarantee that the results obtained do not deviate to those from a FEM software. Since dimensional values are needed to run a FEM simulation in ANSYS, the data from the β vibrissa, displayed in Table 2.2 are used as a reference. The value of the dimensional force is calculated with the help of f_0 (from (3.16)) and used to calculate the dimensional force for each dimensionless load.

To compare the results, the relative error (4.26) between tip coordinates is calculated for

different cases, it is done for both x and y coordinate.

$$\begin{aligned} \text{error } x_1 &:= \frac{|x_{1fem} - x_{1model}|}{x_{1fem}} \times 100\% \\ \text{error } y_1 &:= \frac{|y_{1fem} - y_{1model}|}{y_{1fem}} \times 100\% \end{aligned} \quad (4.26)$$

Table 4.2: Comparison of the tip coordinates, of the deformed β vibrissa under a concentrated force at the free end, obtained with ANSYS and the system equation.

ANSYS		Model		Error		
f	x_1	y_1	x_1	y_1	error x_1	error y_1
-	[mm]	[mm]	[mm]	[mm]	%	%
1	20.049	62.4345	19.921	62.4806	0.638	0.074
5	47.792	39.589	47.1817	40.5992	1.277	2.552
10	53.722	29.299	53.5946	29.5246	0.237	0.770
20	57.622	20.579	57.4412	20.9929	0.314	2.011
40	60.099	14.716	60.0015	14.8689	0.162	1.039

Table 4.3: Comparison of the tip coordinates, of the deformed β vibrissa under a distributed force along the shaft, obtained with ANSYS and the system equation.

ANSYS		Model		Error		
q	x_1	y_1	x_1	y_1	error x_1	error y_1
-	[mm]	[mm]	[mm]	[mm]	%	%
1	8.191	65.61814	8.1629	65.6214	0.337	0.005
5	33.389	55.667	32.7863	56.0642	1.805	0.714
10	46.77	42.912	46.2956	43.4841	1.014	1.331
20	54.976	29.372	54.8735	29.5255	0.186	0.523
40	59.236	18.742	59.1591	18.8305	0.130	0.472

It can be seen in Tables 4.2 and 4.3 that the results obtained through both methods differ in less than 1% in most of the cases (2.55% is the greatest difference). The difference is small enough to be ignored. The magnitude of the error indicates that the model accurately obtains the elastica for large deflections in a beam using the non-linear Euler-Bernoulli beam theory. Note that the FEM already carries an error term, however, it serves to establish reference values.

4.6 Influence of each parameter

Influence of the torsional spring at the base: this parameter proves to have the largest influence on the model. When reducing the stiffness of the spring, the rotation increases and the deformation of the beam is largely reduced (for cases $k < 5$). With even lower values of k , a rotation very similar to rigid body motion is observed. Large values of k (> 20) approximate the results for a rigid support.

Influence of the pre-curvature: the main influence of this parameter is the “overall orientation” of the pre-curvature. For cases where the curvature is negative or in the “same direction” as the load, large deflections are achieved without much strain on the

beam itself. For cases where the curvature is positive or in the “opposite direction” of the load, deflections are not as large and require higher loads to achieve equivalent deflections and thus higher strain. For cases of mixed positive and negative curvature, the behavior typically follows one of the former scenarios, the exact behavior depends on A and B .

Influence of conicity: the bending stiffness of the beam itself is reduced with decreasing values of ϑ . This is more evident at the tip of the beam. When decreasing ϑ , the tip of the beam tends to straighten to the direction of the load applied. Due to the reduced stiffness, convergence problems are encountered for low ϑ values, since the results become increasingly dependent on the starting values for each iteration.

4.7 Summary and comments

- Different cases are studied, taking into account various combinations of characteristics found in vibrissae and their variation.
- A general model that takes into account all characteristics and considerations (distributed load, conicity, pre-curvature, elastic support) is obtained and represented in a non-linear differential equation (3.25) with the boundary conditions described in (3.21) and (3.22). This differential equation is dimensionless and depends on various parameters: force parameter q , conicity parameter ϑ , pre-curvature parameters A and B , and torsional spring parameter k .
- MATLAB function `fzero` is widely used to find an appropriate starting value for each calculation, a custom *bisection method* solver can also be applied. It was, in fact, used during the first simulations. However, for the elastic support cases, where $\varphi(0)$ and $\varphi(1)$ are searched, the function `fsolve` (`fzero` equivalent for system of non-linear equations) is not suitable to find the solution, due to the fact that $\varphi(0)$ converges considerably faster than $\varphi(1)$, and therefore a suitable result cannot be achieved.

Chapter 5

Obstacle contour contact under the influence of a fluid flow

In the previous chapters, a mechanical model of a vibrissa, shown in Fig. 3.1, and the mathematical model with the differential equation of the system (3.25) are developed. In this chapter, the resulting mechanical model is used in order to determine and obtain the fluid loads from information at the base of the vibrissa as well as to identify and reconstruct the contour of an obstacle. The information at the base or observable quantities are: the support reaction forces A_x , A_y , reaction moment M_A , the deflection angle φ_0 at the base and the position x_0 of the support.

5.1 Considerations for obstacle/fluid flow detection

5.1.1 General considerations

The following assumptions are taken into account for contour and fluid flow detection:

- In the case of passive whisking at low speed, a quasi-static analysis is admissible.
- The obstacle object is considered to be rigid and remains in a fixed position. Its contour is defined with a function g , which is strictly convex. The coordinates of a given point of the profile are given by the coordinates x_{cont} , y_{cont} , and the angle ψ_{cont} (measured from the x - to the y -axis).
- The movement and all vibrissa deformations are restricted to the $x - y$ -plane. The base of the whisker moves along the x -axis from the right to the left, its position on the x -axis is called x_0 from now on, and it is expressed in a global coordinate system.
- The vibrissa can show all the characteristics explored in the previous chapters: conicity, pre-curvature, elastic support. The vibrissa material is assumed to be linear elastic and the internal stress and strain never reach the yield point of the material.
- The analysis of contact is also dimensionless, therefore, the dimensionless parameters for a dimensionless vibrissa from Chapter 3 are used. The vibrissa is assumed to have a length 1.
- The contact between the object and the vibrissa is assumed to be ideal and frictionless, therefore the contact force is always perpendicular to the contour tangent. Moreover, there is only one contact point between the vibrissa and the obstacle.

5.1.2 Considerations for the fluid flow

Certain assumptions for the fluid flow and resulting load are taken into account:

- The load produced by the fluid flow is regarded as an uniformly distributed load q (dimensionless) that spans from the base of the vibrissa to the contact point ¹.
- When passing through the reduced section (produced by the contour and the x -axis), the velocity of the flow increases according to the Venturi effect, this effect is ignored.
- The analysis considers that the vibrissa base moves slowly along the x -axis, thus a quasi-static analysis is possible.
- The influence of the characteristics of vibrissae are studied (conicity, pre-curvedure) for both rigid and elastic supports.

5.2 General scenario for obstacle/fluid flow detection

A general scenario for fluid flow detection is displayed in Fig. 5.1.

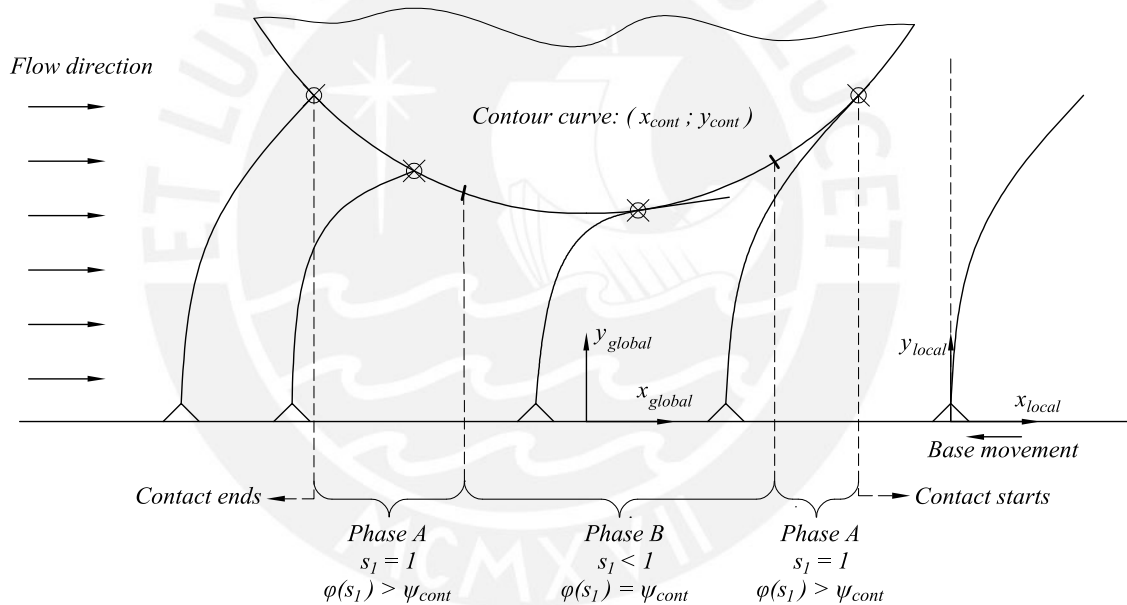


Figure 5.1: General scenario for obstacle contour contact under fluid loads.

Various scenarios are identified as the base moves along the x -axis:

1. vibrissa under the sole influence of the fluid flow,
2. vibrissa contact with the obstacle, it can be either tip or tangential contact,
3. vibrissa separation with the obstacle.

5.2.1 Vibrissa only under the influence of the fluid load

During this scenario, the vibrissa is yet to come into contact with the obstacle and is only under the influence of a given fluid load q . Therefore, it can be considered as a beam only under an horizontal distributed load q ($\alpha = 0$). By applying the model and the system (3.25), two important results are found:

¹This is an approximation. To obtain the real distribution, experimental results and/or computational fluid dynamics (CFD) simulations are required.

- Coordinates of the tip of the vibrissa x_1 and y_1 , as well of the deflection angle at the tip φ_t .
- Base reactions A_x , A_y and M_A as well as the deflection angle at the base φ_0 , which are measured by the sensor at the base. The force equilibrium for this case yields:

$$\begin{aligned} \Sigma F_x = 0 : \quad A_x &= -q \cdot (s_1 - 0) \\ \Sigma F_y = 0 : \quad A_y &= 0 \end{aligned} \quad (5.1)$$

Furthermore, it is found that a relationship between M_A and φ_0 and it depends on the torsional stiffness of the support, as evidenced in Fig. 5.2.

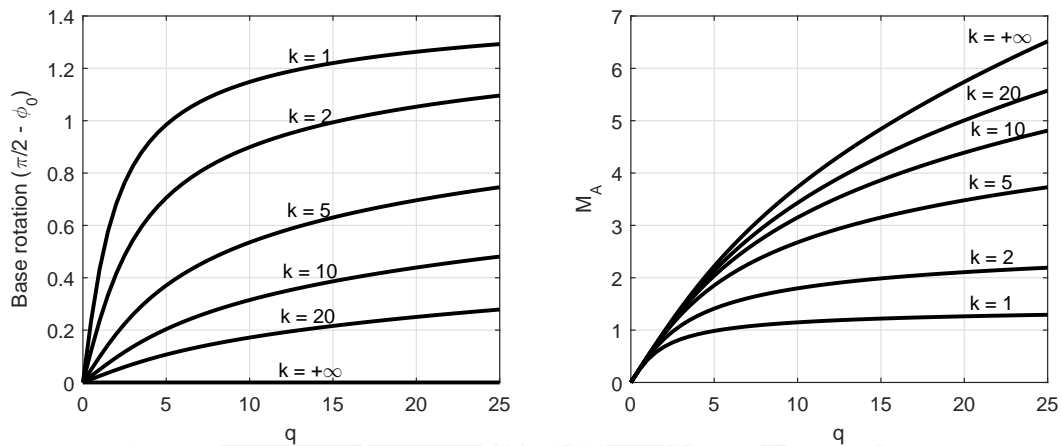


Figure 5.2: Relationship between the rotation at the base ($\pi/2 - \varphi$) and base moment M_A vs. the force parameter.

Using the results y_1 and φ_1 , the initial contact point between the obstacle and the vibrissa can be established. First, the highest point of the vibrissa y_1 is picked and a point belonging to the contour curve g is sought, such that $y_{cont} = y_1$. Next, φ_1 is compared to ψ_{cont} . If φ_1 is larger than ψ_{cont} , then the first contact point is the tip of the vibrissa (tip contact). If φ_1 is smaller than ψ_{cont} , then the contact point is located at an arc-length coordinate $s < 1$, and the contact point is a common tangent point for both the elastica and the contour curve. The contact point then fulfills the condition: $y_{elastica} = y_{cont}$ and $\varphi_{elastica} = \psi_{cont}$. The observable quantities of this scenario serve to obtain the fluid flow load q .

5.2.2 Vibrissa contact with the obstacle

During the contact scenario, for each point in the contour curve the corresponding observables at the base are calculated using the model developed in the previous chapters. The observables are used later to reconstruct the profile and obtain the value of the fluid load. Also, during the obstacle contact scenario, two kinds of contact are possible depending on the location of the contact point. These possibilities are identified as two phases, similar to the work of [Steigenberger 2013], [Will et al. 2014a], [Will et al. 2014b] and [Will et al. 2015]:

Phase A: Tip contact

During this phase, the contact point is located at the tip of the vibrissa, $s_1 = 1$. The deflection angle at the tip φ_1 and the contact force f are unknown. An additional condition

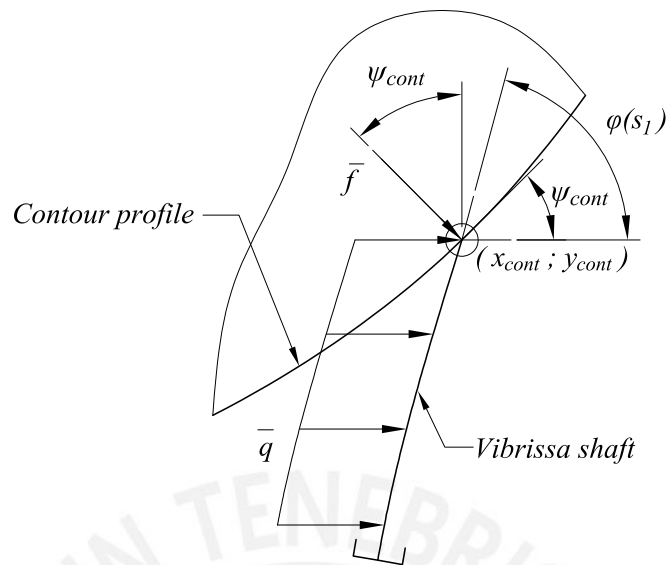


Figure 5.3: Sketch for the tip contact phase.

is that φ_1 must be larger than ψ_{cont} as shown in Fig. 5.3. If during calculation $\varphi_1 < \psi_{cont}$, then the contact phase must switch from A to B. The input data for this phase are the (x_{cont}, y_{cont}) coordinates of the g curve, as well as the slope angle ψ_{cont} at said point, additional input variables are the contact force f and φ_1 calculated in the previous step, as they act as starting points for the calculation for the new values f and φ_1 .

Phase B: Tangential contact

During this phase, the contact point is located somewhere between the base and the tip, $0 < s_1 < 1$, and this point is a common tangential point for both the contour and the elastica, therefore $\varphi_1 = \psi_{cont}$. Unlike phase A, during this phase s_1 must be determined alongside f . If during calculation $s_1 = 1$, the contact phase must switch back from B to A.

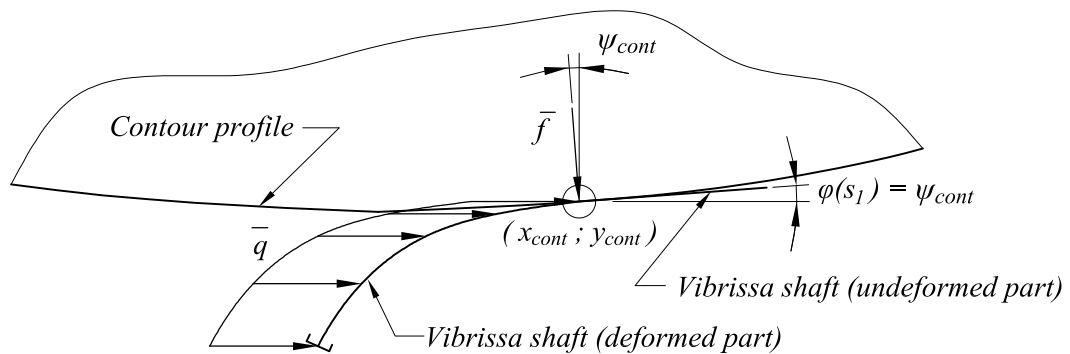


Figure 5.4: Sketch for the tangential contact phase.

5.2.3 Vibrissa separation from the obstacle

Regardless of the flow intensity or the contour profile function, the tip of the vibrissa is the last contact point during the whole contact phase ². The last contact scenario happens when one of the following conditions are met:

Separation condition 1

If x_0 is larger than any x_0 calculated in previous steps – in other terms the pointwise calculated x_0 function shows a local minimum, then a contradiction occurs. Since the movement of the drive of the sensor moves always to the left side (negative side of the x -axis), there cannot be local minimum.

This condition leads to a sudden increase in the contact force before the separation. This fact represents an increase of the deformation energy moments before the separation, which leads to a sudden “snap”. However, when applying fluid loads the sudden separation condition is not always met. Therefore, an additional condition is needed.

Separation condition 2

In case the fluid load is too strong, the separation occurs slowly with the contact force decreasing to zero as the vibrissa drive moves away from the obstacle. If this condition is met, no “snap” occurs. Note that this condition does not always occur and only one of the described scenarios takes place, not both at the same time. This scenario may occur during phase A or B.

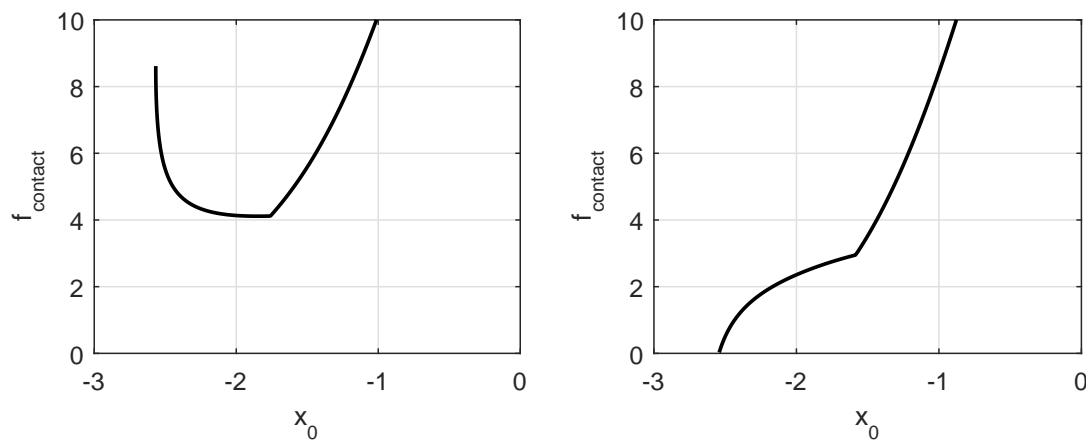


Figure 5.5: Left: Separation condition 1; notice the sudden increase of the contact force before separation, a “snap” occurs at the last instant. Right: Separation condition 2; notice the decrease of the contact force before separation, no “snap” occurs. Note that the base moves from the right to the left.

5.3 Obstacle contour contact

The contour of the object to be identified is defined with a function g . Using the conditions described in the previous section, the following algorithm can be implemented (see Fig. 5.6).

²Scenarios where the last contact phase is actually a tangential contact are also plausible, however they require a further analysis of the behavior of the fluid load, since this scenario occurs with highly negative values of pre-curvature.

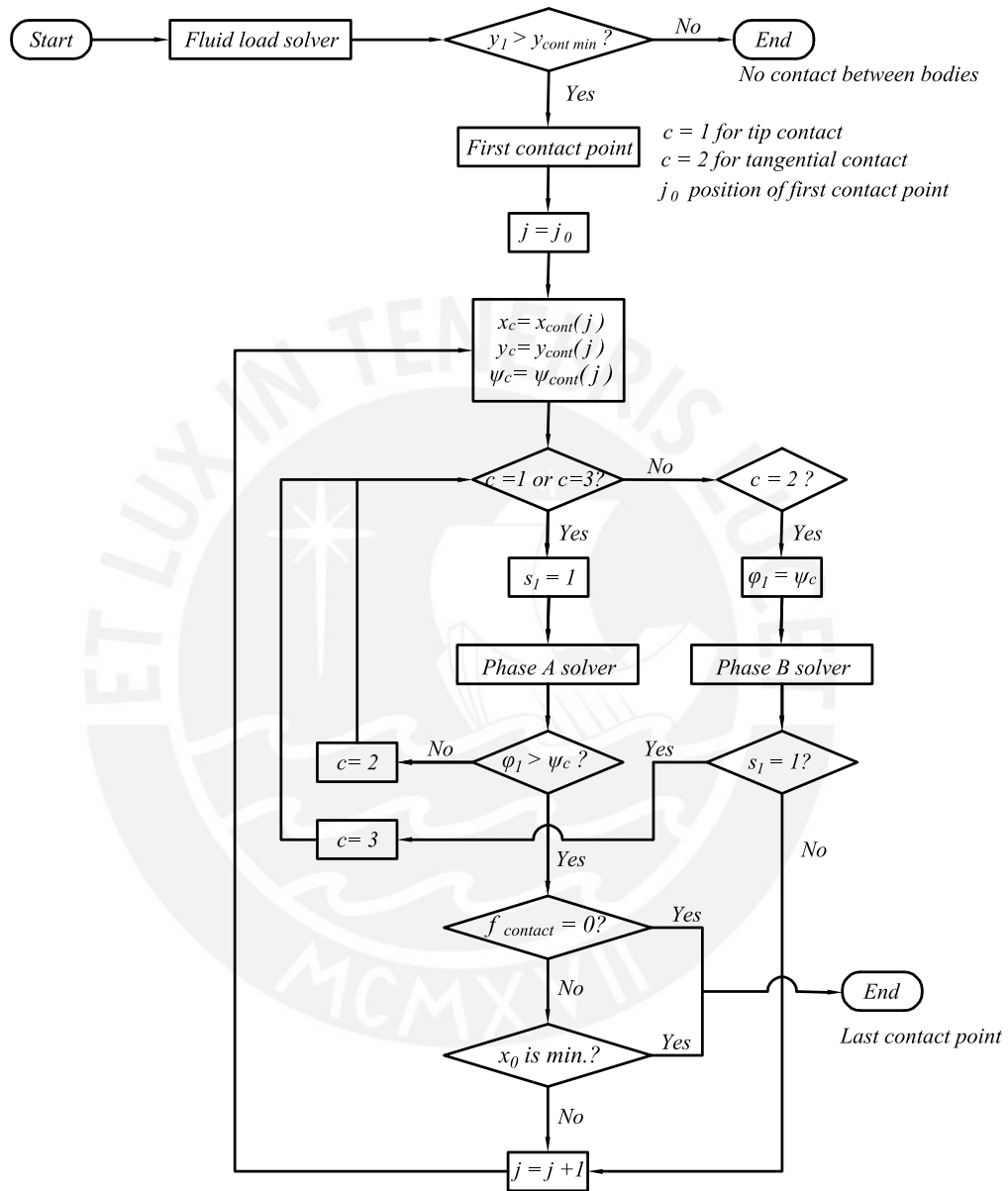


Figure 5.6: Block diagram for the algorithm used for contact between a vibrissa and an obstacle contour.

The determination of the first contact point (tangentially initial contact) is performed with the algorithm found in [Schwarz 2005]. Each solver (tip and tangential) in Fig. 5.6 is written using MATLAB's function `fsolve`, with a maximum number of iterations of 1500

and a maximum number of function evaluations of 800. It was found that, for some cases, the default number of function evaluations is not enough to reach a solution. The tolerance used is 10^{-6} . The algorithm used is the default *trust-region-dogleg* algorithm, which improves robustness and handles better when the initial values are far from the solution³.

In order to set reference values for the simulations and evaluate the influence of the vibrissa characteristics in the results and measured values, the sweep of a catenary profile and a parabolic profile (also evaluated in [Will et al. 2014a], [Will et al. 2014b], [Will et al. 2015]) are simulated. The catenary can be described by (5.2) and the parabola is described by (5.3)

$$g_1 : \quad y_{cont}(x_{cont}) = \cosh\left(\frac{1}{2}x_{cont}\right) - \frac{4}{5} \quad (5.2)$$

$$g_2 : \quad y_{cont}(x_{cont}) = \frac{1}{2} + \frac{1}{2}x_{cont}^2 \quad (5.3)$$

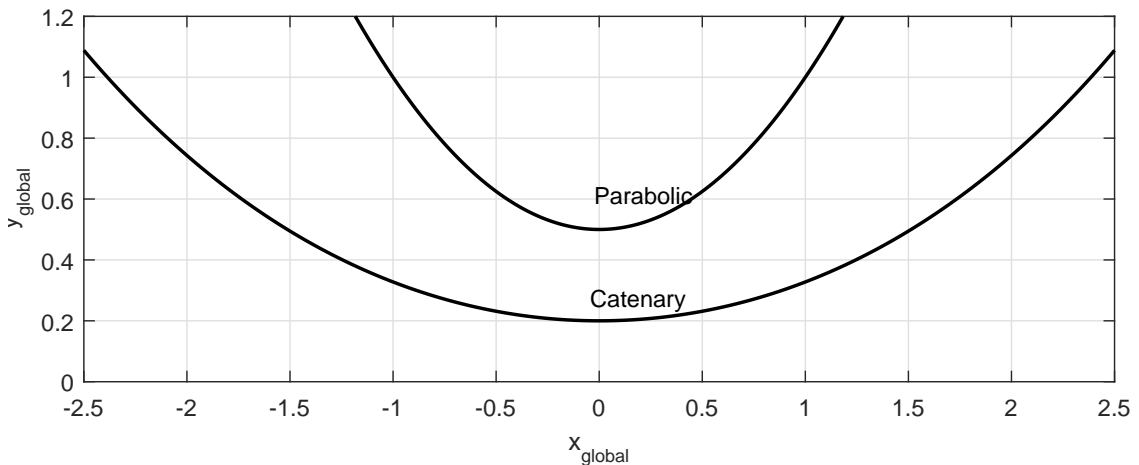


Figure 5.7: Contour profile of the catenary and parabolic curves, (5.2) and (5.3).

Different cases of contact are simulated and studied to analyze the behavior of the vibrissa sensor. During every simulation, the observable quantities are measured and stored. Moreover, the contact force and s_1 are also plotted.

5.3.1 Case 1: Contact considering different fluid loads

The first case considers a cylindrical vibrissa with no pre-curvature and rigid support.

$$g_1, g_2, \quad q \in \{0, 1, 5, 10\}, \quad \vartheta = 1, \quad A, B = 0, \quad k = +\infty \quad (5.4)$$

The obtained observables for the different fluid loads are displayed in Figs. 5.9 and 5.10 and the calculated s_1 and contact force in Fig. 5.11.

It can be seen in Figs. 5.11 and 5.14 that the separation condition changes from a “snap” to a slow separation, since there is no sudden increase in the contact force at the last contact point. This fact is due to the intensity of the fluid load, as the fluid “absorbs” the energy of snap.

It can also be seen that the higher the fluid flow load, the more the initial contact is “delayed”. The magnitude of the delay depends on how far the obstacle is from the

³More detailed information at:

<https://de.mathworks.com/help/optim/ug/equation-solving-algorithms.html#f51887>.

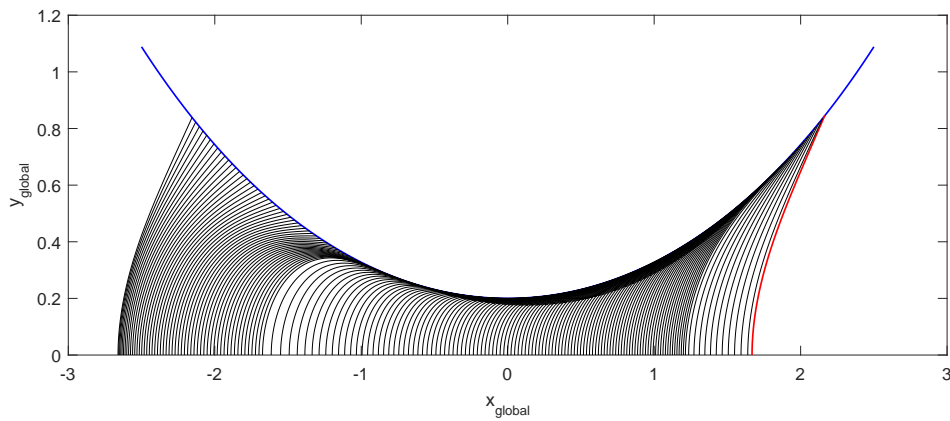


Figure 5.8: Case study 1 (catenary): Contact between a catenary profile and a cylindrical, rigidly supported vibrissa under a fluid load of $q = 5$. Notice the different contact phases.

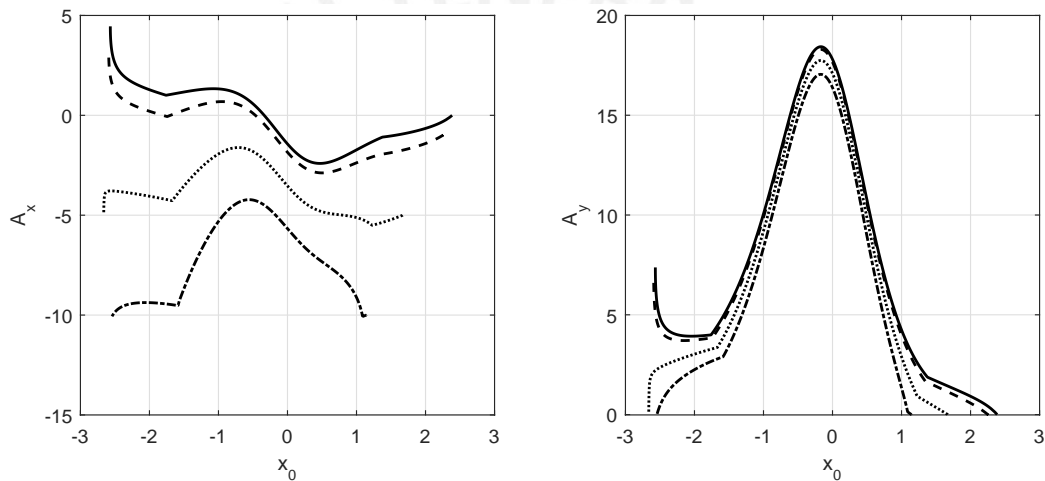


Figure 5.9: Case 1 (catenary): Observable reaction forces in x and y direction. Continuous line: $q = 0$, dashed line: $q = 1$, dotted line: $q = 5$, dashed-dotted line: $q = 10$.

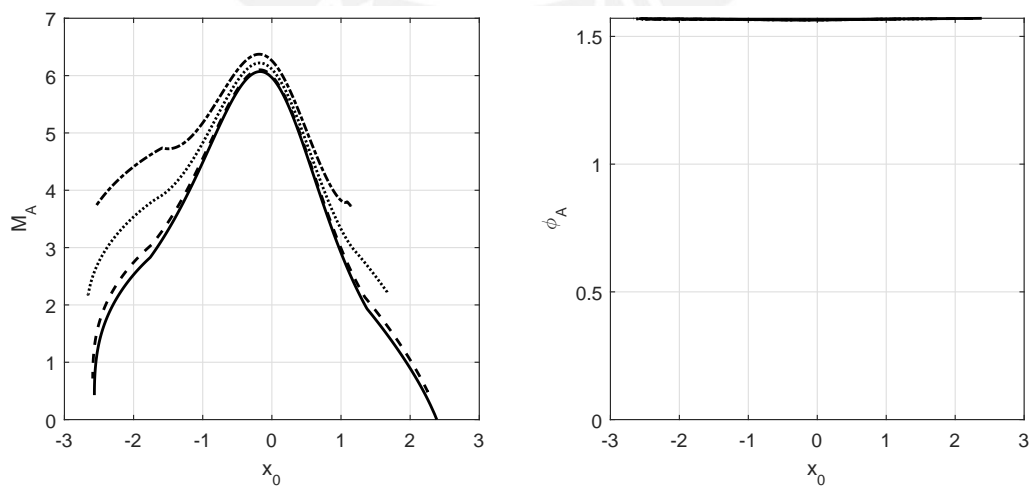


Figure 5.10: Case 1 (catenary): Observable Moment reaction and base angle. Continuous line: $q = 0$, dashed line: $q = 1$, dotted line: $q = 5$, dashed-dotted line: $q = 10$.

vibrissa base and the magnitude of the distributed load. The last contact point does not

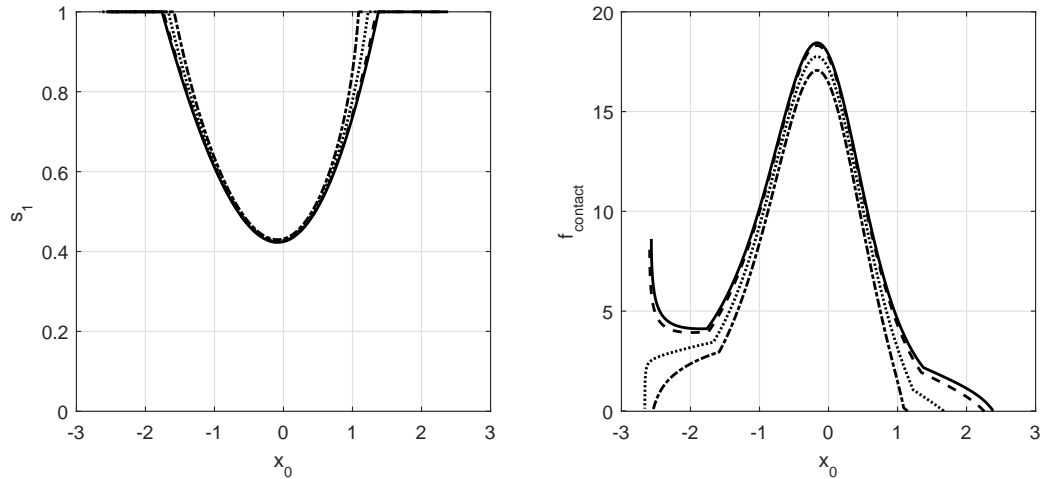


Figure 5.11: Case 1 (catenary): Length s_1 and contact force. Continuous line: $q = 0$, dashed line: $q = 1$, dotted line: $q = 5$, dashed-dotted line: $q = 10$.

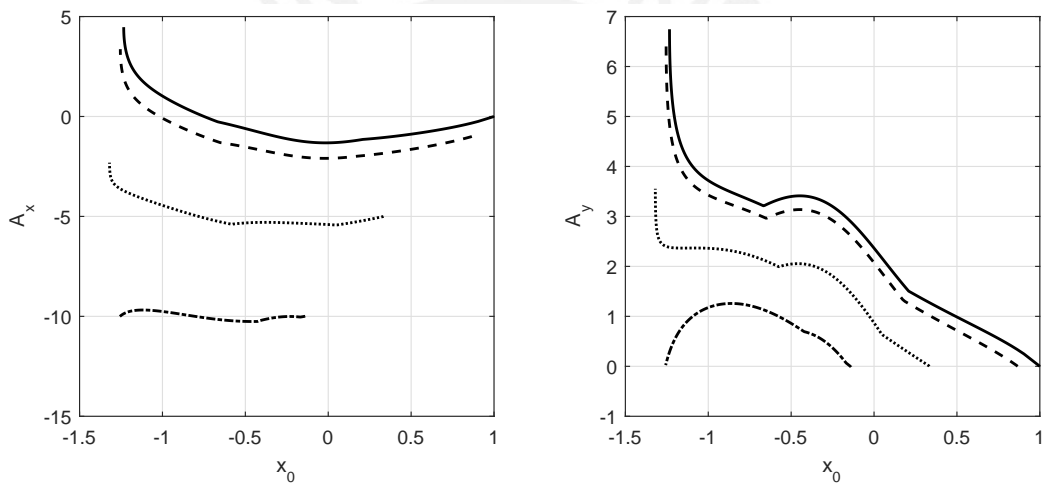


Figure 5.12: Case 1 (parabolic): Observable reaction forces in x and y direction. Continuous line: $q = 0$, dashed line: $q = 1$, dotted line: $q = 5$, dashed-dotted line: $q = 10$.

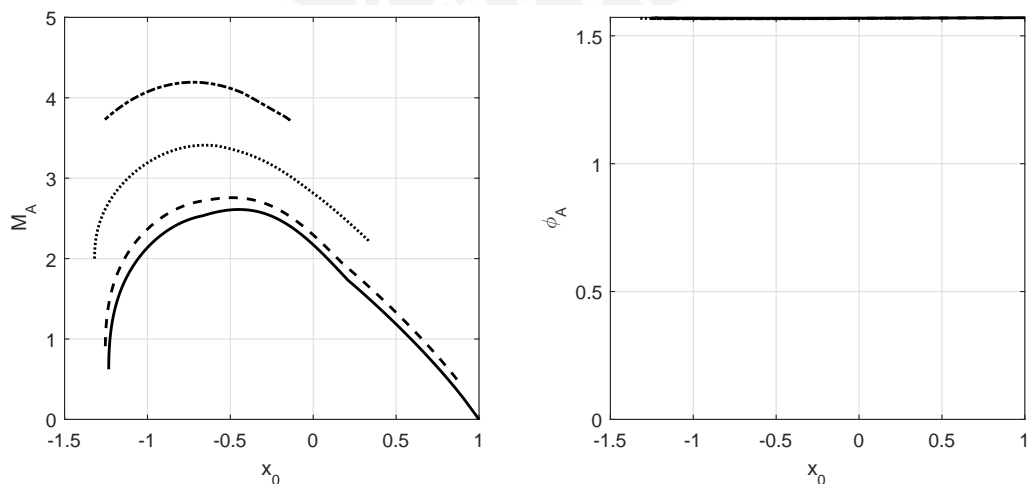


Figure 5.13: Case 1 (parabolic): Observable Moment reaction and base angle. Continuous line: $q = 0$, dashed line: $q = 1$, dotted line: $q = 5$, dashed-dotted line: $q = 10$.

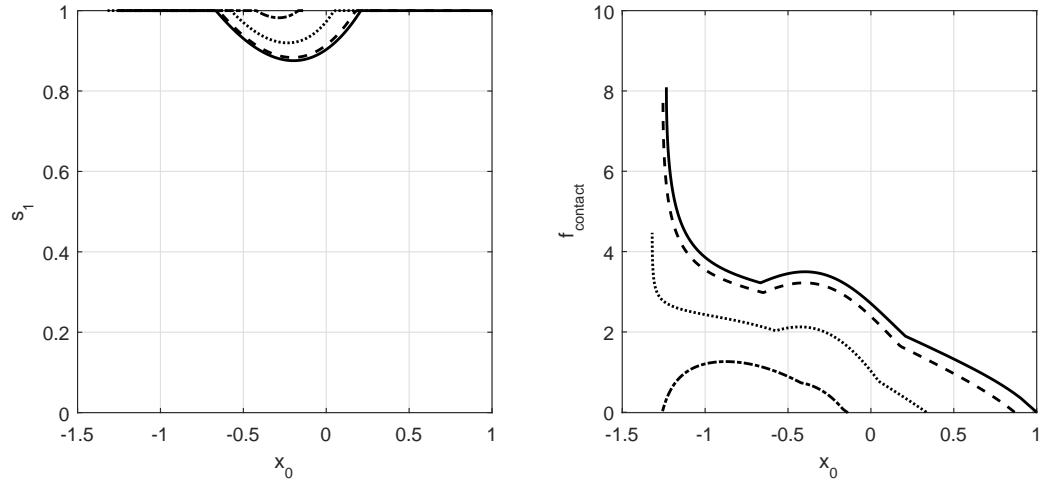


Figure 5.14: Case 1 (parabolic): Length s_1 and contact force. Continuous line: $q = 0$, dashed line: $q = 1$, dotted line: $q = 5$, dashed-dotted line: $q = 10$.

vary largely, regardless of the last contact scenario (see Figs. 5.11 and 5.14.)

It can also be seen that when the farther the obstacle, the less contact points that are measured. This is specially the case in the parabolic obstacle, Figs. 5.12 and 5.14, with a large fluid flow load.

5.3.2 Case 2: Contact considering different conicity parameters

The second case considers a conical vibrissa with no pre-curvature and a rigid support. Each case contains a simulation of a cylindrical vibrissa (continuous line) for comparison.

$$g_1, g_2, \quad q = 5, \quad \vartheta \in \{1, 0.75, 0.5, 0.25\}, \quad A, B = 0, \quad k = +\infty \quad (5.5)$$

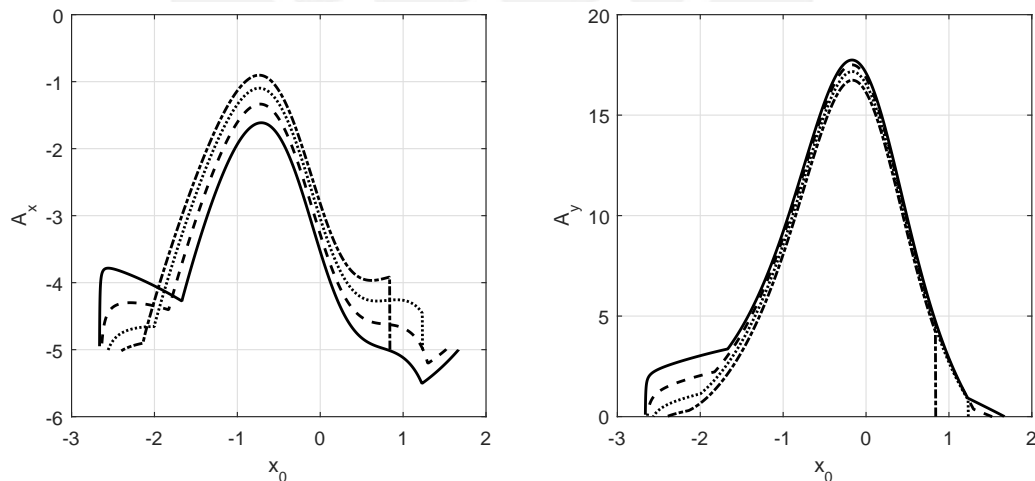


Figure 5.15: Case 2 (catenary): Observable reaction forces in x and y direction. Continuous line: $\vartheta = 1$, dashed line: $\vartheta = 0.75$, dotted line: $\vartheta = 0.5$, dashed-dotted line: $\vartheta = 0.25$.

When comparing the results obtained with vibrissae with different conicity parameters ϑ , it can be seen that there is a reduction in the magnitude of the horizontal force, however, the vertical force does not suffer this decrease, as seen in Figs. 5.15 and 5.18.

A “delay” of the initial contact also occurs, and similarly as the last scenario, the lower

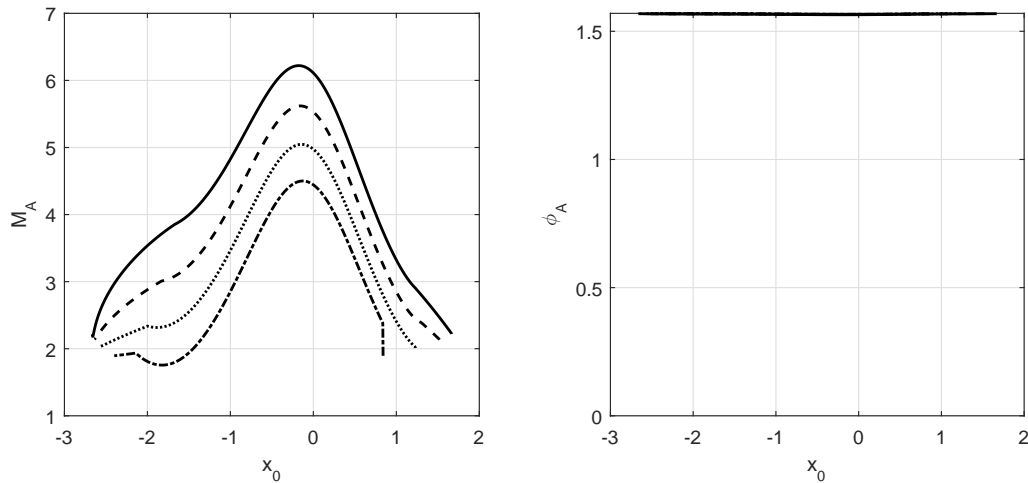


Figure 5.16: Case 2 (catenary): Observable moment reaction and base angle. Continuous line: $\vartheta = 1$, dashed line: $\vartheta = 0.75$, dotted line: $\vartheta = 0.5$, dashed-dotted line: $\vartheta = 0.25$.

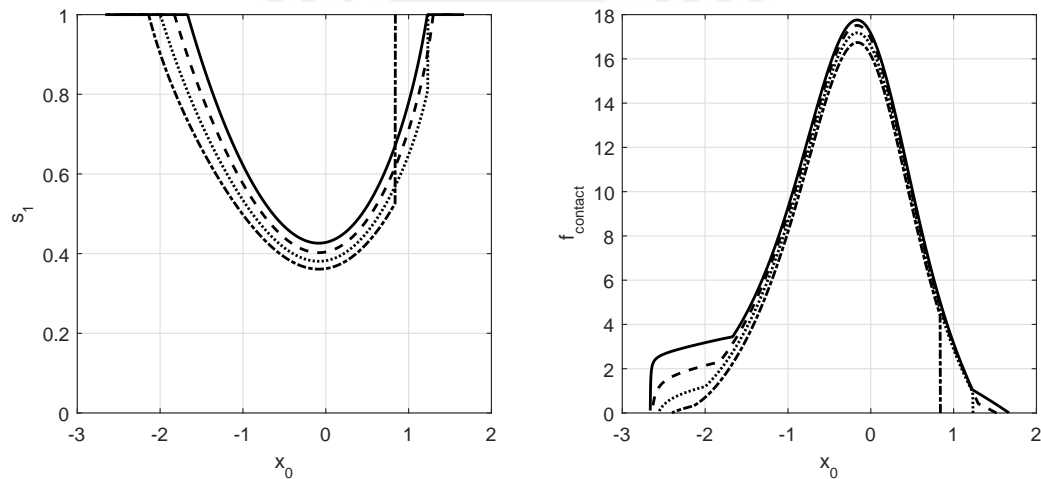


Figure 5.17: Case 2 (catenary): Length s_1 and contact force. Continuous line: $\vartheta = 1$, dashed line: $\vartheta = 0.75$, dotted line: $\vartheta = 0.5$, dashed-dotted line: $\vartheta = 0.25$.

the ϑ parameter, the larger the “delay”.

Due to the lower bending stiffness, the moment measured at the base decreases with low values of ϑ (see Fig. 5.16). However, the contact force does not largely vary as it can be seen in Fig. 5.17.

It is worth noticing that with low conicity parameters (or with high fluid flow forces), the initial contact is no longer Phase A (tip contact), but tangential contact (Phase B). Therefore, the distributed force does not act on the whole length of the vibrissa. This change is represented as a sudden increase in the horizontal force observed at the base (see Figs. 5.15 and 5.18) or in the sudden apparition of a contact force as seen in Figs. 5.17 and 5.20.

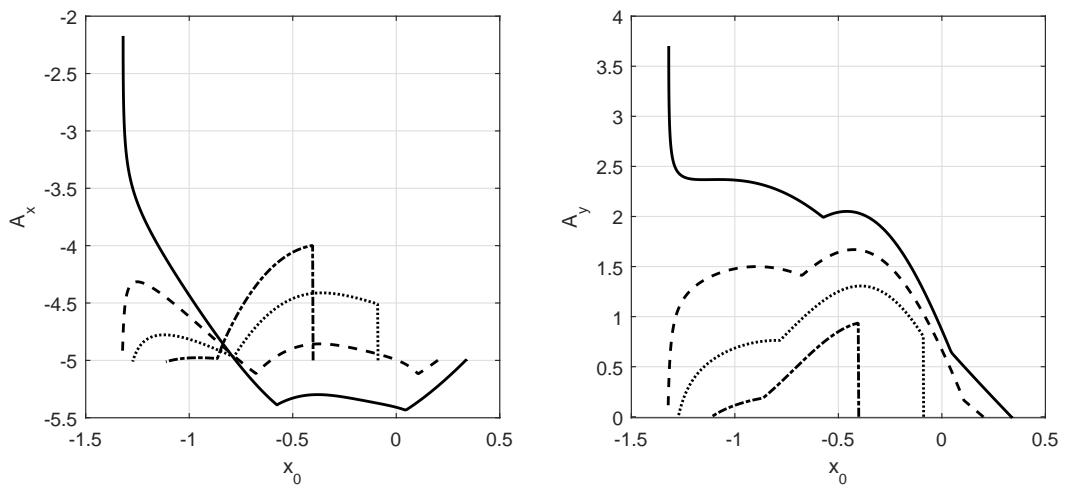


Figure 5.18: Case 2 (parabolic): Observable reaction forces in x and y direction. Continuous line: $\vartheta = 1$, dashed line: $\vartheta = 0.75$, dotted line: $\vartheta = 0.5$, dashed-dotted line: $\vartheta = 0.25$.

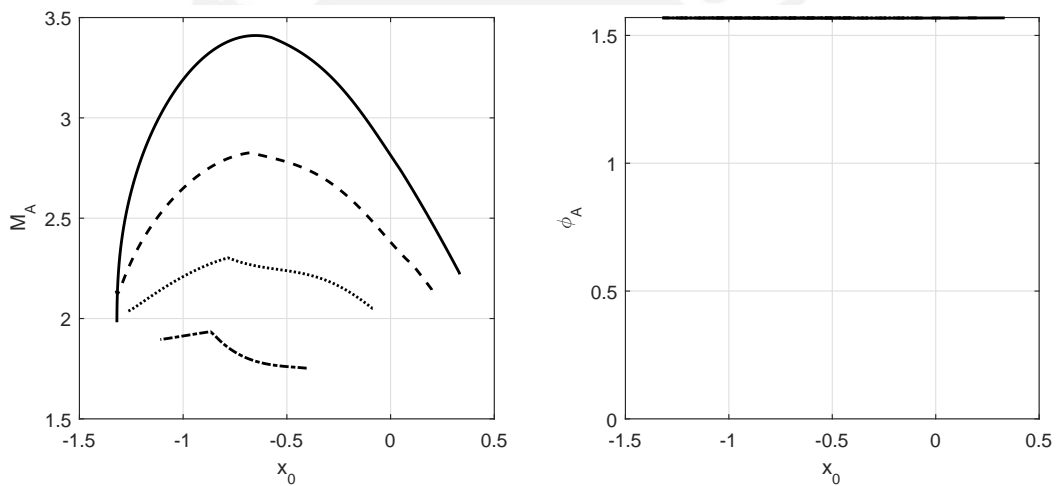


Figure 5.19: Case 2 (parabolic): Observable moment reaction and base angle. Continuous line: $\vartheta = 1$, dashed line: $\vartheta = 0.75$, dotted line: $\vartheta = 0.5$, dashed-dotted line: $\vartheta = 0.25$.

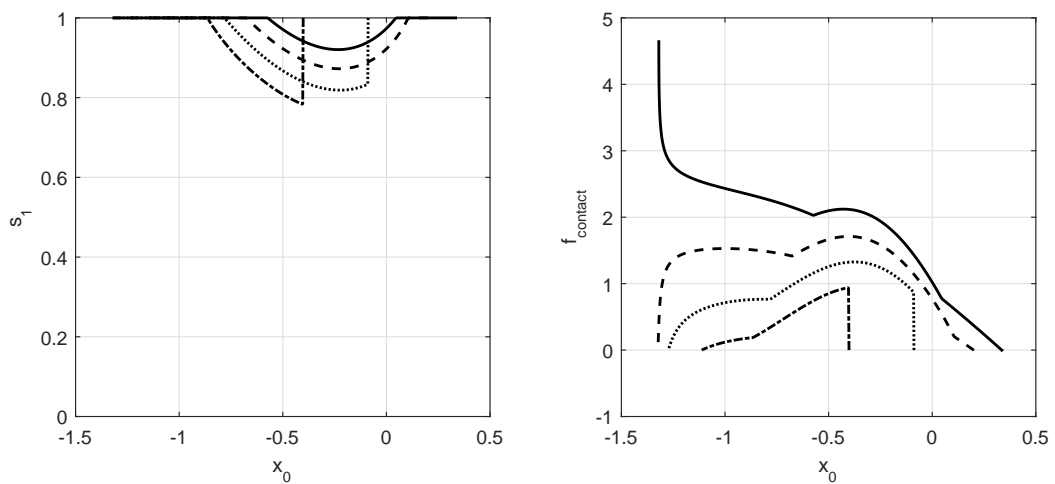


Figure 5.20: Case 2 (parabolic): Length s_1 and contact force. Continuous line: $\vartheta = 1$, dashed line: $\vartheta = 0.75$, dotted line: $\vartheta = 0.5$, dashed-dotted line: $\vartheta = 0.25$.

5.3.3 Case 3: Contact considering different torsional stiffness at the base

The third case considers a cylindrical beam with an elastic support at the base:

$$g_1, g_2, \quad q = 5, \quad \vartheta = 1, \quad A, B = 0, \quad k \in \{5, 10, 20, +\infty\} \quad (5.6)$$

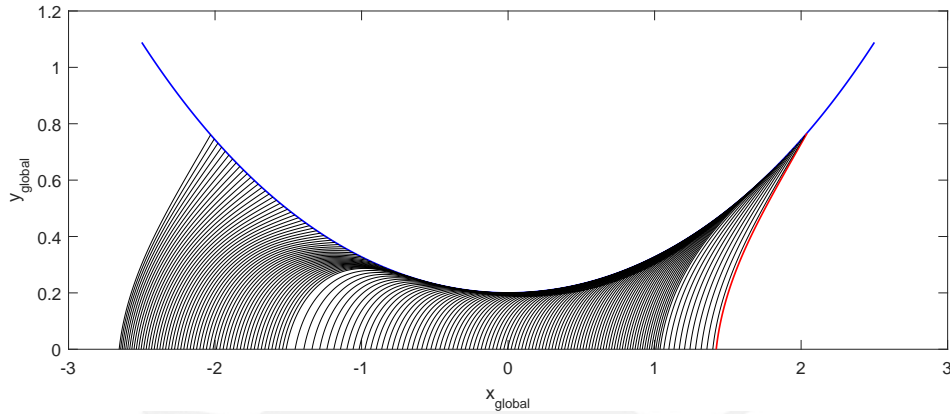


Figure 5.21: Case 3 (catenary): Contact between a catenary profile and a cylindrical, elastic supported vibrissa, with $q = 5$ and $k = 5$. Notice the different contact phases and the deflection at the base.

An elastic support at the base allows to have another measurable magnitude, the deflection angle at the base. This new measured quantity allows more data to be used to reconstruct the profile and obtain the fluid load. Note that for comparison each graph also contains a case with rigid support (continuous line).

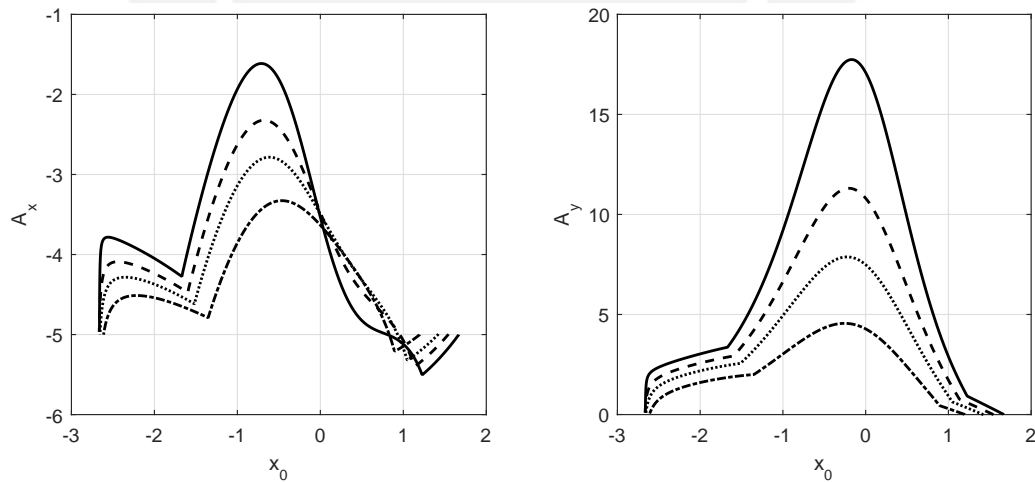


Figure 5.22: Case 3 (catenary): Observable reaction forces in x and y direction. Continuous line: $k = +\infty$, dashed line: $k = 20$, dotted line: $k = 10$, dashed-dotted line: $k = 5$.

During this scenario, it can be seen that there is a decrease in magnitude of the contact force and the measured moment at the base, as seen in Figs. 5.22 to 5.24.

A “delay” in the initial contact is also seen for low values of the torsional stiffness. It is also shown that the torsional spring reduces the “snap” at the end and the last contact condition is now a “slow” loss of contact.

With low values of stiffness at the base, the number of points in the tangential contact

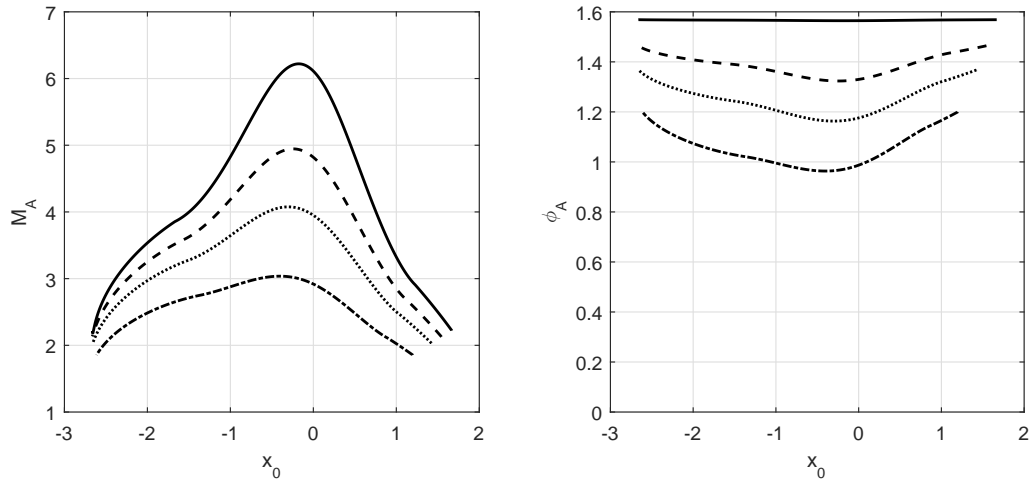


Figure 5.23: Case 3 (catenary): Observable moment reaction and base angle. Continuous line: $k = +\infty$, dashed line: $k = 20$, dotted line: $k = 10$, dashed-dotted line: $k = 5$.

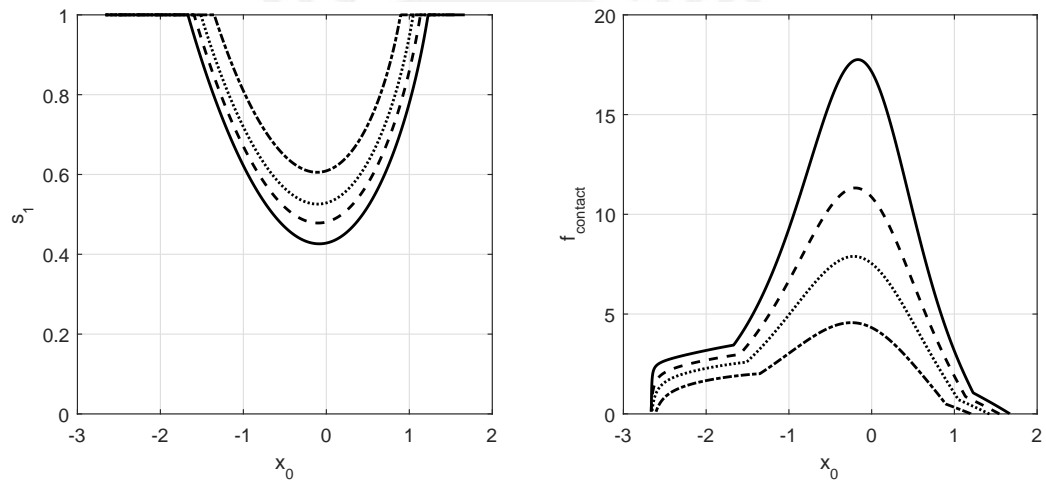


Figure 5.24: Case 3 (catenary): Length s_1 and contact force. Continuous line: $k = +\infty$, dashed line: $k = 20$, dotted line: $k = 10$, dashed-dotted line: $k = 5$.

phase reduces (see Fig. 5.24). The parameter s_1 can be reduced until there are no points in tangential contact and only a tip contact phase occurs (as seen in Fig. 5.27). This case is favorable during the reconstruction of the profile, since the s_1 parameter is known and it is not necessary to determine the contact phase.

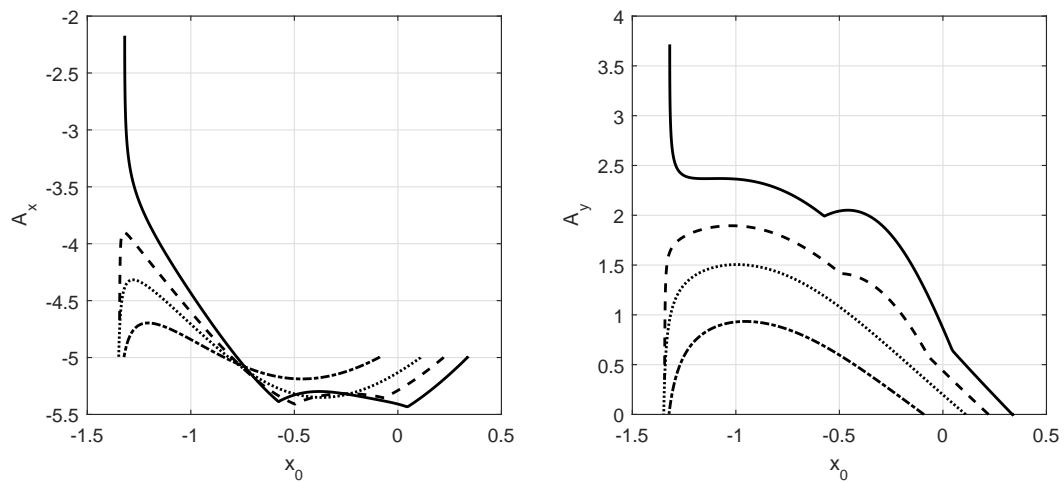


Figure 5.25: Case 3 (parabolic): Observable reaction forces in x and y direction. Continuous line: $k = +\infty$, dashed line: $k = 20$, dotted line: $k = 10$, dashed-dotted line: $k = 5$.

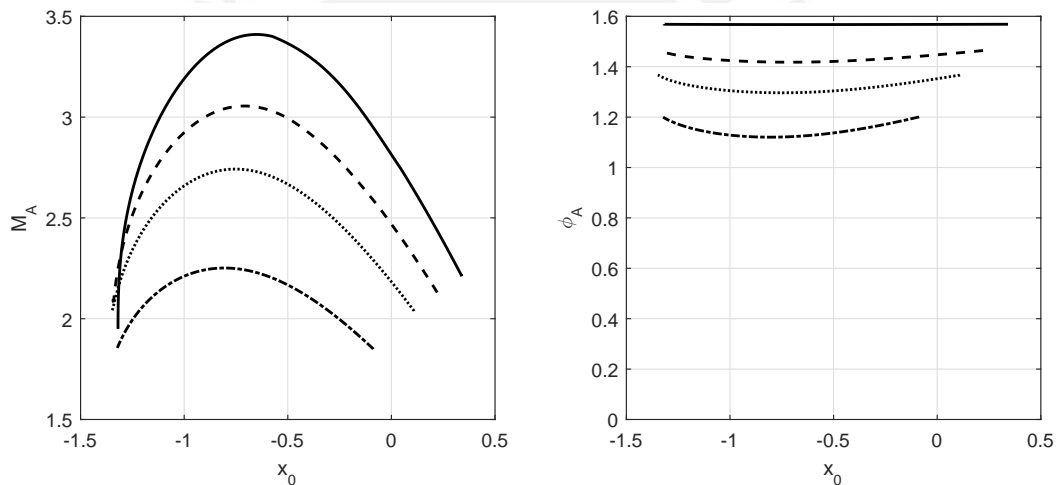


Figure 5.26: Case 3 (parabolic): Observable moment reaction and base angle. Continuous line: $k = +\infty$, dashed line: $k = 20$, dotted line: $k = 10$, dashed-dotted line: $k = 5$.

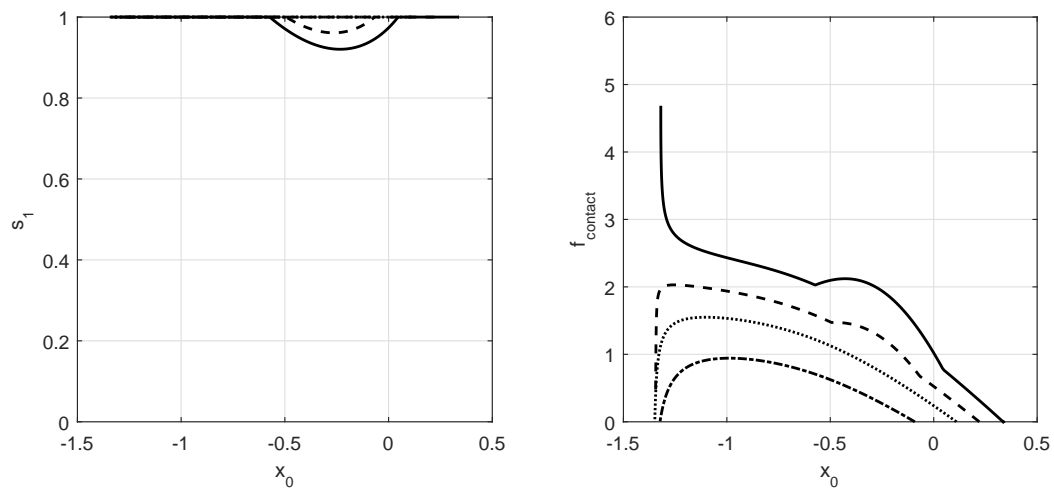


Figure 5.27: Case 3 (parabolic): Length s_1 and contact force. Continuous line: $k = +\infty$, dashed line: $k = 20$, dotted line: $k = 10$, dashed-dotted line: $k = 5$.

5.3.4 Case 4: Contact considering different pre-curvatures

For this study case, two different scenarios are identified, depending on whether the pre-curvature is positive (opposite direction as the flow) or negative (same direction as the flow).

A: Pre-curvature in the same direction of the flow

This case study considers different values for negative pre-curvature for both constant and variable negative pre-curvatures. Note that all graphics include a case with a straight vibrissa (continuous line) for comparison.

$$\boxed{g_1, g_2 \quad q = 5, \quad \vartheta = 1, \quad A \in \{0, -1, -2\}, \quad B \in \{0, -0.5, -1\} \quad k = +\infty} \quad (5.7)$$

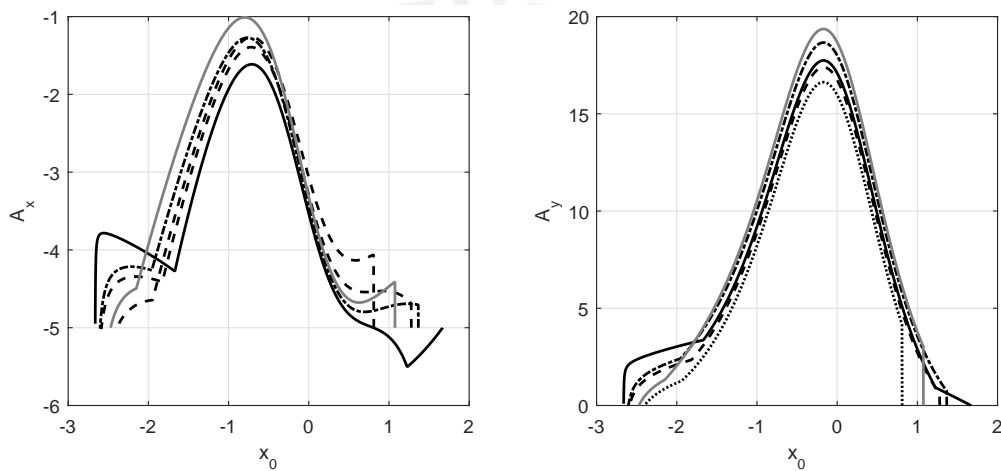


Figure 5.28: Case 4A (catenary): Observable reaction forces in x and y direction. Continuous line: $A = 0, B = 0$; dashed line: $A = 0, B = -0.5$; dotted line: $A = 0, B = -1$; dashed-dotted line: $A = -1, B = 0$; gray line: $A = -2, B = 0$.

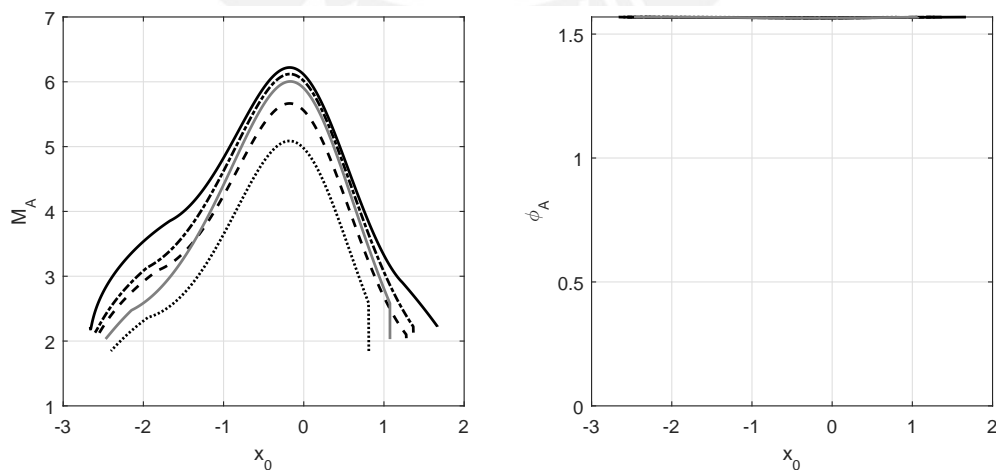


Figure 5.29: Case 4A (catenary): Observable moment reaction and base angle. Continuous line: $A = 0, B = 0$; dashed line: $A = 0, B = -0.5$; dotted line: $A = 0, B = -1$; dashed-dotted line: $A = -1, B = 0$; gray line: $A = -2, B = 0$.

It is shown that most of the cases that include pre-curvature start contacting the profile directly with tangential contact (notice the vertical lines at the starting point). It is also

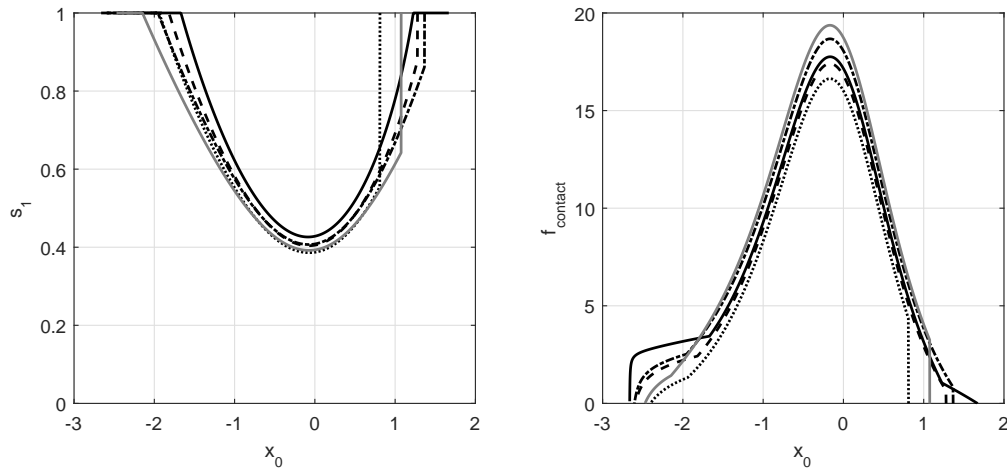


Figure 5.30: Case 4A (catenary): Length s_1 and contact force. Continuous line: $A = 0$, $B = 0$; dashed line: $A = 0$, $B = -0.5$; dotted line: $A = 0$, $B = -1$; dashed-dotted line: $A = -1$, $B = 0$; gray line: $A = -2$, $B = 0$.

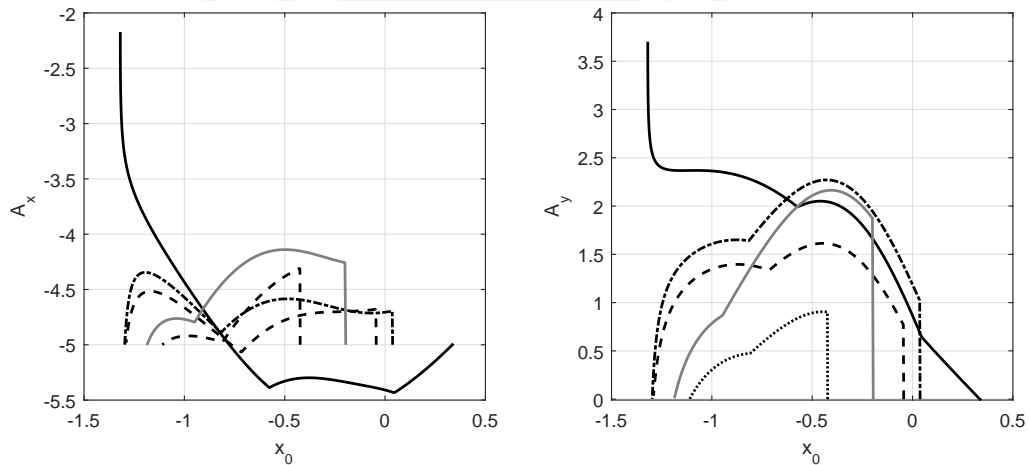


Figure 5.31: Case 4A (parabolic): Observable reaction forces in x and y direction. Continuous line: $A = 0$, $B = 0$; dashed line: $A = 0$, $B = -0.5$; dotted line: $A = 0$, $B = -1$; dashed-dotted line: $A = -1$, $B = 0$; gray line: $A = -2$, $B = 0$.

shown that due to the pre-curvature, no snap at the end occurs and the contact is “slowly” lost (compared the pre-curved cases to the reference case in continuous line).

Also, high pre-curvatures reduce the number of measured points, this becomes apparent with the parabolic contour, notice how the domain of x_0 is reduced with increasing negative pre-curvatures. This largely affects the section of the obstacle contour that is reconstructed.

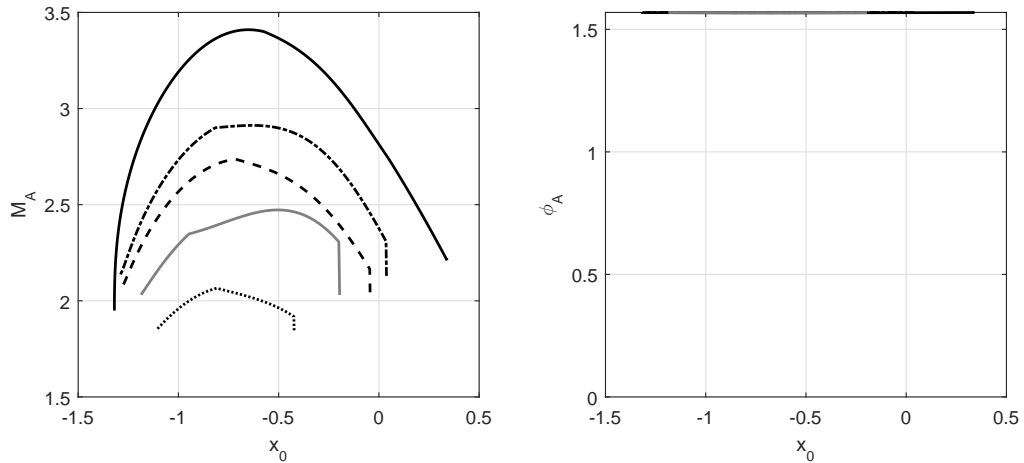


Figure 5.32: Case 4A (parabolic): Observable moment reaction and base angle. Continuous line: $A = 0, B = 0$; dashed line: $A = 0, B = -0.5$; dotted line: $A = 0, B = -1$; dashed-dotted line: $A = -1, B = 0$; gray line: $A = -2, B = 0$.

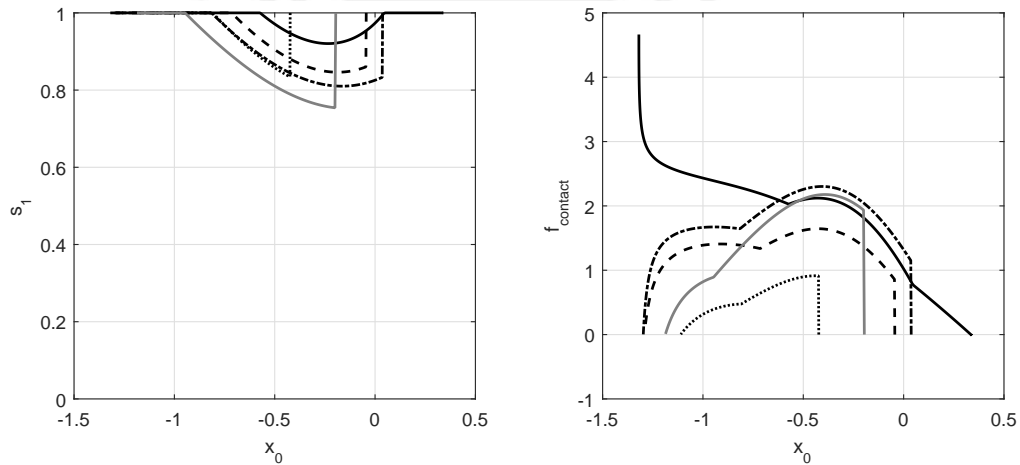


Figure 5.33: Case 4A (parabolic): Length s_1 and contact force. Continuous line: $A = 0, B = 0$; dashed line: $A = 0, B = -0.5$; dotted line: $A = 0, B = -1$; dashed-dotted line: $A = -1, B = 0$; gray line: $A = -2, B = 0$.

B: Pre-curvature in the opposite direction of the flow

This case study considers vibrissa with positive pre-curvature.

Remark 5.1 *During this case study, only scenarios with one contact point are evaluated. It is found that during contact, more than one point might come into contact with the profile due to the pre-curvature of the vibrissa, and thus resulting in an incomplete reconstruction of the profile. The study of the parabolic profile (5.3) does not exhibit this behavior; however, the catenary profile (5.2) does. This is due to the proximity of the obstacle to the base of the vibrissa. The existence of these extra intersections needs to be tested in every calculation step to ensure that there is only one contact point, the verification is performed with the intersection algorithm found in [Schwarz 2005].*

Similar values as in case 4 A are tested (but with positive values):

$$\boxed{g_2, \quad q = 5, \quad \vartheta = 1, \quad A \in \{0, 1, 2\}, \quad B \in \{0, 0.5, 1\}, \quad k = +\infty} \quad (5.8)$$

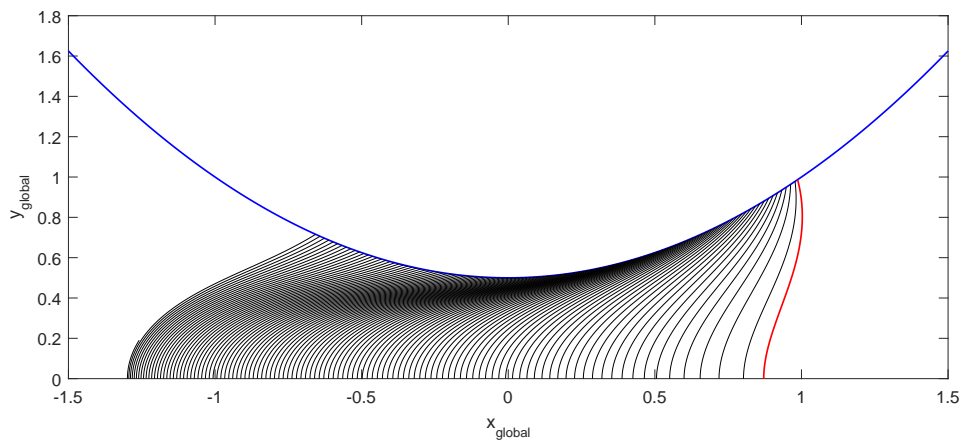


Figure 5.34: Case 4B (parabolic): Contact between a parabolic profile and a positively pre-curved vibrissa.

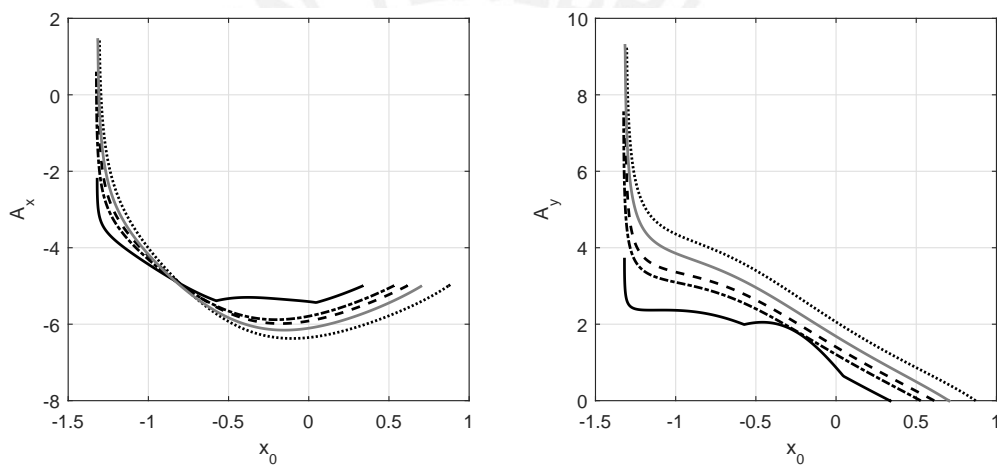


Figure 5.35: Case 4B (parabolic): Observable reaction forces in x and y direction. Continuous line: $A = 0, B = 0$; dashed line: $A = 0, B = 0.5$; dotted line: $A = 0, B = 1$; dashed-dotted line: $A = 1, B = 0$; gray line: $A = 2, B = 0$.

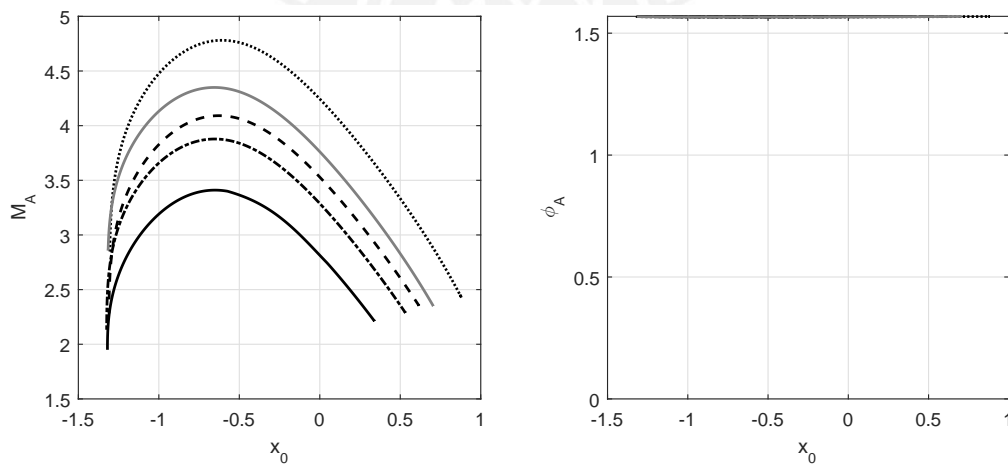


Figure 5.36: Case 4B (parabolic): Observable moment reaction and base angle. Continuous line: $A = 0, B = 0$; dashed line: $A = 0, B = 0.5$; dotted line: $A = 0, B = 1$; dashed-dotted line: $A = 1, B = 0$; gray line: $A = 2, B = 0$.

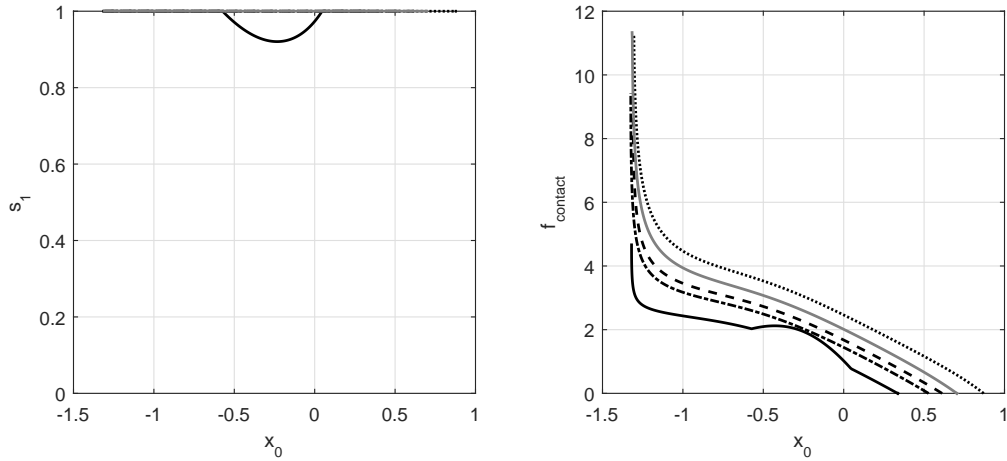


Figure 5.37: Case 4B (parabolic): Length s_1 and contact force. Continuous line: $A = 0$, $B = 0$; dashed line: $A = 0$, $B = 0.5$; dotted line: $A = 0$, $B = 1$; dashed-dotted line: $A = 1$, $B = 0$; gray line: $A = 2$, $B = 0$.

It can be seen in the cases of the parabolic contour that the vibrissa never enters the tangential contact phase. In contrast to other case studies, the number of measure points is increased due to the positive pre-curvature. This allows an “earlier” initial contact point, while maintaining approximately the same last contact point.

5.3.5 Case 5: Contact with all previous considerations

After studying the behavior with different values of conicity, torsional stiffness and pre-curvature; a study considering a combination of parameters is performed for both test profiles.

A: Catenary profile

This case study takes into consideration the catenary profile as well as a negatively pre-curved, conical vibrissa with an elastic support.

$$g_1, \quad q = 5, \quad \vartheta \in \{0.75, 0.5\}, \quad A = -1, \quad B = -0.5, \quad k \in \{10, 20\} \quad (5.9)$$

Due to the combined effect of the pre-curvature, the conicity and elastic support, all the results show a tangential initial contact. Figure 5.40 also shows that the elastic support has a far more influence on the contact force than the conicity.

B: Parabolic profile

This study case takes into consideration the parabolic profile and a positively pre-curved, conical vibrissa with an elastic support.

$$g_2, \quad q = 5, \quad \vartheta \in \{0.75, 0.5\}, \quad A = 2, \quad B = 0, \quad k \in \{10, 20\} \quad (5.10)$$

Results show that the positive pre-curvature helps to increase the number of points measured (compare the results with those in case studies 2 and 3). Furthermore, due to the pre-curvature, the last contact condition is a sudden “snap”, except when the overall bending stiffness is low (low conicity parameter ϑ and low k). Also, due to the absence of tangential contact, the deflection angle at the base remains fairly constant.

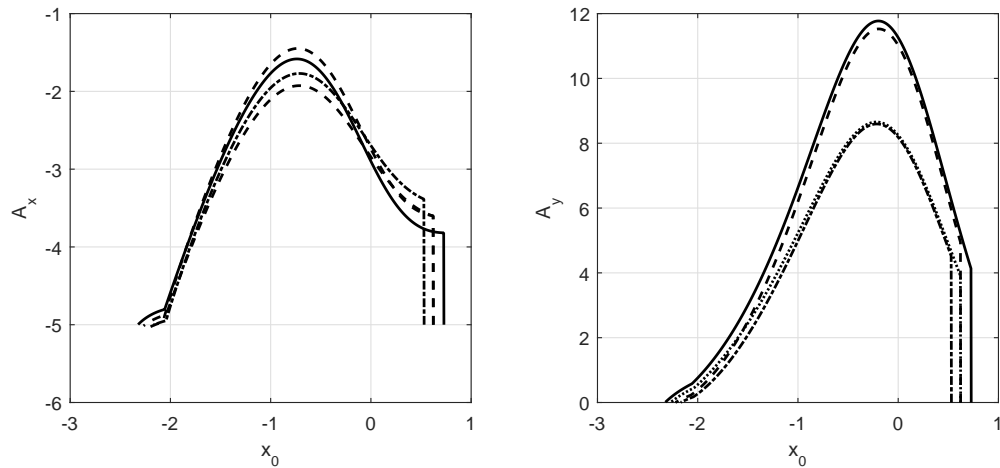


Figure 5.38: Case 5 (catenary): Observable reaction forces in x and y direction. Continuous line: $\vartheta = 0.75$, $k = 20$; dashed line: $\vartheta = 0.5$, $k = 20$; dotted line: $\vartheta = 0.75$, $k = 10$; dashed-dotted line: $\vartheta = 0.5$, $k = 10$.

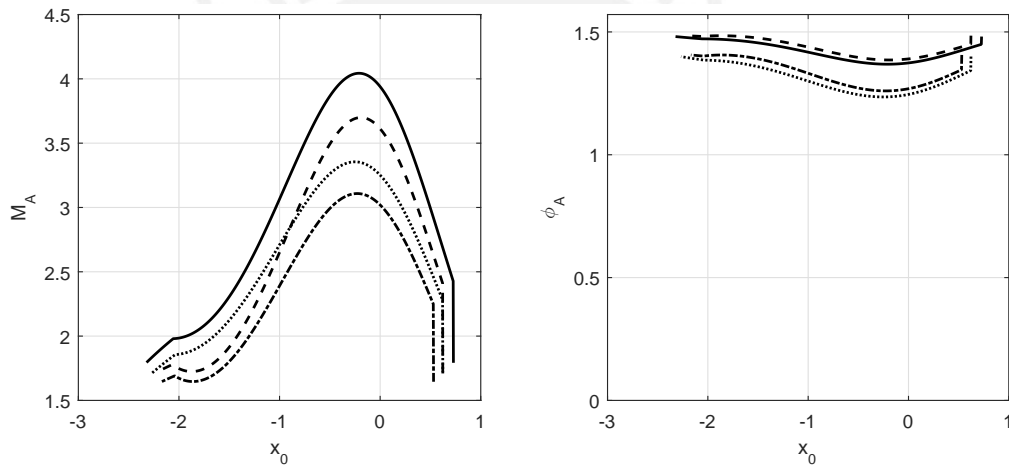


Figure 5.39: Case 5 (catenary): Observable moment reaction and base angle. Continuous line: $\vartheta = 0.75$, $k = 20$; dashed line: $\vartheta = 0.5$, $k = 20$; dotted line: $\vartheta = 0.75$, $k = 10$; dashed-dotted line: $\vartheta = 0.5$, $k = 10$.

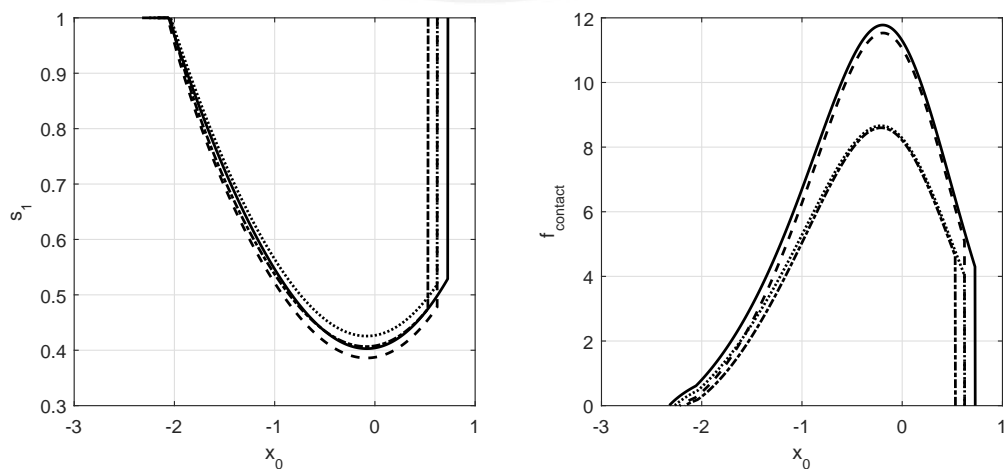


Figure 5.40: Case 5 (catenary): Length s_1 and contact force. Continuous line: $\vartheta = 0.75$, $k = 20$; dashed line: $\vartheta = 0.5$, $k = 20$; dotted line: $\vartheta = 0.75$, $k = 10$; dashed-dotted line: $\vartheta = 0.5$, $k = 10$.

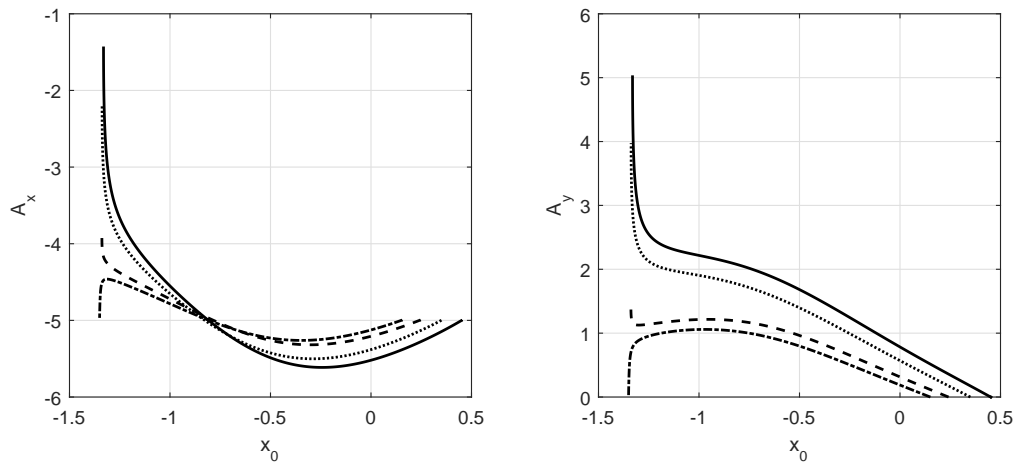


Figure 5.41: Case 5 (parabolic): Observable reaction forces in x and y direction. Continuous line: $\vartheta = 0.75$, $k = 20$; dashed line: $\vartheta = 0.5$, $k = 20$; dotted line: $\vartheta = 0.75$, $k = 10$; dashed-dotted line: $\vartheta = 0.5$, $k = 10$.

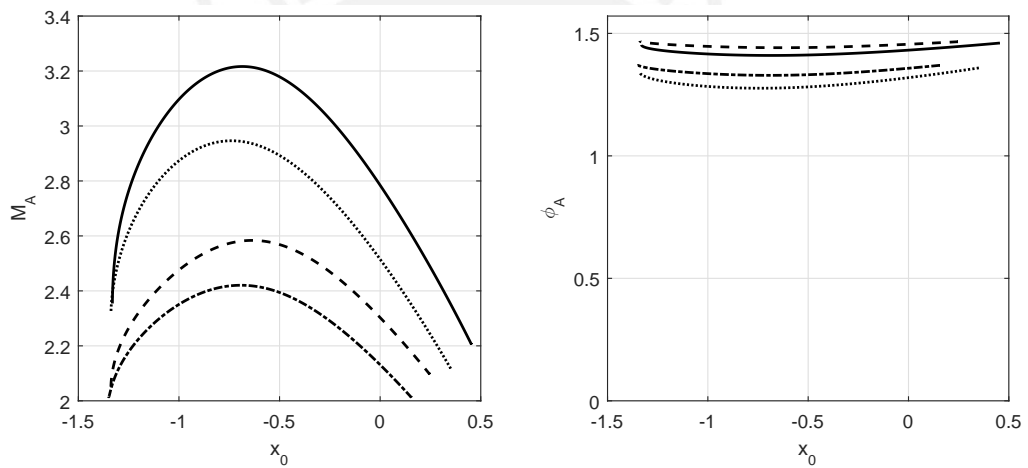


Figure 5.42: Case 5 (parabolic): Observable moment reaction and base angle. Continuous line: $\vartheta = 0.75$, $k = 20$; dashed line: $\vartheta = 0.5$, $k = 20$; dotted line: $\vartheta = 0.75$, $k = 10$; dashed-dotted line: $\vartheta = 0.5$, $k = 10$.

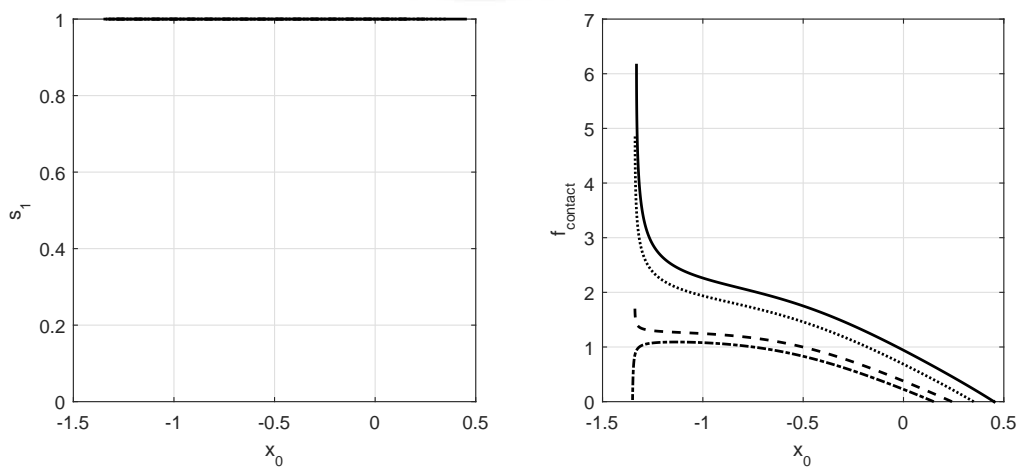


Figure 5.43: Case 5 (parabolic): Length s_1 and contact force. Continuous line: $\vartheta = 0.75$, $k = 20$; dashed line: $\vartheta = 0.5$, $k = 20$; dotted line: $\vartheta = 0.75$, $k = 10$; dashed-dotted line: $\vartheta = 0.5$, $k = 10$.

5.4 Comparison between a experimental sweep and a theoretical sweep

An experimental sweep, performed in [Will et al. 2016], is compared with the theoretical sweep by the algorithm. The profile used for this comparison is the parabola described by (5.11).

$$g_e : y_{cont}(x_{cont}) = 2 \left(x_{cont} + \left(\frac{5}{312} \right) \sqrt{858} \right)^2 + \frac{349}{624} \quad (5.11)$$

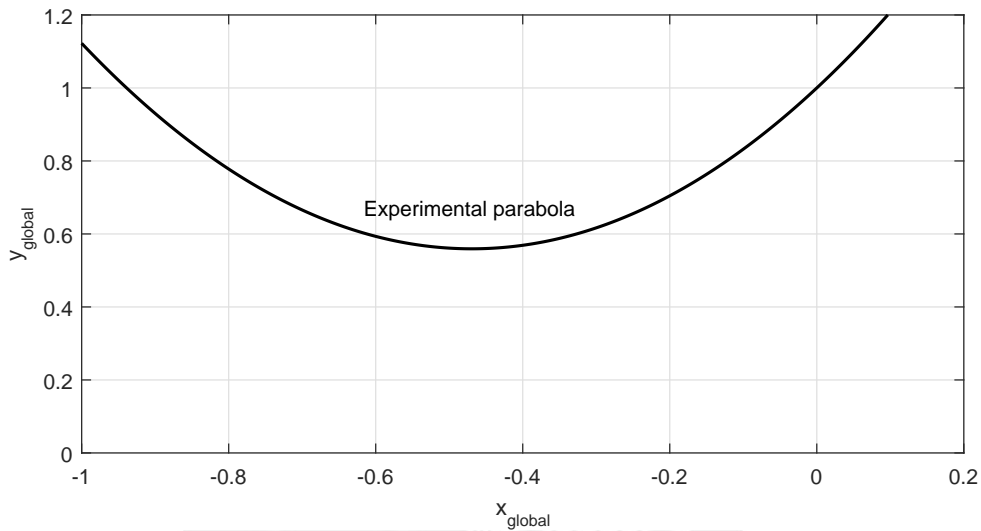


Figure 5.44: Contour profile of the parabolic curve for the experimental sweep.

The experimental sweep is performed without the presence of a fluid load, thus a simulation of contact without fluid flow is also performed, in order to compare the resulting observables obtained by the developed algorithm and the measured data from Will et al. 2016, the setup of the experiment is displayed in Fig. 5.45.

For the theoretical “sweep”, the following considerations are taken:

$$\boxed{g_e, \quad q = 0, \quad \vartheta = 1, \quad A, B = 0, \quad k = +\infty} \quad (5.12)$$

It can be observed in Fig. 5.46 that although both set of observables show a similar behavior there are still differences in the magnitudes. These differences become much more evident with high loads, as seen near the last contact point. Certain factors can be accounted for this difference:

- The contact during the simulation is regarded as ideal and frictionless. However, during the experiment a frictional force does act on the surface, which was not considered during the simulation (as the force applied is ideal and always perpendicular to the curves). This may be one of the reasons for the increase in the contact force at the last contact point, which does not reach the same heights as in the experiment.
- The effect of the imperfections of the surface also influence the measurements, as it affects the “smoothness” of the curve.
- The sensors used are limited by its sensitivity and resolution, and may also pick noise from the environment.
- The FDM used during the contact simulation carries a truncation error higher than the other more traditionally used methods.

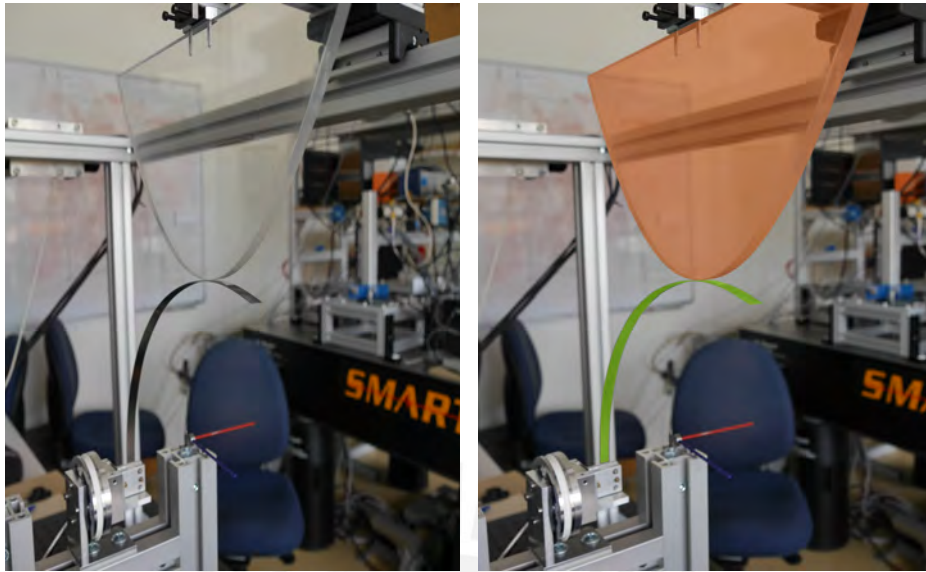


Figure 5.45: Experimental setup for the “sweep” of a parabolic profile. Left: original picture. Right: highlight of the vibrissa sensor and the profile. Courtesy of [Behn et al. 2016].

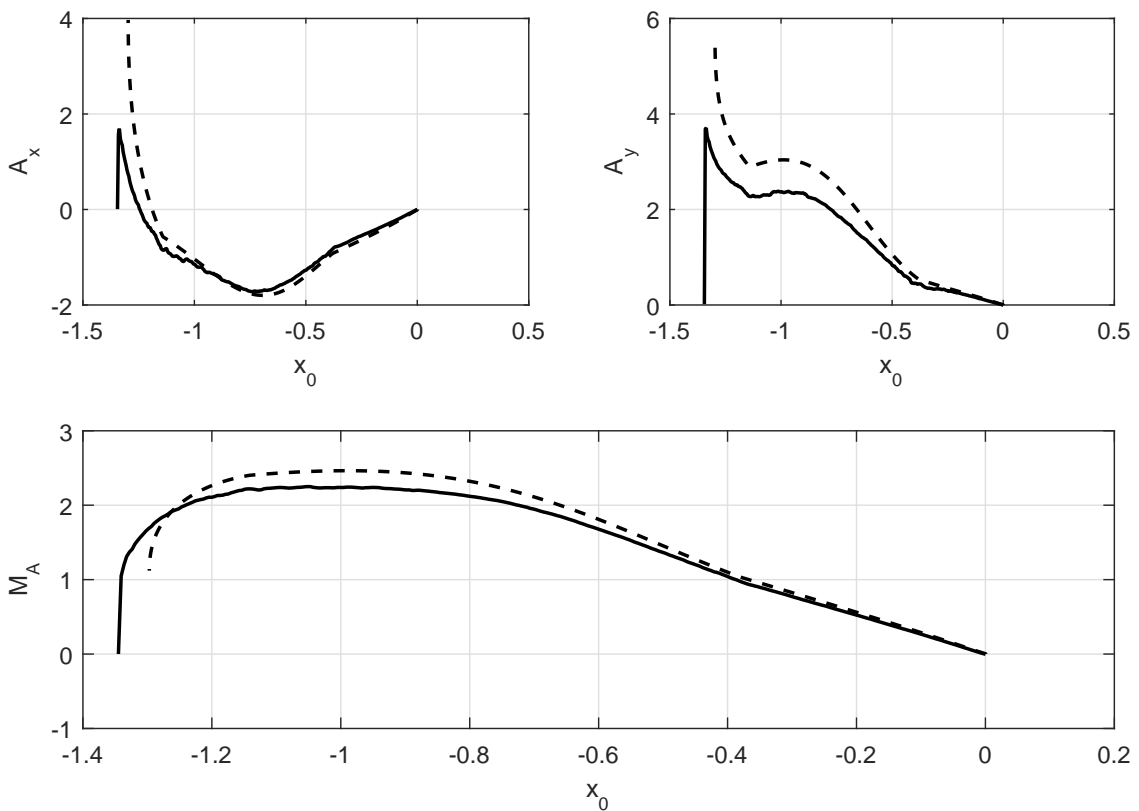


Figure 5.46: Comparison of the observables obtained through the experimental sweep (continuous line) by [Will et al. 2016] and those with the algorithm developed (dashed line).

5.5 Summary and comments

- A procedure for the obtainment of the observables from the contact simulation of an obstacle's profile under fluid loads is developed, under certain considerations explained early in this chapter.
- In general, the change from one contact phase to the other can be easily identified, in each reaction force plot. A sudden change in the slope of the curve indicates the change.
- Characteristics that lower the overall bending stiffness of the system tend to decrease the number of measured points, as the x_0 domain is reduced. Another characteristic that reduces the number of points measured is the magnitude of the fluid flow load, as it bends the vibrissa before it comes into contact with the obstacle. Positive pre-curvatures, however, increase the number of measured points.
- It can be seen in cases with negative pre-curvature that contact force suddenly increases upon contact. These cases require further studies, of the fluid load, since the contact force should grow gradually and not with a "jump". This happens due to the assumption that the fluid load acts uniformly between the base and the contact point. In reality, the fluid flow load does not act uniformly on the entire length and, depending on the form of the vibrissa, also acts on the segment from the contact point to the tip. Thus, further studies of the flow behavior in pre-curved beams is needed, so a better representation of the fluid load is chosen.
- Even though positive pre-curvatures increase the number of measured points, the base of the vibrissa must be kept at a certain distance to avoid more than one contact point.
- From the results obtained, it can be seen that the characteristic that influences more the contact force, and thus the measured base reactions, is the stiffness of the torsional spring at the base. Low values of the torsional stiffness may even cause that the vibrissa only comes into tip contact with the obstacle.
- The value of the conicity parameter seems to not largely affect the measured reactions, however, its influence is more evident in the measured base bending moment.
- Certain scenarios require that the obstacle contour curve to be defined with a higher number of points. This is mostly the case where there is a snap at the last contact point, since the condition of a minimum is not met due to the few calculation points. If the number of points is low, the point (where the exit condition is fulfilled) might be skipped.
- The obtained observable magnitudes are used in the next chapter to determine both the magnitude of the fluid load and to reconstruct the obstacle contour profile.

Chapter 6

Contour profile reconstruction and fluid flow identification

In the previous chapters, the mechanical behavior of the vibrissa-inspired sensors is studied, as well as the contact between an obstacle and a vibrissa. In this chapter, the measured quantities are used to obtain the magnitude of the fluid load and to reconstruct the contour profiles of the previous chapter. The detection is divided in two stages

- detection of the fluid flow load before contact, which gives a value of the fluid load applied and uses the first point of measurement;
- reconstruction of the contour, which analyzes the observable quantities and uses them to reconstruct the contour profile.

6.1 Fluid flow detection

The first step in the detection phase is to identify the magnitude of the fluid load, as it remains constant. It can be easily obtained using the equilibrium equations shown in (6.1). The values of the observables are found as the first point in each of the observables.

$$\begin{aligned}\Sigma F_x = 0 : & \quad A_x = -q \cdot (s_1 - 0) \\ \Sigma F_y = 0 : & \quad A_y = 0\end{aligned}\tag{6.1}$$

Also, the coordinates of the tip of the vibrissa need to be determined, since they provide information about the initial contact point (for the cases where the initial contact is phase A). Using the information at the base, the FDM algorithm developed in Chapter 4 is used in combination with `fsolve` to determine the fluid load, as well as the tip coordinates. The values that produce base reactions that match those measured are taken as solution. The obtained values also work as starting points for the solution in the next stage.

Remark 6.1 *The general case considers that the fluid load is only applied in a certain length of the vibrissa, thus the s_1 instead of 1 in (6.1). This notation becomes useful in the next section, as the fluid load does not act along the whole vibrissa. It also proves useful if future investigations do not consider the distributed load uniform.*

In all cases, the algorithm obtains almost the exact same fluid load, the difference between the applied (q) and the measured fluid load ($q_{measured}$) shown in (Eq. (6.2)).

$$\Delta q = q - q_{measured}\tag{6.2}$$

Table 6.1: Difference between the applied and measured fluid flow loads.

Case 1				
Applied q	0	1	5	10
Δq	2.34E+07	-5.75E-08	-3.14E-07	5.01E-10
Case 2				
ϑ	1	0.75	0.5	0.25
Applied q	5	5	5	5
Δq	-3.14E-07	1.22E-09	4.09E-10	8.89E-10
Case 3				
k	infy	20	10	5
Applied q	5	5	5	5
Δq	-3.14E-07	-2.87E-07	-3.63E-07	-3.83E-07
Case 4A				
A	0	0	-1	-2
B	-0.5	-1	0	0
Applied q	5	5	5	5
Δq	1.37E-07	4.02E-07	-7.55E-08	4.31E-07
Case 4B				
A	0	0	1	2
B	0.5	1	0	0
Applied q	5	5	5	5
Δq	6.90E-07	3.34E-06	5.05E-12	2.03E-11
Case 5 (catenary)				
A	-1	-1	-1	-1
B	-0.5	-0.5	-0.5	-0.5
k	20	20	10	10
ϑ	0.75	0.5	0.75	0.5
Applied q	5	5	5	5
Δq	5.86E-07	-2.36E-12	5.36E-09	1.87E-12
Case 5 (parabolic)				
A	2	2	2	2
B	0	0	0	0
k	20	20	10	10
ϑ	0.75	0.5	0.75	0.5
Applied q	5	5	5	5
Δq	1.12E-09	2.10E-09	9.48E-10	2.58E-09

6.2 Reconstruction of profile

After obtaining the magnitude of the fluid load, the contour profile has to be rebuilt. However, the unknowns are different for both contact phases. For each phase there are five unknown variables:

- for phase A (tip contact), note that $s_1 = 1$:

$$\boxed{x_{cont}, y_{cont}, \psi_{cont}, f, \varphi_1} \quad (6.3)$$

- for phase B (tangential contact), note that $\varphi_1 = \psi_{cont}$:

$$\boxed{x_{cont}, y_{cont}, \psi_{cont}, f, s_1} \quad (6.4)$$

Remark 6.2 *If there were no fluid flow, then the slope angle at each point ψ_{cont} could be calculated using only the reactions at the base. For this case, the tangent of the slope angle ψ_{cont} is given the relationship of the reactions, just as in the procedure found in [Will et al. 2014b].*

Since there are five unknowns, for either case five equations are needed to obtain the values. These equations are formed from the obtained observables and are valid for both contact phases.

- Condition 1: Distance between the tip (x_1, y_1) and the contact point (x_{cont}, y_{cont}) must be zero, since they are the same point.

$$d = \sqrt{(x_1 - x_{cont})^2 + (y_1 - y_{cont})^2} = 0 \quad (6.5)$$

- Condition 2: Moment at the contact point (m_1) must be zero

$$m_1 = \kappa_1 - A s_1 - B = 0 \quad (6.6)$$

- Condition 3: Moment at the base must be equal to the measured value

$$M_A = -\kappa_0 - B \quad (6.7)$$

- Condition 4: Force equilibrium in the x -direction

$$\Sigma F_x = 0 : \quad A_x = -q \cdot (s_1 - 0) - f \sin(\psi_{cont}) \quad (6.8)$$

- Condition 5: Force equilibrium in the y -direction

$$\Sigma F_y = 0 : \quad A_y = f \cos(\psi_{cont}) \quad (6.9)$$

Equations (6.5) to (6.9) require the values for x_1 , y_1 , φ_1 as well as the curvature at the base κ_0 and at the tip κ_1 . These values are determined using the FDM algorithm found in Fig. 4.2, however, the deflection angle at the base is already known from the observables. The MATLAB function `fsolve` is used to approximate the result. However, the default tolerance of 10^{-6} is too small for the calculations as only a tolerance of 10^{-4} is achievable. It is found that smaller tolerances are achievable, however, they require an extremely high number of iterations and in some points it may not be possible. It is also found that results are extremely dependent on the starting guess of values, thus the values obtained from the previous point are used as starting values.

The main difficulty in this simulations is to decide in which contact phase the vibrissa is, whether it is phase A or B. This difficulty is also experienced by [Will et al. 2014a], [Will et al. 2014b], [Will et al. 2015]. However, the decision condition found in these works cannot be applied due to the different approach and the presence of a fluid load, since the phase cannot be defined a priori.

6.2.1 Determination of first contact phase

Due to the fact that some of the contact simulations show that it is possible that contact begins with phase B, it has to be determined beforehand if the contact starts with phase B. The main characteristic of these cases is that the horizontal reaction A_x is partially reduced upon contact (due to the assumption that the fluid load only acts from the base to s_1 and $s_1 < 1$). Thus, if a reduction in the measured horizontal reaction is detected, the starting contact can be established to be in phase B.

Remark 6.3 (Determination of first contact phase) *The assumption taken in to decide if the first contact phase is A or B is based purely on the assumptions made in previous chapter. This assumption is likely to change when experimental data is available or a more complex assumption of the fluid flow load is taken.*

6.2.2 Determination of contact phase of any point

A first approach to determine in which phase the contact is, was to perform the calculations assuming both phases for each point and then comparing the results and conditions for both, and pick the result set that satisfied its corresponding conditions. However, this procedure proved to have two major drawbacks: the required time to reconstruct the profile was doubled (up to 4 hours compared to the 10 minutes required to obtain the observables); and there were points where both solutions appeared to be valid – and in some cases, no solution was found due to the sensitivity to the starting guess values.

A workaround to determine the contact phase beforehand and avoid miscalculations is developed. It can be seen the measured observables (especially A_y) have a sudden slope change, which indicates a contact phase change. Therefore, each at the start of each calculation, an evaluation needs to be done in order to determine whether there is a phase change. This slope change or “jumping discontinuity” requires the derivative of A_y to be determined for the next step beforehand and compared with the current value:

$$\delta = \left. \frac{dA_y}{dx_0} \right|_{k+1} - \left. \frac{dA_y}{dx_0} \right|_k > a_{diff} \quad (6.10)$$

This evaluation is performed at the end of each calculation step, in order to make a decision for the next step. If the condition (6.10) is fulfilled, then a discontinuity is found and in the next step the contact phase changes from A to B or vice versa. The value of a_{diff} is picked after analyzing the behavior of A_y obtained in the previous chapter. A value of 1 is more than enough to guarantee the detection of the discontinuity.

Additionally, each result set for each point must fulfill the conditions for its corresponding phase, those are:

- $\varphi_1 > \psi_{cont}$ and $s_1 = 1$ for points belonging to contact phase A,
- $s_1 < 1$ and $\varphi_1 = \psi_{cont}$ for points belonging to contact phase B.

The procedure is summarized in Fig. 6.1.

6.3 Result sets

All cases studied in Chapter 5 are reconstructed for both test profiles g_1 and g_2 . In order to evaluate the accuracy of the reconstruction, the difference between the reconstructed y_{rec} coordinate and its corresponding expected y_{exp} coordinate is calculated for each point:

$$e := \left| y_{rec} - y_{exp} \right| \quad (6.11)$$

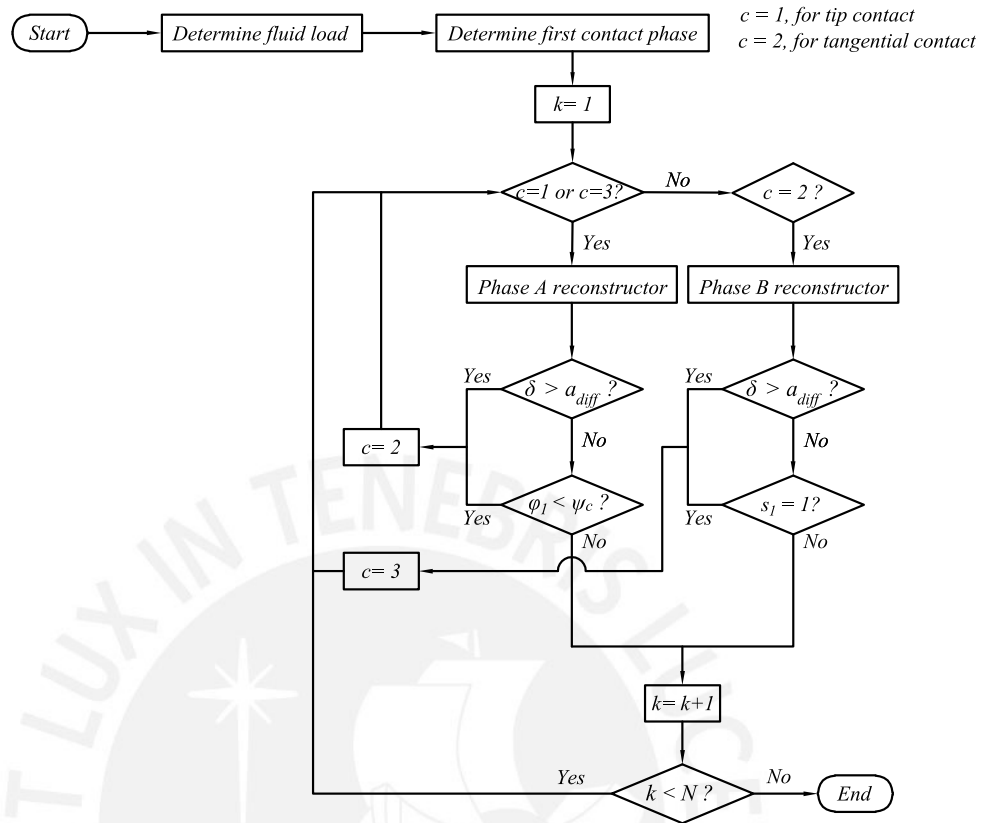


Figure 6.1: Detection algorithm for the flow identification and profile reconstruction.

The y_{real} coordinate is obtained by evaluating the functions g_1 or g_2 on each of the reconstructed x_{rec} points:

$$y_{exp} = g(x_{rec}) \quad (6.12)$$

Figs. 6.2 to 6.12 display the error obtained with (6.11) as a measure of reconstruction quality.

6.3.1 Case 1: Contact considering different fluid loads

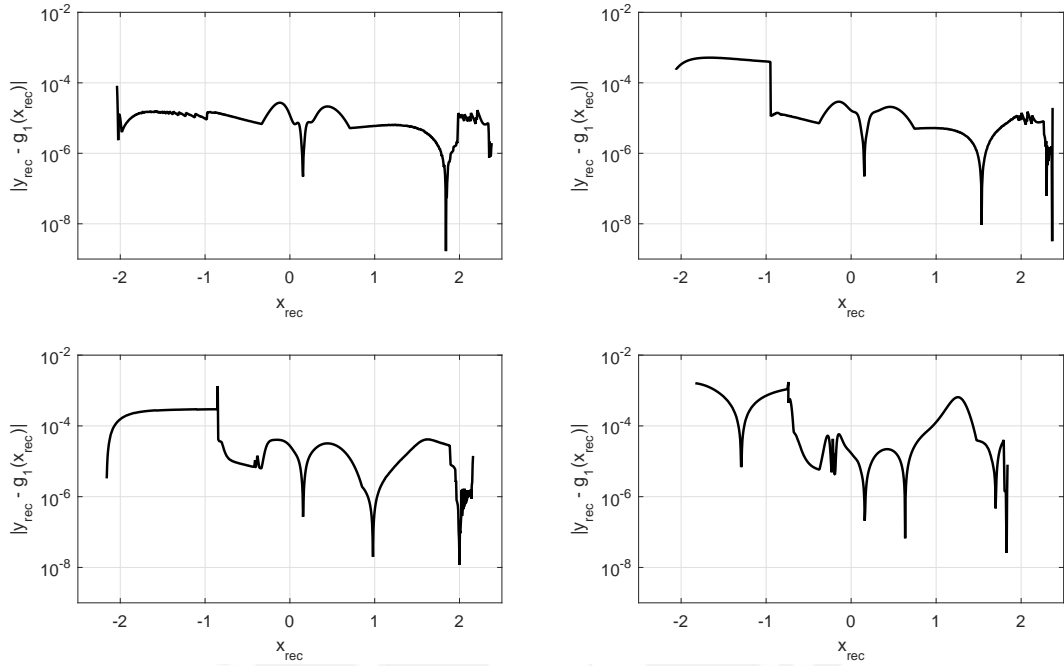


Figure 6.2: Error terms for g_1 : Top left: $q = 0$, top right: $q = 1$, bottom left: $q = 5$, bottom right: $q = 10$.

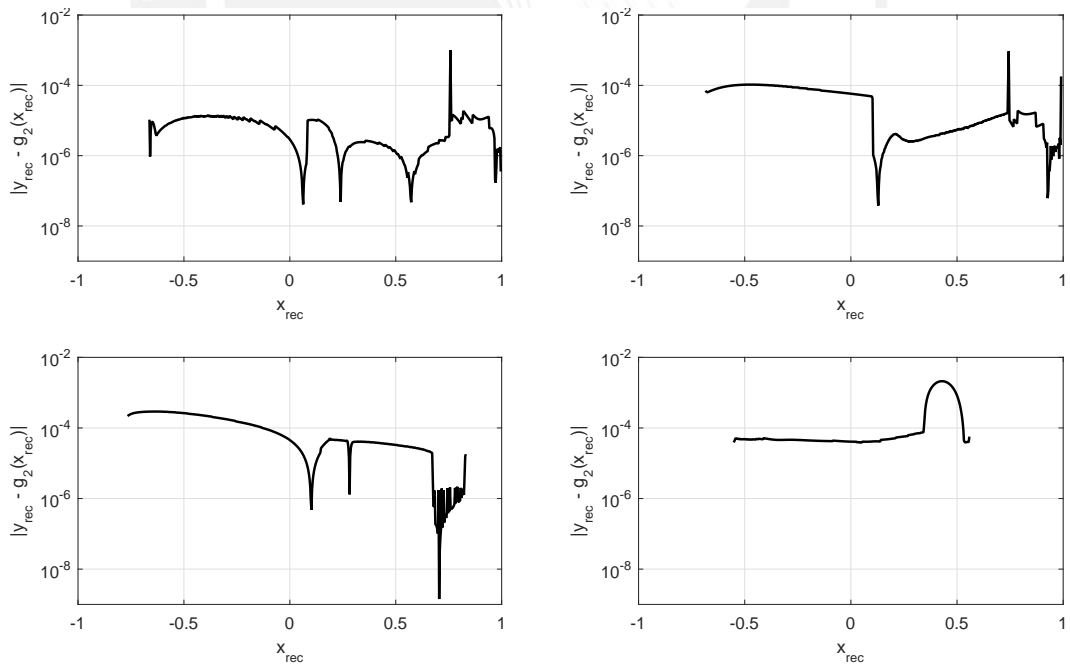


Figure 6.3: Error terms for g_2 : Top left: $q = 0$, top right: $q = 1$, bottom left: $q = 5$, bottom right: $q = 10$.

6.3.2 Case 2: Contact considering different conicity parameters

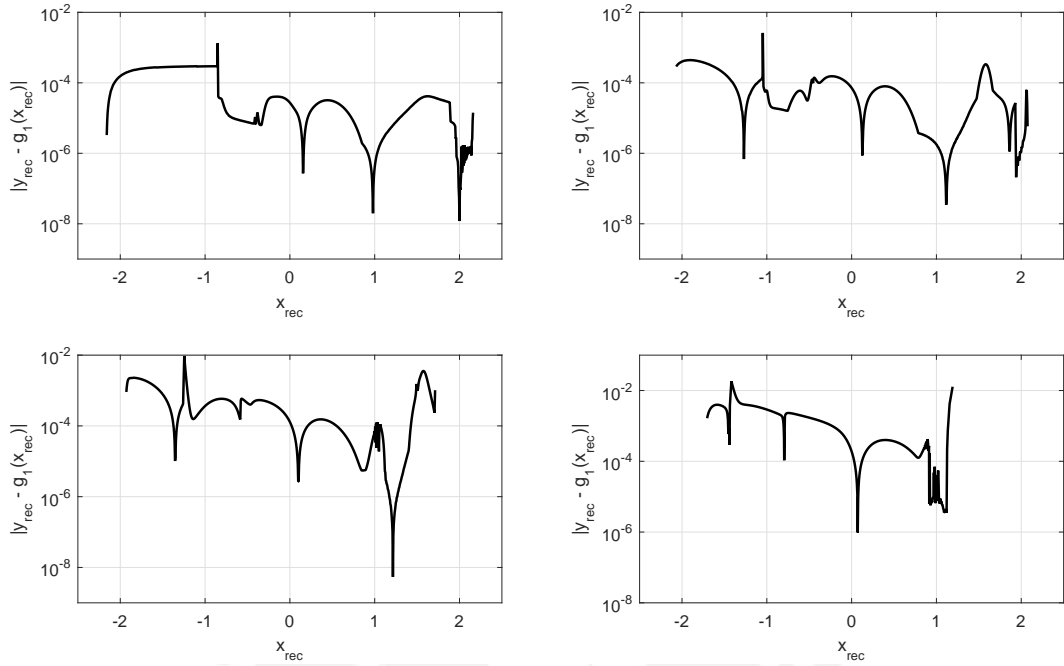


Figure 6.4: Error terms for g_1 and $q = 5$: Top left: $\vartheta = 1$, top right: $\vartheta = 0.75$, bottom left: $\vartheta = 0.5$, bottom right: $\vartheta = 0.25$.

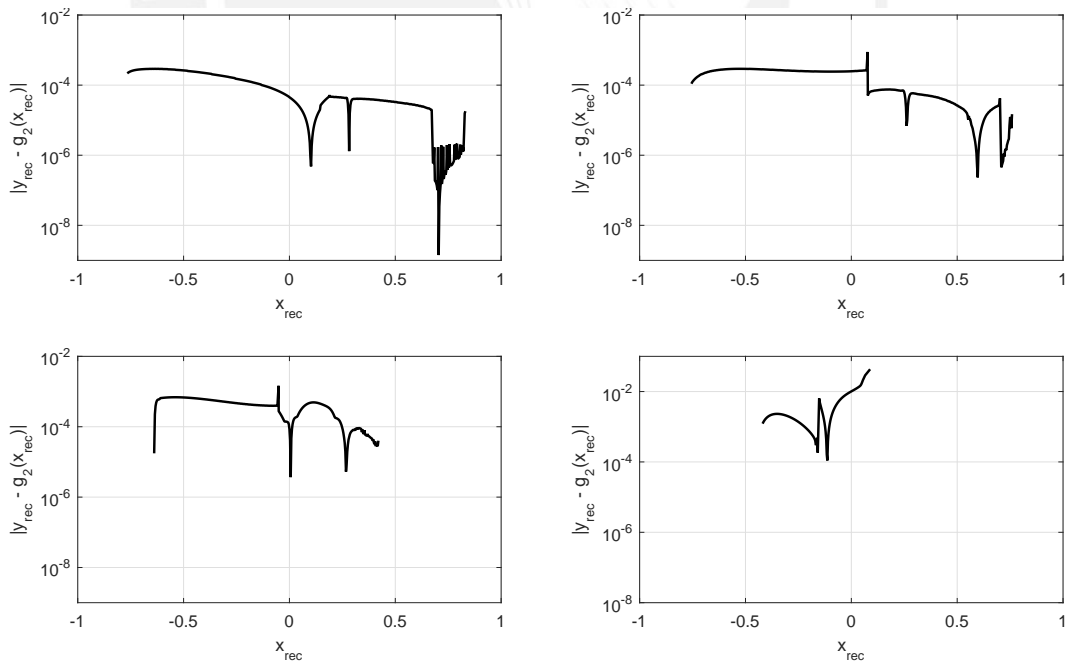


Figure 6.5: Error terms for g_2 and $q = 5$: Top left: $\vartheta = 1$, top right: $\vartheta = 0.75$, bottom left: $\vartheta = 0.5$, bottom right: $\vartheta = 0.25$.

6.3.3 Case 3: Contact considering different torsional stiffness at the base

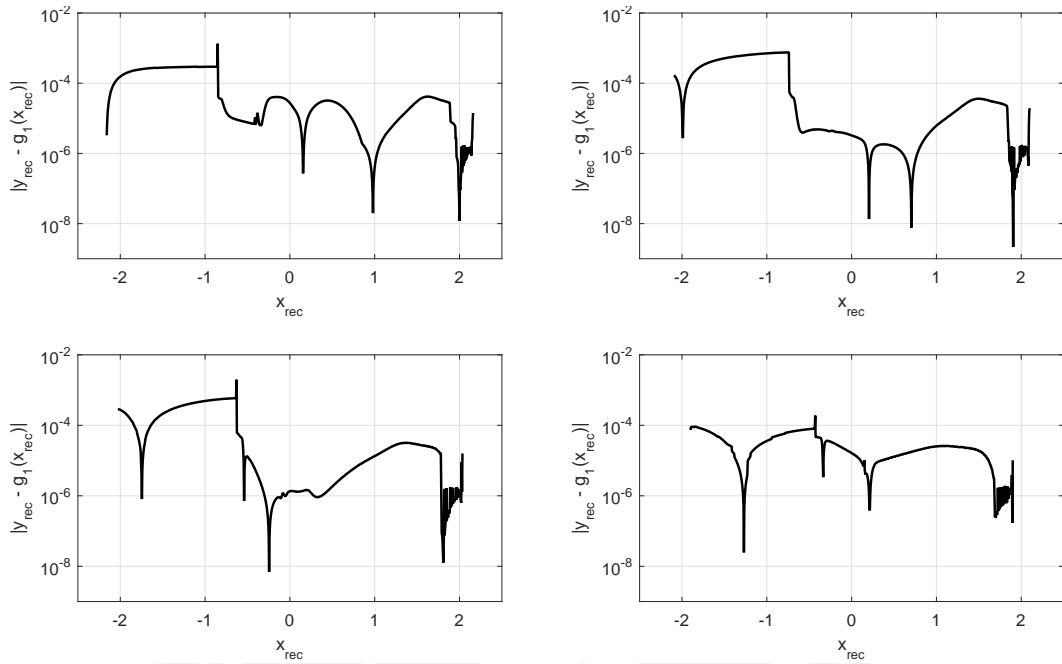


Figure 6.6: Error terms for g_1 and $q = 5$: Top left: $k = \infty$, top right: $k = 20$, bottom left: $k = 10$, bottom right: $k = 5$.

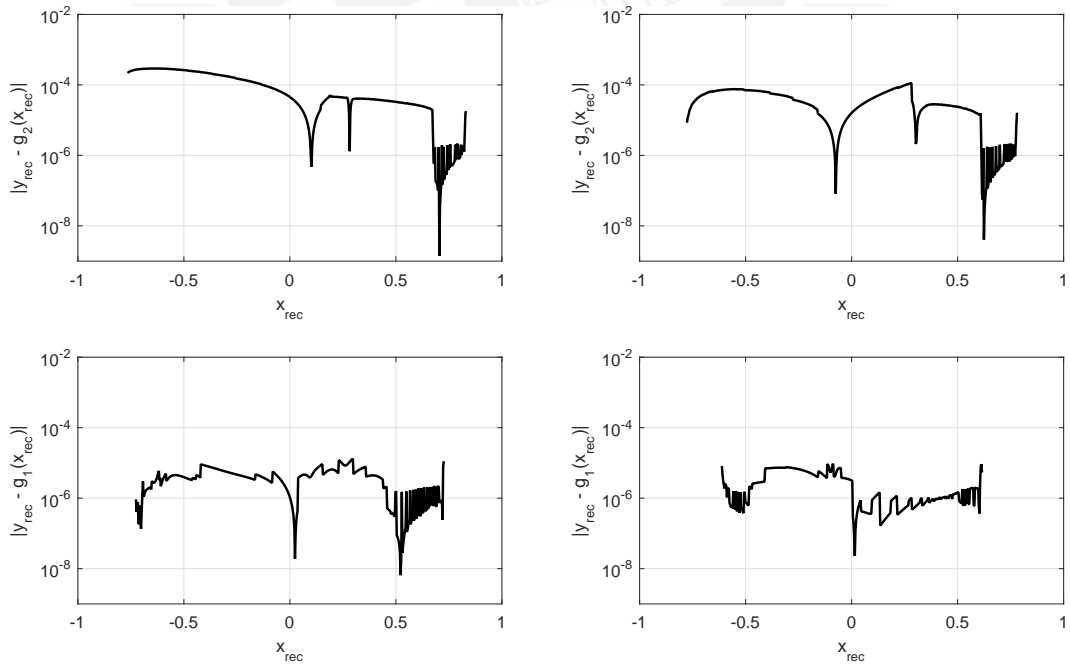


Figure 6.7: Error terms for g_2 and $q = 5$: Top left: $k = \infty$, top right: $k = 20$, bottom left: $k = 10$, bottom right: $k = 5$.

6.3.4 Case 4: Contact considering different pre-curvatures

A: Pre-curvature in the same direction of the flow

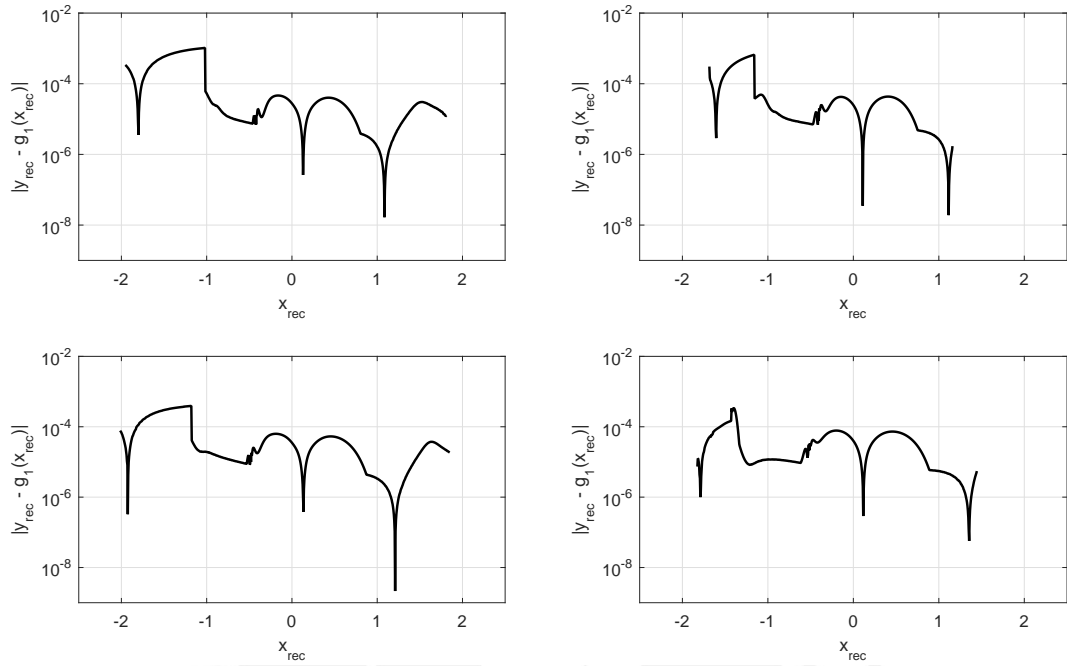


Figure 6.8: Error terms for g_1 and $q = 5$: Top left: $A = 0$ and $B = -0.5$, top right: $A = 0$ and $B = -1$, bottom left: $A = -1$ and $B = 0$, bottom right: $A = -2$ and $B = 0$.

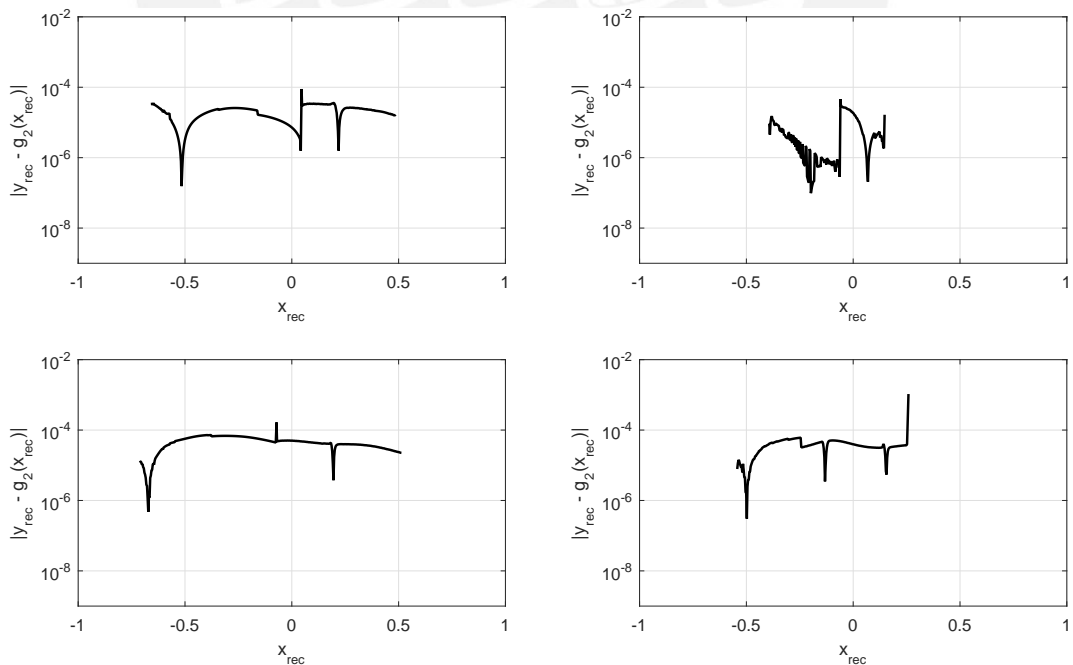


Figure 6.9: Error terms for g_2 and $q = 5$: Top left: $A = 0$ and $B = -0.5$, top right: $A = 0$ and $B = -1$, bottom left: $A = -1$ and $B = 0$, bottom right: $A = -2$ and $B = 0$.

B: Pre-curvature in the opposite direction of the flow

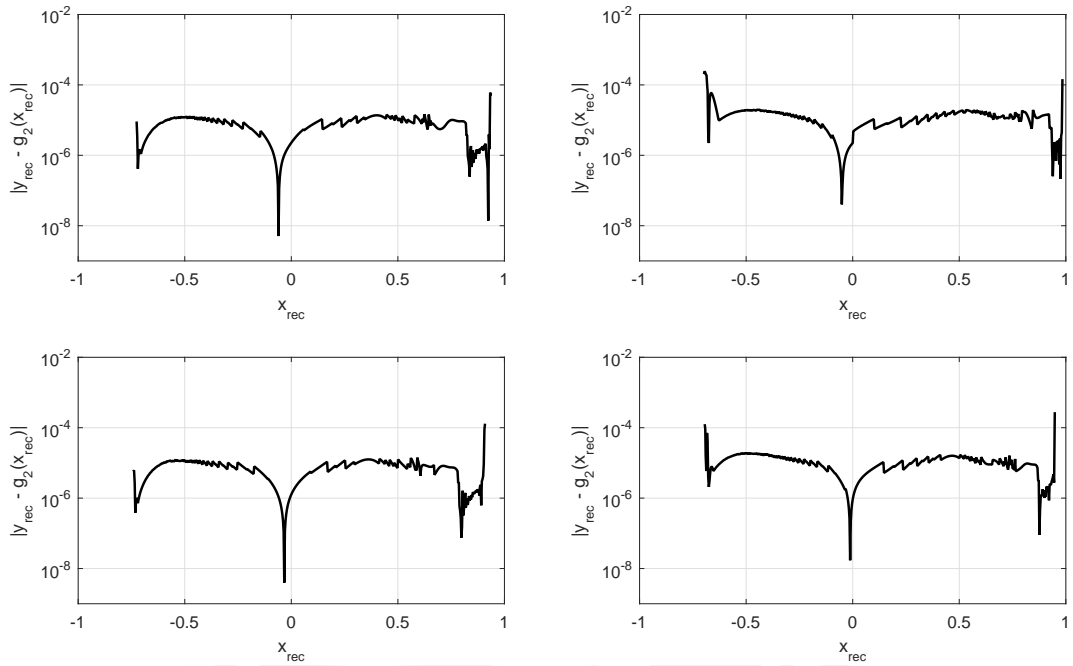


Figure 6.10: Error terms for g_2 : Top left: $A = 0$ and $B = 0.5$, top right: $A = 0$ and $B = 1$, bottom left: $A = 1$ and $B = 0$, bottom right: $A = 2$ and $B = 0$.

6.3.5 Case 5: Contact with all previous considerations

A: Catenary profile

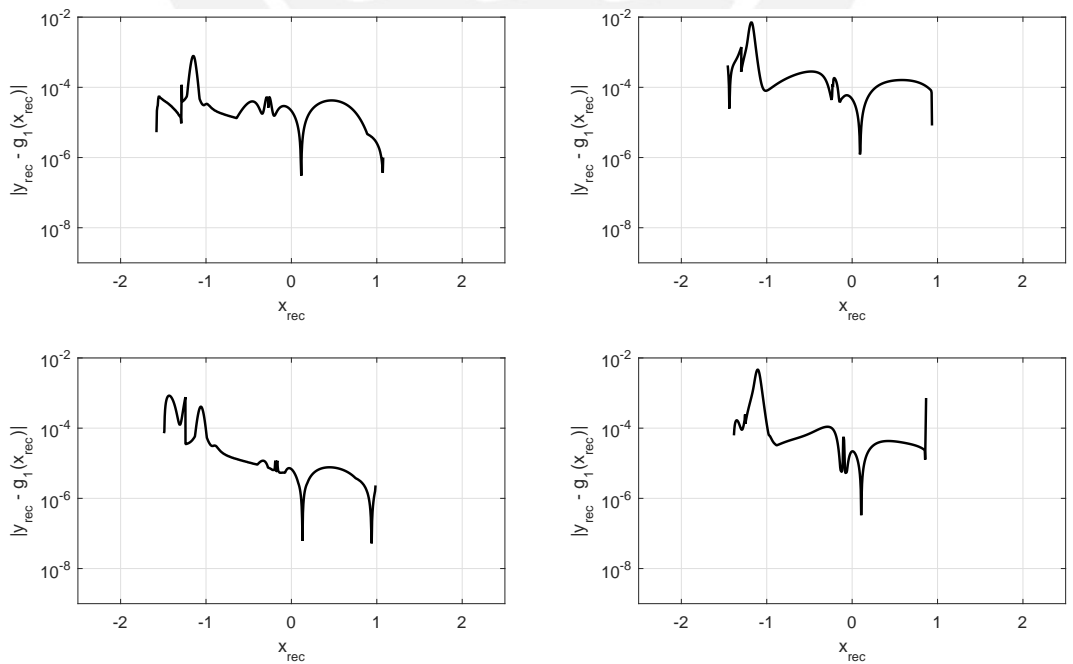


Figure 6.11: Error terms for g_1 and $q = 5$: Top left: $\vartheta = 0.75$ and $k = 20$, top right: $\vartheta = 0.5$ and $k = 20$, bottom left: $\vartheta = 0.75$ and $k = 10$, bottom right: $\vartheta = 0.5$ and $k = 10$.

B: Parabolic profile

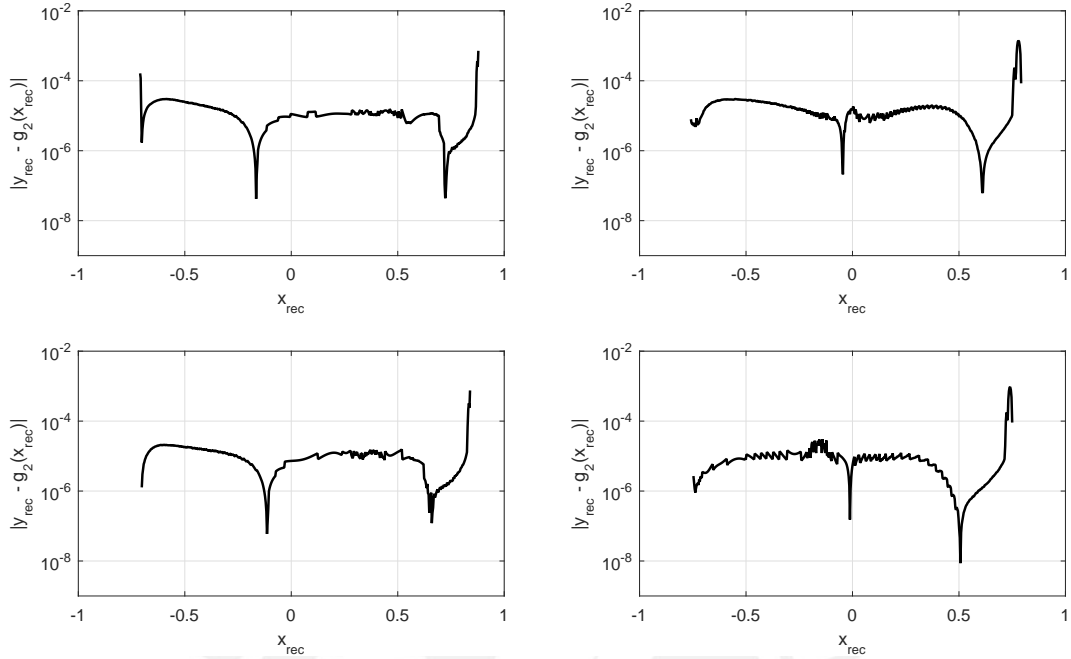


Figure 6.12: Error terms for g_2 , $q = 5$, $A = 2$ and $B = 0$: Top left: $\vartheta = 0.75$ and $k = 20$, top right: $\vartheta = 0.5$ and $k = 20$, bottom left: $\vartheta = 0.75$ and $k = 10$, bottom right: $\vartheta = 0.5$ and $k = 10$.

6.3.6 Experimental case

The profile displayed in (5.11) is also reconstructed, to show that the algorithm works for theoretical and experimental profiles.

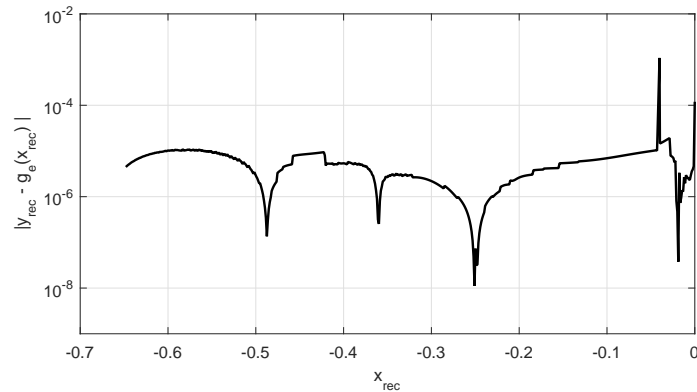


Figure 6.13: Error terms the theoretical sweep of the profile g_e .

6.4 Summary and comments

- An algorithm for the fluid flow load magnitude identification and posterior profile reconstruction is developed. The algorithm successfully identified the magnitude of the applied fluid load.

- The developed algorithm also successfully reconstructed the section of the profile contour that came into contact with the vibrissa. The error between the reconstructed points and the expected points lies overall between 10^{-4} and 10^{-6} .
- A general difficulty encountered in all scenarios is the need to increase the number of iterations and function evaluations. Some points may require an high number of function evaluations (4000 compared to the default 500). It is found that there is a faster convergence of the contact phase A points than those of contact phase B. This is more likely due to the fact that during phase A, s_1 is known, whereas in phase B it is one of the unknowns. The system equation is highly dependent on s_1 and influences almost all terms of the equation.
- A factor that tends to increase the overall error is a low ϑ value. This is likely due to the fact low ϑ come in hand with low bending stiffness at the tip, which may produce convergence issues due to the sensitivity to the starting guess. Low values of ϑ also decrease the segment of the reconstructed profile.
- Certain values of the torsional stiffness at the base show to lower the overall reconstruction error. For instance, scanning the g_2 profile with $k = 5$ proves to yield better results than scanning it with $k = 20$ or $k = \infty$; and for the g_1 profile, a lower value of k tends to yield better results in the latter portion of the scan (see Figs. 6.6 and 6.7). This can be used to implement a system with stiffness depending on the previous measurements.
- A negative pre-curvature or in the “same” direction of the flow does not improve or worsen the reconstructed profile in a significant manner. However, it does decrease the number of measured points, with higher values of negative pre-curvature, reducing more of the reconstructed segment.
- The profile reconstruction results obtained by [Will et al. 2014a], [Will et al. 2014b] and [Will et al. 2015] indicate an error of 10^{-8} , about four orders of magnitude less than those obtained in this work. This is due to the different approaches taken to solve the differential equation of the mechanical model. Whereas an elliptic integral approach is applied in the aforementioned works, this thesis works with a direct numerical approximation of the ODE system using the FDM.

Chapter 7

Conclusions and outlook

In the present thesis, a mechanical-mathematical model of a vibrissa-inspired sensor for object and fluid detection was developed and used for fluid identification and object contour recognition and reconstruction. The vibrissa itself was modeled as a slender, elastic beam capable of large deflections and with certain geometrical and load considerations. The thesis was separated in chapters, which progressively formulated and solved the problem of object and fluid detection and applied the model to certain scenarios to test its capabilities.

In the first chapter, the motivation for the work was stated as well as the problem formulation and a general overview of the master thesis.

During the second chapter the state of the art was explored. The main functions and characteristics of vibrissae were explored and explained, which provided insight into which characteristics should be included in a mechanical-mathematical model, these are pre-curvature, conicity and a elastic support that represents the vibrissa follicle. Current and past developments of prototypes, robots, and devices that rely on vibrissa-inspired sensors were also investigated. Furthermore, an analysis and investigation of mechanical and mathematical models for large deflections of beams (developed by various authors) was performed and a classification as well as an evaluation was done. These models helped to gain insight into the formulations and methods used to approximate the elastica in largely deflected beams. However, no model exhibiting all the characteristics previously described was found in the surveyed literature. Numerical procedures that are used in the solution of these models were also described, with a special emphasis on the non-linear finite difference method, which was widely used in the thesis at hand. For all the models, a user-implemented finite differences algorithm was implemented.

In the third chapter, a mechanical and mathematical model that considers large deflections of beams was developed. This model is based on the non-linear Euler-Bernoulli beam theory. This model considers the characteristics discussed in the previous chapter as mathematical parameters, these are: conicity, pre-curvature and a elastic support. All these features were represented using mathematical parameters in the mathematical model. Two main loads were considered: a concentrated force, representing a contact force, and an uniformly distributed force, representing a fluid flow load. With all parameters and loads forming part of the mechanical model, a mathematical model was developed based on the previously mentioned theory. Then, the model was transformed into a dimensionless representation, since no special interest in a particular vibrissa was contemplated and this allows to obtain more general assertions. Several scenarios were formulated to explore the effects of the variation of loads and parameters, up to 18 scenarios were formulated. The output of this chapter was a dimensionless system of differential equations that takes into consideration all of the characteristics and loading.

In the fourth chapter, the developed model was subjected to all the scenarios formulated

in the previous chapter. Some of the cases were compared to those found in literature and those obtained in the commercial finite element method software ANSYS. The results showed a close similarity between the results obtained through both methods, thus validating the model. The Runge-Kutta method and finite difference method were evaluated and compared, the finite difference method was then chosen due to its robustness for this particular problem. The influence of each parameter was asserted through the study of each of the scenarios. The results used to show the variations are the coordinates of the tip of the beam vs. the dimensionless loads applied and the elastica curve for certain parameters. Most of the scenarios that were analyzed could not be found in the surveyed literature and each one show the variation of one or more parameter.

In the fifth chapter, a simulation of the contact of the vibrissa with the contour of two obstacles was performed. The contour of the obstacle was assumed as a strictly convex profile, meaning that the contact was regarded as happening only at one point at a time and as ideal, thus no frictional force is taken into consideration. Also, a distributed load, acting from the base to the contact point, was considered, which represents the force produced by the fluid flow. The scanning was performed as a quasi-static sweep, meaning that the base of the vibrissa moves at a low speed. For each of the points in the contour profile, the base reactions, position, and the contact force is calculated, “sweeping” the profile. Two main contact phases were studied: a tip contact phase, where the contact point is the tip of the vibrissa and the fluid flow force acts on the whole length of it; and a tangential contact phase, where the contact point is within the arc-length of the vibrissa and is a common tangential point for both curves (the elastica and the contour). Due to the fact that a vibrissa could be pre-curved (naturally) or pre-deformed (by the fluid load), the detection of the first contact point was important. Also, due to the different scenarios analyzed, two different “last contact” scenarios are contemplated, as well as a condition for both. Once again, each parameter was varied and its influence analyzed. For each of the formulated scenarios, the observable quantities such as the reaction forces and moment as well as the deflection angle were “measured” and “recorded”; the contact force as well as the position of the contact point on the arc-length were also obtained for analysis. In order to validate the results, the algorithm used to solve the contact problem was used to make a “sweep” the equation of real profile, and the experimental measures of the observables were compared to their theoretical counterparts. The comparison showed a relatively close relationship between the results.

In the sixth chapter, a reconstruction algorithm was developed – based and adapted from [Will et al. 2014b] – in order to take the observable quantities results from the last chapter and use them to: obtain the magnitude of the fluid load, and reconstruct the obstacle profile. The fluid flow force identification algorithm takes the first point measured (as in this point there is no contact yet) and uses the results to search for a distributed load that produces the same observable quantities. The reconstruction algorithm took the obtained flow load magnitude along with the observable quantities and started a search for the contact point coordinates and the contact force that satisfy and produce the same observable quantities. Each of the resulting contact point coordinates formed a reconstructed profile, which was then compared with the original profile. The difference between the two profiles was calculated and plotted, as a measurement of the reconstruction quality. A close reproduction of the original profiles was obtained, with a relatively small error, for each of the cases as well as the applied fluid flow load, which indicates a successful reconstruction and detection. The theoretical sweeps as well as the experimental sweep of the previous chapter were also reconstructed. The results obtained showed that it is possible to detect and determine the fluid flow load on a vibrissa as well as performing a scan of the contour of an obstacle and reconstruct it. The influence of each vibrissa parameter on the measurements was also analyzed.

Summarizing, all tasks of this Master thesis were successfully solved:

- a non-linear beam model (with different considerations and loads) capable of large deflections was set up and analyzed,
- the influence of each parameter was studied, results show a clear similarity between the obtained results and those obtained in the bibliography and those obtained with the use of FEM software,
- simulations of contact under the influence of flow were performed and the observable magnitudes measured, a comparison with a experimental sweep was also performed, showing clear similarities between the theoretical and experimental results,
- an algorithm for reconstruction of the encountered profile contour was implemented, obtaining a difference with the original profile ranging between 10^{-4} and 10^{-6} on average.

The developed model and obtained results can be used to further studies of the behavior of vibrissa and its capabilities as a tactile sensor for the use as a fluid flow sensor. The developed model showed that scanning a profile contour with the influence of a flow is possible considering an ideal frictionless contact. The model can later be adapted for a frictional contact between an obstacle and a vibrissa sensor.

Numerical simulations and experimentation have already been performed without the influence of a fluid which provide experimental backup in previous works. However, experimental backup is still needed for cases with fluid flow loads. It is shown in the state of the art that the flow behavior changes significantly with the variation of the geometry of the vibrissa, this fact has to be taken carefully into consideration, since it affects the measurements directly inducing vibrations and noise.

Further, varying the value of the stiffness of the elastic support (mimicking the relaxation and tensing of muscles) during the “sweep” may have a positive effect on the measurements, increasing their accuracy. This effect has yet to be studied for the developed model. Furthermore, the developed non-linear model of the beam takes into consideration many geometrical characteristics that have not been found in the surveyed literature. Thus, further studies of non-linear and large deflections of beams can be based on the present thesis, applications in various fields are possible, not only in biomimetics. The finite difference approach, chosen in this thesis for numerical simulations, can also be further explored as an alternative to similar problems or to cases where other method may become unstable or do not yield physically significant results. This exploration may include adaptive step sizes, a study to minimize the error terms of the approximation, and reducing the computational time needed to obtain a solution.

Bibliography

- Ahissar, E. and P. M. Knutsen (2011). “Vibrissal location coding”. *Scholarpedia* 6(10), p. 6639. DOI: 10.4249/scholarpedia.6639. Revision 151626.
- Ahl, A.S. (1986). “The role of vibrissae in behavior: A status review”. *Veterinary Research Communications* 10, pp. 245–268. DOI: 10.1007/BF02213989.
- Ahl, A.S. (1987). “Relationship of Vibrissal Length and Habits in the Sciuridae”. *Journal of Mammalogy* 68(4), pp. 848–853. DOI: 10.2307/1381563.
- Ang, M. H., W. Wei, and L. Teck-Seng (1993). “On the estimation of the large deflection of a cantilever beam”. In: *Proceedings of IECON'93 - 19th Annual Conference of IEEE Industrial Electronics*, pp. 1604–1609. DOI: 10.1109/IECON.1993.339311.
- Arabzadeh, E., M. von Heimendahl, and M. E. Diamond (2009). “Vibrissal texture decoding”. *Scholarpedia* 4(4), p. 6640. DOI: 10.4249/scholarpedia.6640. Revision 149576.
- Ascher, U. M., R. M. Mattheij, and R. D. Russell (1995). *Numerical Solution of Boundary Value Problems for Ordinary Differential Equations*. 1st. Society for Industrial and Applied Mathematics. ISBN: 978-0-89871-354-1. DOI: 10.1137/1.9781611971231.
- Bar-Cohen, Y. (2006). *Biomimetics: biologically inspired technologies*. 1st. CRC Press Taylor & Francis Group, p. 527. DOI: 10.1016/S1369-7021(06)71400-6.
- Bebek, O. and M. C. Cavusoglu (2007). “Whisker Sensor Design for Three Dimensional Position Measurement in Robotic Assisted Beating Heart Surgery”. In: *Proceedings 2007 IEEE International Conference on Robotics and Automation*. IEEE, pp. 225–231. DOI: 10.1109/ROBOT.2007.363791.
- Beem, H., M. Hildner, and M. Triantafyllou (2012). “Characterization of a harbor seal whisker-inspired flow sensor”. In: *OCEANS 2012 MTS/IEEE: Harnessing the Power of the Ocean*, pp. 2–5. DOI: 10.1109/OCEANS.2012.6404978.
- Beer, F.P., E.R Johnston, and J. DeWolf (2012). *Mechanics of Materials*. McGraw-Hill. ISBN: 978-0-07-131439-8.
- Beem, H., M. Hildner, and M. Triantafyllou (2013). “Calibration and validation of a harbor seal whisker-inspired flow sensor”. *Smart Materials and Structures* 22(1), p. 014012. DOI: 10.1088/0964-1726/22/1/014012.
- Behn, C., J. Steigenberger, and K. Zimmermann (2009). “Finite Degree-of-Freedom Models for Animal Vibrissae”. In: *Proceedings of the European Control Conference 2009*, pp. 2500–2505. ISBN: 978-3-9524173-9-3.
- Behn, C., T. Schmitz, H. Witte, and K. Zimmermann (2013). “Animal vibrissae: Modeling and adaptive control of bio-inspired sensors”. In: *Proceedings of the 12th international conference on Artificial Neural Networks: advances in computational intelligence*. Vol. Part 2, pp. 159–170. DOI: 10.1007/978-3-642-38682-4_19.

- Behn, C., J. Steigenberger, A. Sauter, and C. Will (2016). "Pre-curved Beams as Technical Tactile Sensors for Object Shape Recognition". In: *INTELLI 2016 : The Fifth International Conference on Intelligent Systems and Applications (includes InManEnt 2016)*, pp. 7–12. ISBN: 978-1-61208-518-0.
- Beléndez, T., C. Neipp, and A. Beléndez (2002). "Large and small deflections of a cantilever beam". *European Journal of Physics* 23(3), pp. 371–379. DOI: 10.1088/0143-0807/23/3/317.
- Berkelman, P. J., L. L. Whitcomb, R. H. Taylor, and P. Jensen (2003). "A Miniature Microsurgical Instrument Tip Force Sensor for Enhanced Force Feedback During Robot-Assisted Manipulation". *IEEE Transactions on Robotics and Automation* 19(5), pp. 917–922. DOI: 10.1109/TRA.2003.817526.
- Birdwell, J. A., J. H. Solomon, M. Thajchayapong, A. Taylor, M. Cheely, R. B. Towal, J. Conradt, and M. J. Z. Hartmann (2007). "Biomechanical Models for Radial Distance Determination by the Rat Vibrissal System". *Journal of Neurophysiology*, pp. 2439–2455. DOI: 10.1152/jn.00707.2006.
- Bisshopp, K. E. and D. C. Drucker (1945). "Large Deflection of Cantilever Beams". *Quarterly of Applied Math* 3(3), pp. 272–275.
- Burden, R. L. and J. D. Faires (2011). *Numerical Analysis*. 9th. Boston: Cengage Learning. ISBN: 9780538733519.
- Chapra, S. and R.P. Canale (2010). *Numerical Methods for Engineering*. 7th. McGraw-Hill. ISBN: 9780071267595.
- Cheney, W. and D. Kincaid (2008). *Numerical Mathematics and Computing*. 6th. Thomson Brooks/Cole, p. 840. ISBN: 978-0-495-11475-8.
- Chen, L. (2010). "An integral approach for large deflection cantilever beams". *International Journal of Non-Linear Mechanics* 45(3), pp. 301–305. DOI: 10.1016/j.ijnonlinmec.2009.12.004.
- Davis, H., K. A. MacKenzie, and S. Morrison (1989). "Numerical discrimination by rats (*Rattus norvegicus*) using body and vibrissal touch." *Journal of Comparative Psychology* 103, pp. 45–53. DOI: 10.1037/0735-7036.103.1.45.
- Dehnhardt, G., W. Hanke, and H. Bleckmann (2001). "Hydrodynamic Trail-Following in Harbor Seals (*Phoca vitulina*)". *Science* 293, pp. 102–104.
- Fertis, D. (2007). *Nonlinear Structural Engineering*. 1st. Heidelberg, Germany: Springer-Verlag. ISBN: 9783540329756.
- Gere, J. and B. Goodno (2008). *Mechanics of materials*. 7th. Toronto, Canada: Cengage Learning. ISBN: 9780534553975.
- Giguere, P. and G. Dudek (2011). "A simple tactile probe for surface identification by mobile robots". *IEEE Transactions on Robotics* 27(3), pp. 534–544. DOI: 10.1109/TR0.2011.2119910.
- Hanke, W., M. Witte, L. Miersch, M. Brede, J. Oeffner, M. Michael, F. Hanke, A. Leder, and G. Dehnhardt (2010). "Harbor seal vibrissa morphology suppresses vortex-induced vibrations." *Journal of Experimental Biology* 213(15), pp. 2665–2672. DOI: 10.1242/jeb.043216.
- Hans, H., J. M. Miao, and M. Triantafyllou (2014). "Mechanical characteristics of harbor seal (*Phoca vitulina*) vibrissae under different circumstances and their implications on

- its sensing methodology”. *Bioinspiration & biomimetics* 9(3), p. 036013. DOI: 10.1088/1748-3182/9/3/036013.
- Hanke, W. and G. Dehnhardt (2015). “Vibrissal touch in pinnipeds”. *Scholarpedia* 10(3), p. 6828. DOI: 10.4249/scholarpedia.6828. Revision 149468.
- Hartmann, M. J. Z. (2015). “Vibrissal mechanical properties”. *Scholarpedia* 10(5), p. 6636. DOI: 10.4249/scholarpedia.6640.
- Hibbeler, R.C. (2011). *Mechanics of Materials*. 8th. Pearson. ISBN: 9780136022305.
- Hyvärinen, H., H. Kangasperko, and R. Peura (1977). “Functional structure of the carpal and ventral vibrissae of the squirrel (*Sciurus vulgaris*)”. *Journal of Zoology* 182(4), pp. 457–466. DOI: 10.1111/j.1469-7998.1977.tb04162.x.
- Iott, J., R. T. Haftka, and H. M. Adelman (1985). *Selecting Step Sizes in Sensitivity Analysis by Finite Differences*. NASA Technical Memorandum.
- Kemper, J. D. (1968). “Large deflections of tapered cantilever beams”. *International Journal of Mechanical Sciences* 10(6), pp. 469–478. DOI: 10.1016/0020-7403(68)90027-1.
- Kim, D. E. and R. Möller (2005). “Biomimetic Whisker Experiments for Tactile Perception”. In: *Proceedings of International Symposium on Adaptive Motion*, pp. 1–7. ISBN: 3-932633-99-7.
- Kim, D. E. and R. Möller (2006). “Passive sensing and active sensing of a biomimetic whisker”. In: *Proceedings of International Conference on the Simulation and Synthesis of Living Systems*, pp. 282–288.
- Kim, D. E. and R. Möller (2007). “Biomimetic whiskers for shape recognition”. *Robotics and Autonomous Systems* 55(3), pp. 229–243. DOI: 10.1016/j.robot.2006.08.001.
- Kimiaefar, A., N. Tolou, A. Barari, and J.L. Herder (2014). “Large deflection analysis of cantilever beam under end point and distributed loads”. *Journal of the Chinese Institute of Engineers* 37(4), pp. 438–445. DOI: 10.1080/02533839.2013.814991.
- Knutsen, P. M., A. Biess, and E. Ahissar (2008). “Vibrissal Kinematics in 3D: Tight Coupling of Azimuth, Elevation, and Torsion across Different Whisking Modes”. *Neuron* 59(1), pp. 35–42. DOI: 10.1016/j.neuron.2008.05.013.
- Koo Lee, B., J. F. Wilson, and S. Jin Oh (1993). “Elastica of cantilevered beams with variable cross sections”. *International Journal of Non-Linear Mechanics* 28(5), pp. 579–589. DOI: 10.1016/0020-7462(93)90049-Q.
- Lawrence, J. D. (1972). *A Catalog of Special Plane Curves*. 1st. New York: Dover Publications. ISBN: 0486602885.
- Lee, K. (2002). “Large deflections of cantilever beams of non-linear elastic material under a combined loading”. *International Journal of Non-Linear Mechanics* 37(3), pp. 439–443. DOI: 10.1016/S0020-7462(01)00019-1.
- Li, D. (2008). “Bionics”. In: *Encyclopedia of Microfluids and Nanofluids*. Boston, MA: Springer US. Chap. Bionics, pp. 67–84. ISBN: 978-0-387-48998-8.
- Lyne, A. G. (1952). “Notes on external characters of the pouch young of four species of bandicoot”. In: *Proceedings of the Zoological Society of London*. Vol. 122. 3, pp. 625–649. DOI: 10.1111/j.1096-3642.1952.tb00247.x.
- Marshall, C. D., H. Amin, K. M. Kovacs, and C. Lydersen (2006). “Microstructure and innervation of the mystacial vibrissal follicle-sinus complex in bearded seals, *Erignathus*

BIBLIOGRAPHY

- barbatus (Pinnipedia: Phocidae)". *The Anatomical Record Part A: Discoveries in Molecular, Cellular, and Evolutionary Biology* 288A(1), pp. 13–25. DOI: 10.1002/ar.a.20273.
- Mathews, J. H. and K. D. Fink (1999). *Numerical Methods Using MATLAB*. 3rd. Saddle River: Prentice Hall, p. 662. ISBN: 0-13-624990-6.
- Miersch, L., W. Hanke, S. Wieskotten, F. Hanke, J. Oeffner, A. Leder, M. Brede, M. Witte, and G. Dehnhardt (2011). "Flow sensing by pinniped whiskers". *Philosophical Transactions of the Royal Society B: Biological Sciences* 366(1581), pp. 3077–3084. DOI: 10.1098/rstb.2011.0155.
- Morsch, F. M., N. Tolou, and J. L. Herder (2009). "Comparison of methods for large deflection analysis of a cantilever beam under free end point load cases". In: *Proceedings of the ASME Design Engineering Technical Conferences and Computers and Information in Engineering Conference*. Vol. 7. January 2009, pp. 183–191. DOI: 10.1115/DETC2009-86754.
- Morrison, H. E., M. Brede, G. Dehnhardt, and A. Leder (2016). "Simulating the flow and trail following capabilities of harbour seal vibrissae with the Lattice Boltzmann Method". *Journal of Computational Science*. DOI: 10.1016/j.jocs.2016.04.004.
- Mutyalarao, M., D. Bharathi, and B. N. Rao (2010). "Large deflections of a cantilever beam under an inclined end load". *Applied Mathematics and Computation* 217(7), pp. 3607–3613. DOI: 10.1016/j.amc.2010.09.021.
- Nallathambi, A. K., C. Lakshmana Rao, and S. M. Srinivasan (2010). "Large deflection of constant curvature cantilever beam under follower load". *International Journal of Mechanical Sciences* 52(3), pp. 440–445. DOI: 10.1016/j.ijmecsci.2009.11.004.
- Nicholls, H. R. and M. H. Lee (1989). "A Survey of Robot Tactile Sensing Technology". *The International Journal of Robotics Research* 8(3), pp. 3–30. DOI: 10.1177/027836498900800301.
- O'Neil, P. V. (2011). *Advanced Engineering Mathematics*. 7th. Cengage Learning. ISBN: 9781111427412.
- Pal, M. (2007). *Numerical Analysis for Scientists and Engineers: Theory and C Programs*. Alpha Science International. ISBN: 9781842653647.
- Pearson, M. J., A. G. Pipe, C. Melhuish, B. Mitchinson, and T. J. Prescott (2007). "Whiskerbot: A robotic active touch system modeled on the rat whisker sensory system". *Adaptive Behavior* 15(3), pp. 223–240. DOI: 10.1177/1059712307082089.
- Pearson, O. P. (1962). "Survival Value of Vibrissae". *Journal of Mammalogy* 43(1), p. 105. DOI: 10.2307/1376889.
- Pocock, R. I. (1914). "On the Facial Vibrissae of Mammalia." In: *Proceedings of the Zoological Society of London*. Vol. 84. 3, pp. 889–912. DOI: 10.1111/j.1469-7998.1914.tb07067.x.
- Pocock, R. I. (1926). "The External Characters of Thylacinus, Sarcophilus and some related Marsupials." *Proceedings of the Zoological Society of London* (4), pp. 1037–1084. DOI: 10.1111/j.1096-3642.1926.tb02233.x.
- Prescott, T. J., M. J. Pearson, B. Mitchinson, J. C. Sullivan, and A. G. Pipe (2009). "Whisking with robots: From rat vibrissae to biomimetic technology for active touch". *IEEE Robotics and Automation Magazine* 16(3), pp. 42–50. DOI: 10.1109/MRA.2009.933624.

- Prescott, T. J., B. Mitchinson, and R. A. Grant (2011). “Vibrissal behavior and function”. *Scholarpedia* 6(10), p. 6642. DOI: 10.2991/978-94-6239-133-8_7. Revision 153103.
- Quist, B. W. and M. J. Z. Hartmann (2012). “Mechanical signals at the base of a rat vibrissa: The effect of intrinsic vibrissa curvature and implications for tactile exploration.” *Journal of Neurophysiology* 107(9), pp. 2298–2312. DOI: 10.1152/jn.00372.2011.
- Rao, B. N. and G. Rao (1989). “Large deflections of a cantilever beam subjected to a rotational distributed loading”. *Forschung im Ingenieurwesen* 55(4), pp. 116–120.
- Reep, R. and D.K. Sarko (2009). “Tactile hair in Manatees”. *Scholarpedia* 4(4), p. 6831. DOI: 10.4249/scholarpedia.6831. Revision 143233.
- Roth-Alpermann, C. and M. Brecht (2009). “Vibrissal touch in the Etruscan shrew”. *Scholarpedia* 4(11), p. 6830. DOI: 10.4249/scholarpedia.6830. Revision 91921.
- Scharff, M., C. Behn, J. Steigenberger, and J. Alencastre (2016). “Towards the Development of Tactile Sensors for Surface Texture Detection”. In: *International Conference on Intelligent Systems and Applications at Barcelona, Spain*. ISBN: 978-1-61208-518-0.
- Schwarz, D. (2005). *Fast and Robust Curve Intersections, MATLAB Central File Exchange*. URL: <http://de.mathworks.com/matlabcentral/fileexchange/11837-fast-and-robust-curve-intersections> (visited on 11/14/2016).
- Shvartsman, B. S. (2007). “Large deflections of a cantilever beam subjected to a follower force”. *Journal of Sound and Vibration* 304(3-5), pp. 969–973. DOI: 10.1016/j.jsv.2007.03.010.
- Shvartsman, B. S. (2013). “Analysis of large deflections of a curved cantilever subjected to a tip-concentrated follower force”. *International Journal of Non-Linear Mechanics* 50, pp. 75–80. DOI: 10.1016/j.ijnonlinmec.2012.10.015.
- Solomon, J. H. and M. J. Z. Hartmann (2006). “Biomechanics: robotic whiskers used to sense features.” *Nature* 443(7111), p. 525. DOI: 10.1038/443525a.
- Solomon, J. H. and M. J. Z. Hartmann (2008). “Artificial whiskers suitable for array implementation: Accounting for lateral slip and surface friction”. *IEEE Transactions on Robotics* 24(5), pp. 1157–1167. DOI: 10.1109/TR0.2008.2002562.
- Spotorno, A., C. A. Zuleta, J. P. Valladares, A. L. Deane, and J. E. Jime (2004). “Chinchilla laniger”. *Mammalian Species* 758(758), pp. 1–9. DOI: 10.1644/758.
- Steigenberger, J., C. Behn, and C. Will (2015). “Mathematical model of vibrissae for surface texture detection”. Preprint No. 15/03 - Technische Universität Ilmenau.
- Steigenberger, J. (2013). “A Continuum Model of Passive Vibrissae”. Preprint No. 13/03 - Technische Universität Ilmenau.
- Sullivan, J. C., B. Mitchinson, M. J. Pearson, M. Evans, N. F. Lepora, C. W. Fox, C. Melhuish, and T. J. Prescott (2012). “Tactile discrimination using active whisker sensors”. *IEEE Sensors Journal* 12(2), pp. 350–362. DOI: 10.1109/JSEN.2011.2148114.
- Towal, R. B., B. W. Quist, V. Gopal, J. H. Solomon, and M. J. Z. Hartmann (2011). “The morphology of the rat vibrissal array: A model for quantifying spatiotemporal patterns of whisker-object contact”. *PLoS Computational Biology* 7(4), pp. 1–17. DOI: 10.1371/journal.pcbi.1001120.
- Tuna, C., J. H. Solomon, D. L. Jones, and M. J. Z. Hartmann (2012). “Object shape recognition with artificial whiskers using tomographic reconstruction”. In: *2012 IEEE Inter-*

BIBLIOGRAPHY

- national Conference on Acoustics, Speech and Signal Processing (ICASSP)*, pp. 2537–2540. DOI: 10.1109/ICASSP.2012.6288433.
- Valdivia y Alvarado, P., V. Subramaniam, and M. Triantafyllou (2012). “Design of a bio-inspired whisker sensor for underwater applications”. In: *Proceedings of IEEE Sensors*, pp. 1–4. DOI: 10.1109/ICSENS.2012.6411517.
- Van Horn, R. N. (1970). “Vibrissae Structure in the Rhesus Monkey”. *Folia Primatologica* 13(4), pp. 241–285. DOI: 10.1159/000155325.
- Vincent, J. F. V., O. A. Bogatyreva, N. R. Bogatyrev, A. Bowyer, and A. Pahl (2006). “Biomimetics : its practice and theory”. *Journal of the Royal Society* (April), pp. 471–482. DOI: 10.1098/rsif.2006.0127.
- Voges, D., K. Carl, G. J. Klauer, R. Uhlig, C. Schilling, C. Behn, and H. Witte (2012). “Structural characterization of the whisker system of the rat”. *IEEE Sensors Journal* 12(2), pp. 332–339. DOI: 10.1109/JSEN.2011.2161464.
- Weisstein, E. W. (2016). *Cesáro Equation*. URL: <http://mathworld.wolfram.com/CesaroEquation.html> (visited on 11/29/2016).
- Williams, C. M. and E. M. Kramer (2010). “The Advantages of a Tapered Whisker”. *PLoS ONE* 5(1), e8806. DOI: 10.1371/journal.pone.0008806. URL: <http://dx.plos.org/10.1371/journal.pone.0008806>.
- Will, C., J. Steigenberger, and C. Behn (2014a). “Object contour reconstruction using bio-inspired sensors”. In: *11th International Conference on Informatics in Control, Automation and Robotics, ICINCO 2014*, pp. 459–467. DOI: 10.5220/0005018004590467.
- Will, C., J. Steigenberger, and C. Behn (2014b). “Quasi-static object scanning using technical vibrissae”. In: *58th Ilmenau Scientific Colloquium*. September, pp. 8–12.
- Will, C., J. Steigenberger, and C. Behn (2015). “Obstacle scanning by technical vibrissae with compliant support”. Preprint No. M 15/07 - Technische Universität Ilmenau.
- Will, C., C. Behn, and J. Steigenberger (2016). “Object contour scanning using elastically supported technical vibrissae”. *Zeitschrift für Angewandte Mathematik und Mechanik*.
- Yates, R. (1952). *Curves and their properti*. 1st ed. National Council of Teachers of Mathematics, p. 245.
- Yokoi, H., M. Lungarella, M. Fend, and R. Pfeifer (2005). “Artificial Whiskers: Structural Characterization and Implications for Adaptive Robots”. *Journal of Robotics and Mechatronics* 17(5), pp. 584–595. DOI: 10.20965/jrm.2005.p0584.
- Zill, D. G. and M. R. Cullen (2008). *Matemáticas Avanzadas para Ingeniería: Ecuaciones Diferenciales*. 3rd. Vol. 1. Mexico DF.: McGraw-Hill. ISBN: 9788578110796. DOI: 10.1088/1751-8113/44/8/085201.